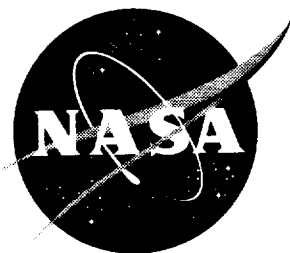


NASA/CR-2000-210301



Advanced Atmospheric Water Vapor DIAL Detection System

*Tamer F. Refaat and Hani E. Elsayed-Ali
Old Dominion University, Norfolk, Virginia*

National Aeronautics and
Space Administration

Langley Research Center
Hampton, Virginia 23681-2199

Prepared for Langley Research Center
under Purchase Order L-68314D

June 2000

Available from:

NASA Center for AeroSpace Information (CASI)
7121 Standard Drive
Hanover, MD 21076-1320
(301) 621-0390

National Technical Information Service (NTIS)
5285 Port Royal Road
Springfield, VA 22161-2171
(703) 605-6000

ABSTRACT

ADVANCED ATMOSPHERIC WATER VAPOR DIAL DETECTION SYSTEM

Measurement of atmospheric water vapor is very important for understanding the Earth's climate and water cycle. The remote sensing Differential Absorption Lidar (DIAL) technique is a powerful method to perform such measurement from aircraft and space. This thesis describes a new advanced detection system, which incorporates major improvements regarding sensitivity and size. These improvements include a low noise advanced avalanche photodiode detector, a custom analog circuit, a 14-bit digitizer, a microcontroller for on board averaging and finally a fast computer interface.

This thesis describes the design and validation of this new water vapor DIAL detection system which was integrated onto a small Printed Circuit Board (PCB) with minimal weight and power consumption. Comparing its measurements to an existing DIAL system for aerosol and water vapor profiling validated the detection system.

TABLE OF CONTENTS

	Page
LIST OF TABLES.....	vi
LIST OF FIGURES.....	vii
I. INTRODUCTION.....	1
1.1. Atmospheric water vapor.....	1
1.2. Water vapor measurement using lidar	2
1.3. Research objectives	5
II. AVALANCHE PHOTODIODE; THEORY AND MODEL	8
2.1. Avalanche photodiode structure and theory of operation.....	8
2.2. Modeling of four layer avalanche photodiode.....	11
2.2.1. Rate equations	13
2.2.2. Continuity equation.....	16
2.2.3. Avalanche photodiode equivalent circuit	18
2.3. Model validation.....	23
2.3.1. Model parameters	23
2.3.2. Steady state performance	24
2.3.3. Transient performance.....	31
2.3.4. Model conclusion and limitation	34
III. AVALANCHE PHOTODIODE; CHARACTERIZATION AND SELECTION.	36
3.1. Experimental setup	36
3.2. Avalanche photodiode calibration	40
3.3. Temperature dependent responsivity	41
3.4. Bias voltage dependent responsivity.....	45
3.5. Responsivity uniformity scan	49
3.6. Noise measurement	52
3.7. Frequency response	54
3.8. Avalanche photodiode selection results.....	56
IV. DETECTION SYSTEM DESIGN AND LABORATORY PERFORMANCE ...	58
4.1. Detection system design	58
4.1.1. Analog circuit	61
4.1.2. Digital Circuit	66
4.2. Detection system settings	71
4.2.1. Microcontroller program	72
4.2.2. Data acquisition card	74
4.3. Laboratory performance setting	76

	Page
4.3.1. Temperature and bias voltage controllers performance	77
4.3.2. Signal conditioning performance	79
4.3.3. Digitizer performance.....	81
4.3.4. Overall system performance	83
V. THE LIDAR THEORY	87
5.1. The lidar equation	87
5.1.1. Receiver optics geometry	92
5.1.2. Geometrical form factor for simple overlap	94
5.2. The DIAL equation	97
5.3. Applied lidar measurement technique	100
5.3.1. Aerosol measurement	101
5.3.2. Water vapor measurement	102
VI. VALIDATION OF THE DETECTION SYSTEM	103
6.1. Receiver system setup	103
6.2. Detection system validation with NASA airborne DIAL system	106
6.3. Water vapor DIAL detection system validation.....	109
VII. CONCLUSIONS	113
REFERENCES	116
APPENDICES.....	125
A. APD MANUFACTURER DATA AND CHARACTERIZATION RESULTS	125
A.1. APD designator and manufacturer data	125
A.2. SLIK APD package	126
A.3. APD calibration results	127
A.4. APD Surface scan results	128
A.5. APD responsivity variation with temperature	129
A.6. APD responsivity variation with bias voltage	130
A.7. APD noise measurement	131
B. DETECTION SYSTEM APPLIED CIRCUITS	132
B.1. Analog to digital converter circuit	132
B.2. Data collect and store circuit	132
B.3. Microcontroller connection circuit	133
B.4. Output stage	135
B.5. Chip power supply bypassing	136
B.6. Clock and trigger isolation	136

	Page
C. ELEMENTS OF THE NEW DETECTION SYSTEM	137
C.1. Detection system components	137
C.2. Detection system power consumption	139

LIST OF TABLES

Table	Page
2.1 Silicon APD parameters at 300 K.	23
3.1 APD noise measurements results.	53
4.1 Timing intervals for different record length.	76
6.1 Dullas Airport water vapor profile data on November 5, 1999 at 7:00 am.	11
6.2 Wallops Island water vapor profile data on November 5, 1999 at 7:00 am.	111
7.1 DIAL detection system performance summary.	115

LIST OF FIGURES

Figure	Page
1.1 LASE system block diagram.....	3
1.2 Schematic of the new DIAL receiver system.....	6
2.1 PIN diode and different APD structures with electric field distribution.....	10
2.2 Schematic diagram of a four-layer APD with electric field profiles.....	12
2.3 APD equivalent circuit	22
2.4 APD spectral response obtained from manufacturer data sheet and model.....	25
2.5 APD quantum efficiency versus wavelength.....	26
2.6 APD responsivity variation with bias voltage at 830 nm.....	27
2.7 Responsivity and stability constant variation with multiplication width.....	29
2.8 Donor and acceptor concentration effect on the APD responsivity.....	29
2.9 Spectral response variation with the width of the absorption region	31
2.10 APD output current with a square wave input power of 100 ps duration.....	32
2.11 APD output current during breakdown.....	33
2.12 APD breakdown time variation.....	33
3.1 APD experimental setup for the spectral response determination	37
3.2 APD bias circuit and mounting chamber	38
3.3 APD alignment setup using microscope.....	39
3.4 Spectral response of the reference detector and test detectors.....	41
3.5 APD spectral response and responsivity variation with temperature	43
3.6 APD relative error in responsivity due to 1 °C temperature variation.....	45
3.7 APD spectral response and responsivity variation with bias voltage	48

3.8 APD relative error in responsivity due to 1 V deviation in the bias voltage.....	49
3.9 Responsivity uniformity scan setup.....	50
3.10 Laser focal point evaluation setup using a pinhole.....	51
3.11 APD surface scan.....	51
3.12 APD noise-equivalent-power and figure-of-merit measurements	53
3.13 Frequency response experimental setup	55
3.14 SLIK APD frequency response.....	57
4.1 Block diagram of the analog circuit	59
4.2 Block diagram of the digital circuit.....	60
4.3 Circuit diagram of the signal conditioning stage.....	62
4.4 APD voltage bias controller circuit diagram.....	64
4.5 APD temperature controller circuit diagram	65
4.6 Block diagram of the data collect and store circuit.....	67
4.7 System memory map	68
4.8 Microcontroller connection block diagram.....	70
4.9 Block diagram of the output stage.....	71
4.10 Flowchart of the microcontroller program	73
4.11 Microcontroller ports 1 and 2 configuration.....	73
4.12 Dip switch configuration	74
4.13 Flowchart of the PCI-DIO-32HS data acquisition card	75
4.14 PCI-DIO-32HS data acquisition card connection to the detection system	75
4.15 Detection system data flow diagram	76

4.16	Experimental setup for detection system laboratory performance testing	77
4.17	APD temperature controller response	78
4.18	APD voltage bias monitor and bias voltage transients	79
4.19	Signal conditioning stage normalized gain versus input voltage	80
4.20	Signal conditioning stage frequency response	81
4.21	APD and signal conditioning stage low frequency noise spectrum.....	82
4.22	Histogram plot indicates no missing codes.....	83
4.23	System output versus input light intensity and signal-to-noise ratio	84
4.24	Simulated lidar return signals.....	86
5.1	Geometry of the target plane at range R	93
5.2	The three possible cases for telescope field of view and laser overlap.....	96
5.3	Geometry of the biaxial lidar	96
5.4	DIAL on- and off-line wavelengths relative to water vapor absorption line	98
5.5	Ideal lidar return signal as obtained from the digitizer output	100
6.1	Water vapor DIAL detection system as a part of the receiver.....	104
6.2	Focusing optics alignment setup with the detection system	105
6.3	Detection system output corresponding to the best alignment	106
6.4	Detection system validation setup with NASA airborne DIAL system.....	106
6.5	New detection system return signals.....	108
6.6	Aerosol profiles	108
6.7	On- and off-line return signals	110
6.8	Water vapor profiles.....	110
6.9	Measured and calculated return signals.....	112

CHAPTER I

INTRODUCTION

1.1. Atmospheric water vapor

Water vapor is an important molecular species which is primarily located in the Earth's troposphere (part of the atmosphere extending from the surface of the Earth up to an altitude of about 18 km). Although the distribution of atmospheric water vapor is highly variable in both time and location, its measurement is very important for understanding the Earth's water cycle, the greenhouse effect and weather phenomena.^{1,2}

The water cycle provides a direct way for interactions among Earth's global systems, namely, the atmosphere, hydrosphere, cryosphere, lithosphere and biosphere. Water is considered the main media for energy transfer between most of these systems. Although the amount of atmospheric water vapor represents only a small percent of the Earth's water reservoir, it is very dynamic and its latent heat for transformation is considered the main energy source that maintains the atmospheric circulation.^{1,2}

Water vapor and clouds affect the incident solar radiation by reflecting solar radiation back to space and also absorbing some of this energy within the atmosphere. This substantially moderates the Earth's climate. On the other hand, water vapor and clouds affect infrared radiation released by the Earth's surface. Some of this radiation is reflected back to the surface and some is absorbed and re-emitted at a lower temperature which contributes to the global warming problem or greenhouse effect.²

Journal model used for this thesis is *Optical Engineering*.

Water vapor has a direct role in most weather phenomena and natural disasters such as hurricanes. It was found that the latent heat of water vapor is the main energy source for hurricanes. The measurement of water vapor flow into a hurricane associated with other observations aids in estimating the hurricane strength and direction.^{3,4}

Water vapor measurements can be obtained by balloon radio-sondes but a more effective method is the laser remote sensing technique onboard an aircraft or satellite. Such systems have the advantage of obtaining two-dimensional water vapor profiles with high accuracy.^{5,6}

1.2. Water vapor measurements using lidar

Light detection and ranging (lidar) is a remote sensing technique which is currently used for atmospheric water vapor measurements.^{5,6} At NASA Langley Research Center, the lidar atmospheric sensing experiment (LASE) uses the differential absorption lidar (DIAL) technique to measure water vapor profiles using the ER-2, DC-8 or P3-B aircraft.⁶⁻¹³ LASE consists of three main systems, the DIAL laser transmitter, the receiver and the control and data acquisition system.⁷

In a typical water vapor DIAL system two laser pulses separated by a time interval are transmitted into the atmosphere. The wavelength of the first pulse is tuned to the peak of a water vapor absorption line and is called the on-line wavelength, while the second wavelength is adjusted to a water vapor spectral region with no absorption and is called the off-line wavelength. The two wavelengths are selected close to each other; therefore, the scattering by other atmospheric molecules and particles is the same for both on and off laser wavelengths and the difference in the on- and off-line return signals will be entirely

due to the absorption by water vapor molecules. Thus, the ratio of the backscattered signals at the two wavelengths can be used to calculate the water vapor concentration profile as a function of range.¹⁴⁻¹⁶

This principle was applied to the LASE instrument which is shown in the block diagram of Figure 1.1. LASE is an instrument that detects water vapor using the 815-nm water vapor absorption line. LASE measurements were found to have an accuracy better than 6% or 0.01 g/kg, whichever is greater across the entire troposphere.⁷⁻¹¹

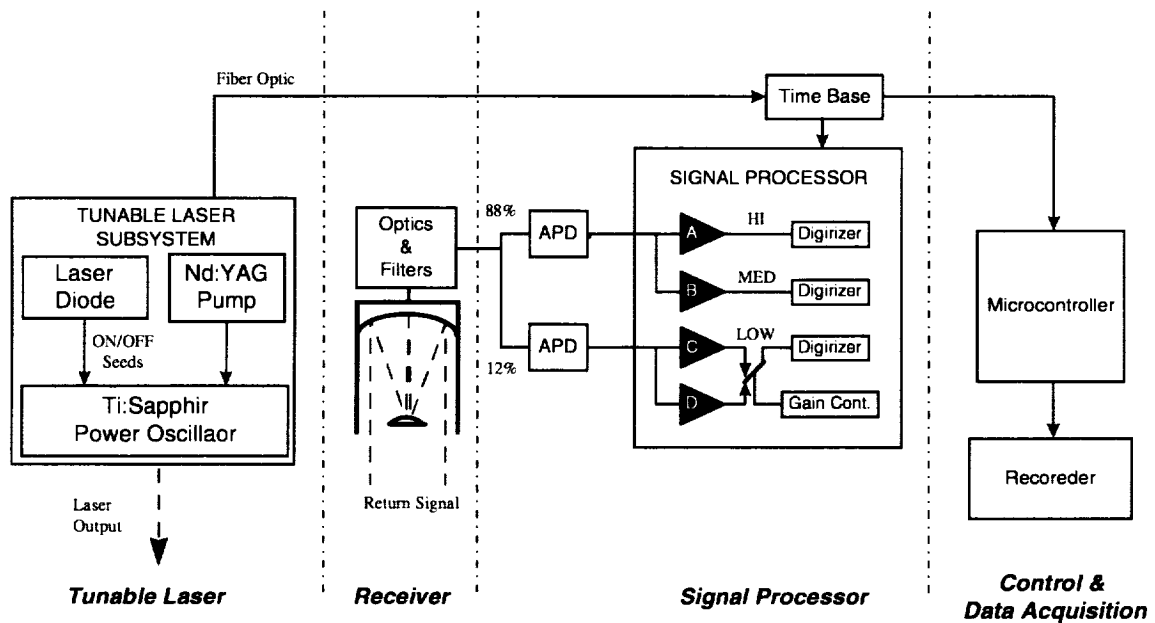


Figure 1.1 LASE system block diagram.⁷

The LASE transmitter was designed to generate two laser pulses of 30 ns duration separated by 400 μ s at a frequency of 5 Hz with a pulse energy output of 150 mJ. A Ti:Sapphire ($\text{Ti:Al}_2\text{O}_3$) power oscillator was constructed using a Nd:YAG laser as the pump source. Narrow linewidth and wavelength tuning of the $\text{Ti:Al}_2\text{O}_3$ laser is achieved by

a continuous wave 100-mW single mode diode laser performing as an injection seed source. This injected seeding allows control of the spectral linewidth to within 1 pm and provides wavelength tuning stability to ± 0.25 pm. The diode laser wavelength is locked onto the selected water absorption line and tuned by passing a fraction of its frequency modulated light through a reference cell filled with water vapor and detecting the cell transmission. The tunable diode laser seeds the pulsed laser alternately between the on-line wavelength located at the center of the water vapor absorption line and the off-line wavelength typically located 20 to 80 pm away from the on-line wavelength.⁷

The LASE receiver has a Cassegrainian telescope with a 40-cm diameter collecting area. The received light is split into two channels. The two data channels use silicon avalanche photodiodes (APDs) in order to increase the dynamic range. The first low-gain channel uses 12 % of the collected light for measuring strong return signals while the second high gain APD channel uses 88% for low signal level detection. The APD detectors for both channels were manufactured by EG&G (model C30955E) with a 1.5-mm diameter active area.⁷

The APD detector output signal is applied to a trans-impedance amplifier stage which limits the signal bandwidth to 2.5 MHz. A 1.5 MHz low-pass filter is used to set the signal bandwidth, and then the signals are applied to 12-bit, 10-MHz digitizers. Both the amplifier and the digitizer stages are mounted in a CAMAC (Computer Automated Measurements and Control) crate, which communicates with an onboard computer for data recording. The whole system is synchronized by a time-based trigger signal.⁷⁻⁹

While LASE has performed well, there are several improvements in the detection system that could be made to reduce system mass and improve performance. Eliminating

the CAMAC crate would reduce the system mass substantially, and using advanced super-low-ionization-coefficient (SLIK) APD technology could reduce the system noise, thus improving measurement range. These improvements are the subject of this research dissertation.

1.3. Research objectives

In order to obtain global atmospheric water vapor profile measurements, DIAL systems such as LASE should be incorporated in aircraft or satellite-based systems. This requires the development of DIAL systems with reduced size, mass and power consumption as well as increased measurement capabilities. This will require higher energy laser systems, but a major part of this development also must be applied to the detection system.

The research objective of this dissertation was to design, build and test an advanced, compact, low-mass water vapor DIAL detection system that is used to increase the performance of the LASE instrument and also serve as a receiver prototype for future space missions. This new detection system increase the signal-to-noise ratio (SNR) by a factor of 10 compared to the current LASE receiver. Also it was integrated into a small size suitable for mounting directly on the receiver telescope. The system consists of an advanced low noise APD, an analog circuit, a 14-bit digitizer and a digital interface to a personal computer all on one small electronic card. These goals were achieved using state-of-the-art electronic components and a newly evaluated very low noise APD detector and constructing a 10-MHz waveform digitizer which is placed as close as possible to this detector on the same card.¹⁷⁻²⁰ The APD is a very critical device in such systems, since it

directly affects the water vapor measurement accuracy and range. Therefore, the selection of this device was obtained after modeling its performance and characterizing a group of APDs from different manufacturers.^{21,22}

The design of the new DIAL detection system, the subject of this thesis, is shown schematically in Figure 1.2. The design allows the placement of both analog and digital circuits on one small-size light weight printed circuit board which includes detection and digitization sections. This scheme has the advantage of transmitting digital data for storage and analysis by a personal computer; therefore, analog signals do not have to be transmitted for long distances which reduces the system noise pick up.¹⁸⁻²⁰

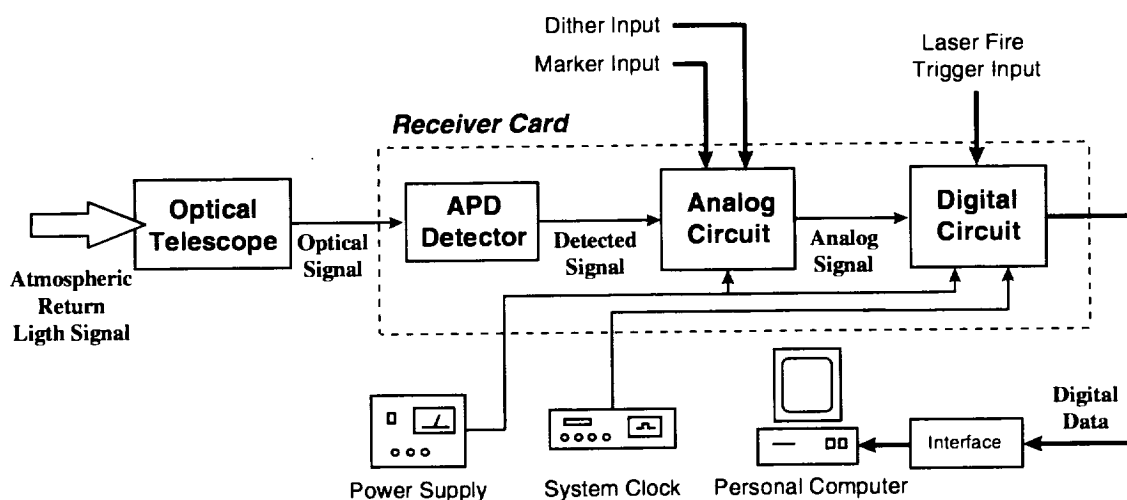


Figure 1.2 Schematic of the new DIAL receiver system.

The system design was optimized for water vapor absorption lines near 820 and 940 nm. In the receiver system, an existing telescope was used to collect and focus the lidar return signal onto the APD detector sensitive area. The APD output signal was then applied to the analog circuit for signal conditioning which includes signal saturation

protection, amplification, and filtering. In addition, this stage provides the APD with a stable bias voltage and temperature control.¹⁸⁻²⁰

The analog signal is then applied to the digital circuit to be digitized and then processed and temporarily stored. This circuit is compatible with a parallel input/output computer interface for final data storage and display, and provides monitoring of the detector high voltage bias and temperature. The whole system card is supplied with ± 5 V and ± 12 V power and a 10-MHz clock signal for digitization. This new detection system increases the accuracy and range of water vapor measurements over the current LASE receiver system.¹⁸⁻²⁰

The new detection system has the advantage of eliminating the CAMAC crate, thus reducing the mass and power consumption compared to the LASE instrument. A prototype receiver system was built, tested and evaluated. The prototype receiver system was used to measure relative aerosol profiles and actual atmospheric water vapor profiles to validate its performance.²³

CHAPTER II

AVALANCHE PHOTODIODE: THEORY AND MODEL

APDs are solid state quantum detectors suitable for low light detection in the visible and near infrared regions. These devices are commercially available from many manufacturers and are fabricated using different solid state structures. In this chapter, the basic APD structures will be described in order to develop a mathematical model for such devices. The model will be converted into an equivalent circuit and will be validated.

2.1. Avalanche photodiode structure and theory of operation

The basic structure of a PIN diode as well as three different structures of APDs and their electric field distribution is shown in Figure 2.1. The PIN diode shown in Figure 2.1a is a p-n junction with an intrinsic or lightly-doped layer sandwiched between the p and n layers. This structure serves to extend the width of the depletion region which increases the volume available for absorbing the incident photons. Also it reduces the junction capacitance, thereby reducing the RC time constant resulting in higher detection bandwidth. Thus, the response time of these devices is in the tens-of-pico-second range which corresponds to giga-hertz bandwidths.²⁴⁻²⁷ A disadvantage of PIN detectors is that they have no internal gain mechanism which reduces signal-to-noise ratio. The APD structure is similar to the PIN diode structure except for an additional gain mechanism within the device. This gain mechanism depends on the impact ionization process in which the photoelectric charge carriers, due to their high energy, can impact and cause ionization of lattice atoms generating more carriers resulting in the internal gain.²⁴⁻²⁸

As shown in Figure 2.1b, the beveled-edge APD has the simplest structure among them. It consists of a p^+ -n junction with a high resistivity n layer which increases the breakdown voltage of the device into the kilovolt range. Breakdown at the edges is prevented by beveling and making the junction very deep (in the range of 50 μm). Therefore, the dead part of the p^+ layer is usually etched away to reduce the device depth. Because the n layer is much deeper than the p^+ layer, electrons produced there are more likely to be multiplied than holes. This reduces the dark-current noise which is mostly generated by hole current. The disadvantage, however, is that only light absorbed in the p layer leads to effective multiplication and this layer has the lowest electric field. As a result, charge accumulates slowly leading to a longer response time typically in the range of tens of nanoseconds.²⁸

The reach-through structure APD and its electric field distribution are shown in Figure 2.1c. This structure consists of an absorption region and a separate multiplication region. In the absorption region, the p^+ layer at the active surface is followed by an intrinsic wide layer which increases the photon absorption depth. The emitted photo-electrons drift and reach a constant velocity. In the multiplication region, the p - n^+ layers form a thin junction with a high internal field which enhances the impact ionization process.²⁸⁻³⁰ Recently, an enhancement of the reach-through structure known as the “super low ionization ratio κ ” (SLIK) geometry has become available and is shown in Figure 2.1d.³¹ The ability of electrons and holes to “impact ionize” in order to generate additional charge carriers is characterized by the ionization coefficients α and β , for

electrons and holes respectively. The ionization coefficient represents the ionization probabilities per unit length. An important parameter is the ionization ratio, κ , given by

$$\kappa = \frac{\beta}{\alpha}. \quad (2.1)$$

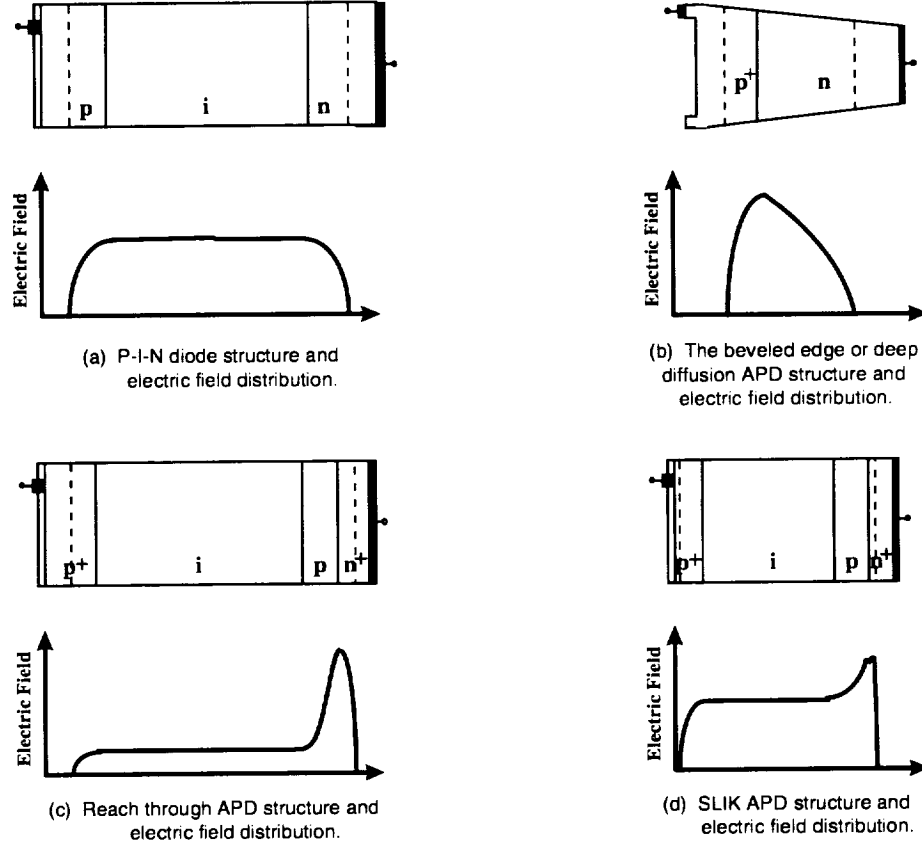


Figure 2.1 PIN diode and different APD structures with electric field distributions.

In APDs, it is desirable to reduce κ as much as possible so the multiplication process is only due to electrons, since hole current leads to high dark-current noise.²⁴ This was achieved in the SLIK structure by increasing the absorption region electric field and

merging this region with the multiplication region.³¹ Typically, the value of κ is in the range of 0.02 for the reach-through structure while it is 0.002 for the SLIK structure.³¹

2.2. Modeling of four layer avalanche photodiode

Large efforts were made to model the different structures of APDs, but little work has focused on developing an equivalent circuit for these devices.^{28,32} Chen and Liu constructed an equivalent circuit model for three layer PIN-APD and applied it to $\text{In}_{0.53}\text{Ga}_{0.47}\text{As-InP}$ PIN-APD.³³ This model was based on the study of the minority carrier generation, diffusion and drift through the different layers of the device, by applying both the rate and continuity equations. The drift-diffusion model was converted into an equivalent circuit. In this section the, Chen-Liu model will be extended to the case of four layer APDs, such as the reach-through and SLIK structures, in order to solve for the characteristics and response and to obtain an equivalent circuit for such devices.²¹ This APD model is capable of simulating the transient and steady state behavior of an APD knowing its microstructure. The model simulation results were compared to a commercial reach-through silicon APD in order to validate it.^{21,34}

A schematic of the structure of a reach-through APD as well as the internal electric field distribution are shown in Figures 2.2a and 2.2b respectively. As discussed earlier, the field profile shown in Figure 2.2b distinguishes the two main regions within the device. The first is the absorption region which is used to absorb the incident photons to generate photo-charge carriers and drift these carriers into the second region. The second region is the multiplication region which has a relatively smaller depth with higher field. In this region, the photo-generated carriers produce additional carriers by the impact ionization

process. For the sake of simplicity in this model, the electric field profile will be approximated by two step functions as shown in Figure 2.2c. The lower field value is for the absorption region that is covered by the i layer, while the higher field value is for the multiplication region which is almost covered by the p layer. The electric field will be neglected in the outer highly-doped layers since they have relatively smaller depletion widths. Under these approximations the device currents in the p^+ -i and p - n^+ interfaces will be due to the diffusion currents of the minority carriers from the highly doped layer, and the drift current of the generated charge carriers in the internal regions.²¹

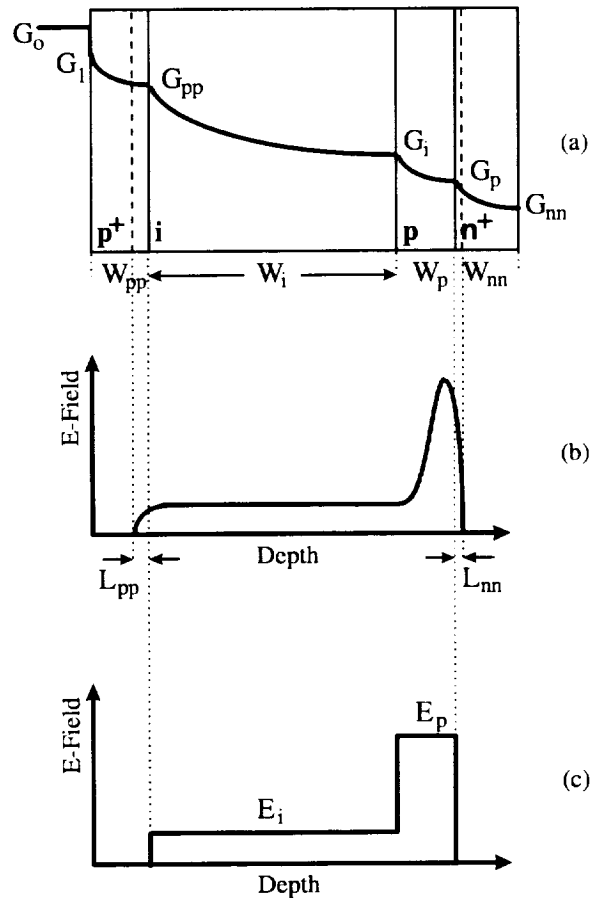


Figure 2.2 (a) Schematic diagram of a four layer APD showing light absorption through the device with (b) simulated³⁴ and (c) approximate electric field profiles.

The absorption profile along the device depth is also shown in Figure 2.2a. Considering the input optical power P_{in} at a wavelength λ , the incident photon flux is given by

$$G_o = \frac{P_{in}}{hc} \lambda, \quad (2.2)$$

where h is Plank's constant and c is the speed of light in vacuum. A part of this flux will reflect back at the APD surface and the other part will penetrate the device and will be given by

$$G_i = G_o (1 - R), \quad (2.3)$$

where R is the APD surface reflection coefficient. Since the electron-hole pair photo-generation rate is directly proportional to the number of absorbed photons, this rate will be given as (in s^{-1}) for the p^+ , i , p and n^+ layers, respectively, by

$$G_{pp} = G_i \cdot [1 - \exp(-\alpha_{pp} W_{pp})] \quad (2.4)$$

$$G_i = G_i \cdot \exp(-\alpha_{pp} W_{pp}) \cdot [1 - \exp(-\alpha_i W_i)] \quad (2.5)$$

$$G_p = G_i \cdot \exp(-\alpha_{pp} W_{pp} - \alpha_i W_i) \cdot [1 - \exp(-\alpha_p W_p)] \quad (2.6)$$

$$G_{nn} = G_i \cdot \exp(-\alpha_{pp} W_{pp} - \alpha_i W_i - \alpha_p W_p) \cdot [1 - \exp(-\alpha_{nn} W_{nn})], \quad (2.7)$$

where α_{pp} , α_i , α_p and α_{nn} are the absorption coefficients and W_{pp} , W_i , W_p and W_{nn} are the widths of the p^+ , i , p and n^+ layers, respectively.

2.2.1. Rate equations

Considering a reverse bias device, the rate of increase of the number of electrons in the p^+ layer (minority carriers) will be proportional to the photo-generation rate and

opposed by the recombination and diffusion. Thus the rate equations for the electrons in the p^+ layer is given by

$$\frac{dP_{ppe}}{dt} = G_{pp} - \frac{P_{ppe}}{\tau_{ppe}} - \frac{I_{ppe}}{q} \quad (2.8)$$

Similarly for the n^+ layer, the rate equation of the holes (minority carriers) is given by

$$\frac{dP_{nnh}}{dt} = G_{nn} - \frac{P_{nnh}}{\tau_{nnh}} - \frac{I_{nnh}}{q} \quad (2.9)$$

where P_{ppe} and P_{nnh} are the number of excess electrons and holes, τ_{ppe} and τ_{nnh} are the electron and hole life times for the p^+ and n^+ respectively, I_{ppe} is the electron diffusion current from the p^+ to the i region, I_{nnh} is the hole diffusion current from the n^+ to the p region and q is the magnitude of the electron charge.

In the i region, both electrons and holes are considered as minority carriers, and the rate of increasing any type of these carriers will be equal to the photo-generation rate in this region plus the impact ionization rates initiated by any electrons or holes minus the recombination rate. Also, for electrons this process will be affected by the electron diffusion and drift from the p^+ region and to the p region respectively. For holes, it will be affected by the hole drift from and to the p and p^+ regions respectively. Therefore, the rate equation for electrons in the i region has the form

$$\frac{dP_{ie}}{dt} = G_i + v_{ie}\zeta_{ie}P_{ie} + v_{ih}\zeta_{ih}P_{ih} + \frac{I_{ppe}}{q} - \frac{P_{ie}}{\tau_{ier}} - \frac{P_{ie}}{\tau_{iet}} \quad (2.10)$$

where v_{ie} and v_{ih} are the electron and hole velocity in the i region, ζ_{ie} and ζ_{ih} are the electron and hole impact ionization rates and τ_{ier} and τ_{iet} are the electron recombination

life-time and electron transient time in the i region respectively. For holes, the rate equation is

$$\frac{dP_{ih}}{dt} = G_i + v_{ih} \zeta_{ih} P_{ih} + v_{ie} \zeta_{ie} P_{ie} + \frac{P_{ph}}{\tau_{pht}} - \frac{P_{ih}}{\tau_{ihr}} - \frac{P_{ih}}{\tau_{iht}}, \quad (2.11)$$

where τ_{pht} , τ_{ihr} and τ_{iht} are the hole transient time in the p region, hole recombination life time in the i region and the hole transient time in the i region respectively. It should be noted that equations (10) and (11) are equal due to the charge neutrality condition. For the reach-through APD, the impact ionization terms can be neglected and the photo-generation and drift terms are the dominant. This assumption is not valid for the SLIK structure APD since the electric field in that region is relatively higher causing the impact ionization to occur earlier.³¹

Finally, since the p layer is lightly doped, both electrons and holes will be considered as minority carriers, and the rate equations will be similar to that of the i region and are given by

$$\frac{dP_{pe}}{dt} = G_p + v_{pe} \zeta_{pe} P_{pe} + v_{ph} \zeta_{ph} P_{ph} + \frac{P_{ie}}{\tau_{iet}} - \frac{P_{pe}}{\tau_{per}} - \frac{P_{pe}}{\tau_{pet}} \quad (2.12)$$

and

$$\frac{dP_{ph}}{dt} = G_p + v_{ph} \zeta_{ph} P_{ph} + v_{pe} \zeta_{pe} P_{pe} + \frac{I_{mh}}{q} - \frac{P_{ph}}{\tau_{phr}} - \frac{P_{ph}}{\tau_{pht}}, \quad (2.13)$$

where ζ_{pe} and ζ_{ph} are the electron and hole impact ionization rates in the p region, τ_{iet} , τ_{per} and τ_{pet} are the electron transient time in the i region, recombination life-time in the p region and transient time in the p region respectively and τ_{phr} is the hole recombination life-time in the p region. Also, due to the charge neutrality condition, equations (2.12) and

(2.13) are equal. The dominant terms in these relations will be the impact ionization and the drift terms for both the reach-through and SLIK APDs, while the absorption term can be neglected especially for deep devices.

2.2.2. Continuity equations

The diffusion current from the p^+ layer can be obtained by applying the continuity equation which is given by

$$D_e \frac{d^2 n_e}{dx^2} - \frac{(n_e - n_{e0})}{\tau_{ppe}} + \frac{g_{pp}(x)}{A} = 0, \quad (2.14)$$

where D_e is the electron diffusion coefficient in the p^+ region, n_e is the electron density profile, n_{e0} is the electron equilibrium density and A is the device area. The boundary conditions for this layer are; at $x = 0$, $n_e = n_e(0)$ and at $x = W_{pp}$, $n_e = 0$. If L_{pp} is the diffusion depth in the p^+ region, the diffusion coefficient is given by

$$D_e = \frac{L_{pp}^2}{\tau_{ppe}}, \quad (2.15)$$

and $g_{pp}(x)$ is photo-generation rate of the charge carriers along the depth of the p^+ layer.

Referring to equation (2.3), $g_{pp}(x)$ is given by

$$g_{pp}(x) = G_1 \cdot \alpha_{pp} \cdot \exp(-\alpha_{pp} x) \quad ; 0 \leq x \leq W_{pp}. \quad (2.16)$$

The solution of equation (2.14) is given by

$$n_e(x) = n_{e0} + c_1 \exp(-\alpha_{pp} x) + [n_e(0) - n_{e0} - c_1] \frac{\sinh\left(\frac{W_{pp} - x}{L_{pp}}\right)}{\sinh\left(\frac{W_{pp}}{L_{pp}}\right)} - [n_{e0} - c_1 \exp(-\alpha_{pp} W_{pp})] \frac{\sinh\left(\frac{x}{L_{pp}}\right)}{\sinh\left(\frac{W_{pp}}{L_{pp}}\right)} \quad (2.17)$$

where c_1 is a constant given by

$$c_1 = \frac{(1-R)\alpha_{pp}\tau_{ppe}}{Ahc(1-\alpha_{pp}^2 L_{pp}^2)} P_{in} . \quad (2.18)$$

To evaluate $n_e(0)$, equation (2.17) is applied to the condition

$$P_{ppe} = A \int_0^{w_{pp}} (n_e - n_{eo}) dx , \quad (2.19)$$

and solving for $n_e(0)$ and substituting its value in equation (2.17), the electron diffusion current from the p^+ region can be determined from

$$I_{ppe} = +qAD_c \left. \frac{dn_e}{dx} \right|_{x=w_{pp}} . \quad (2.20)$$

Similarly, to evaluate the hole diffusion current I_{nnh} from the n^+ region, we apply the hole continuity equation which is given by

$$D_h \frac{d^2 n_h}{dx^2} - \frac{(n_h - n_{ho})}{\tau_{nnh}} + \frac{g_{nn}(x)}{A} = 0 , \quad (2.21)$$

where D_h is the hole diffusion coefficient in the n^+ region, n_h is the hole density profile and n_{eo} is the hole equilibrium density. The boundary conditions in this region are at $x = 0$, $n_h = 0$ and at $x = W_{nn}$, $n_h = n_h(0)$. The hole diffusion coefficient can be obtained using the diffusion length L_{nn} in the n^+ region by

$$D_h = \frac{L_{nn}^2}{\tau_{nnh}} , \quad (2.22)$$

and $g_{nn}(x)$ is photo-generation rate of the charge carriers along the n^+ layer depth.

Referring to (2.3) $g_{nn}(x)$ is given by

$$g_{nn}(x) = G_i \cdot \exp(-\alpha_{pp} W_{pp} - \alpha_i W_i - \alpha_p W_p) \cdot \alpha_{nn} \cdot \exp(-\alpha_{nn} x) ; 0 \leq x \leq W_{nn} \quad (2.23)$$

The solution of equation (2.21) is:

$$n_h(x) = n_{ho} + c_2 \exp(-\alpha_{nn} x) + [n_h(0) - n_{ho} - c_2 \exp(-\alpha_{nn} W_{nn})] \frac{\sinh\left(\frac{x}{L_{nn}}\right)}{\sinh\left(\frac{W_{nn}}{L_{nn}}\right)} - [n_{ho} - c_2] \frac{\sinh\left(\frac{W_{nn} - x}{L_{nn}}\right)}{\sinh\left(\frac{W_{nn}}{L_{nn}}\right)}, \quad (2.24)$$

where c_2 is a constant given by

$$c_2 = \frac{(1-R)\lambda\alpha_{nn}\tau_{nnh}}{Ahc(1-\alpha_{nn}^2 L_{nn}^2)} \exp(-\alpha_{pp} W_{pp} - \alpha_i W_i - \alpha_p W_p) P_{in}. \quad (2.25)$$

Similarly, to evaluate $n_h(0)$ we use

$$P_{nnh} = A \int_0^{W_{nn}} (n_h - n_{ho}) dx. \quad (2.26)$$

Substituting its value in equation (2.21), we get a complete expression for the hole density in the n^+ . The hole diffusion current will then be evaluated using

$$I_{nnh} = -qAD_h \left. \frac{dn_h}{dx} \right|_{x=0}. \quad (2.27)$$

2.2.3. Avalanche photodiode equivalent circuit

For the purpose of constructing an equivalent circuit for the APD, we assume a constant C_o which is equivalent to a capacitor. Referring to equations (2.4), (2.5), (2.6) and (2.7), equations (2.8), (2.9), (2.10) and (2.13) can be written respectively as

$$I_{opp} = \frac{P_{in}}{V_{opp}} = C_o \frac{dV_{pp}}{dt} + \frac{V_{pp}}{R_{pp}} + I_{ppe} \quad (2.28)$$

$$I_{onn} = \frac{P_{in}}{V_{onn}} = C_o \frac{dV_{nn}}{dt} + \frac{V_{nn}}{R_{nn}} + I_{nnh} \quad (2.29)$$

$$I_{oi} = \frac{P_{in}}{V_{oi}} = C_o \frac{dV_i}{dt} + \frac{V_i}{R_{ir}} + \frac{V_i}{R_{it}} - I_{ppe} - I_{is} \quad (2.30)$$

$$I_{op} = \frac{P_{in}}{V_{op}} = C_o \frac{dV_p}{dt} + \frac{V_p}{R_{pr}} + \frac{V_p}{R_{pt}} - I_{nnh} - I_{ps}, \quad (2.31)$$

where the excess charge carriers are converted to voltages, using C_o , and are given by

$$V_{pp} = q \frac{P_{ppe}}{C_o}, \quad V_i = q \frac{P_{ie}}{C_o}, \quad V_p = q \frac{P_{ph}}{C_o}, \quad \text{and} \quad V_{nn} = q \frac{P_{nnh}}{C_o} \quad (2.32)$$

The rest of the parameters are given by

$$V_{opp} = \frac{1}{q} \cdot \frac{P_{in}}{G_{pp}}, \quad V_{oi} = \frac{1}{q} \cdot \frac{P_{in}}{G_i}, \quad V_{op} = \frac{1}{q} \cdot \frac{P_{in}}{G_p} \quad \text{and} \quad V_{onn} = \frac{1}{q} \cdot \frac{P_{in}}{G_{nn}} \quad (2.33)$$

$$R_{pp} = \frac{\tau_{ppe}}{C_o} \quad (2.34)$$

$$R_{nn} = \frac{\tau_{nnh}}{C_o} \quad (2.35)$$

$$R_{ir} = \frac{\tau_{ier}}{C_o}, \quad R_{it} = \frac{\tau_{iet}}{C_o} \quad (2.36)$$

$$I_{is} = C_o V_i (v_{ie} \zeta_{ie} + v_{ih} \zeta_{ih}) \quad (2.37)$$

$$R_{pr} = \frac{\tau_{phr}}{C_o}, \quad R_{pt} = \frac{\tau_{phl}}{C_o} \quad (2.38)$$

$$I_{ps} = C_o V_p (v_{pe} \zeta_{pe} + v_{ph} \zeta_{ph}). \quad (2.39)$$

The diffusion currents I_{ppe} and I_{nnh} will be given respectively by

$$I_{ppe} = \frac{V_{pp}}{R_{pd}} + \beta_p P_{in} + I_{ppeo} \quad (2.40)$$

$$I_{nnh} = \frac{V_{nn}}{R_{nd}} + \beta_n P_{in} + I_{nnho} , \quad (2.41)$$

where

$$R_{pd} = R_{pp} \left[\cosh \left(\frac{W_{pp}}{L_{pp}} \right) - 1 \right] \quad (2.42)$$

$$R_{nd} = R_{nn} \left[\cosh \left(\frac{W_{nn}}{L_{nn}} \right) - 1 \right] \quad (2.43)$$

$$\beta_p = q \frac{(1-R)}{hc} \lambda \frac{\alpha_{pp} L_{pp}^2}{(1 - \alpha_{pp}^2 L_{pp}^2)} \left\{ \alpha_{pp} \exp(-\alpha_{pp} W_{pp}) + \frac{[\exp(-\alpha_{pp} W_{pp}) - 1]}{\alpha_{pp} L_{pp}^2 \left[\cosh \left(\frac{W_{pp}}{L_{pp}} \right) - 1 \right]} \right. \\ \left. + \frac{\left[\cosh \left(\frac{W_{pp}}{L_{pp}} \right) + 1 \right] \exp(-\alpha_{pp} W_{pp})}{L_{pp} \sinh \left(\frac{W_{pp}}{L_{pp}} \right)} \right\} \quad (2.44)$$

$$\beta_n = q \frac{(1-R)}{hc} \lambda \frac{\alpha_{nn} L_{nn}^2}{(1 - \alpha_{nn}^2 L_{nn}^2)} \exp(-\alpha_{pp} W_{pp} - \alpha_i W_i - \alpha_p W_p) \left\{ \frac{\left[\cosh \left(\frac{W_{nn}}{L_{nn}} \right) + 1 \right]}{L_{nn} \sinh \left(\frac{W_{nn}}{L_{nn}} \right)} \right. \\ \left. + \frac{[\exp(-\alpha_{nn} W_{nn}) - 1]}{\alpha_{nn} L_{nn}^2 \left[\cosh \left(\frac{W_{nn}}{L_{nn}} \right) - 1 \right]} - \alpha_{nn} \right\} \quad (2.45)$$

$$I_{ppeo} = q \frac{AD_e n_{eo}}{L_{pp}} \left[\frac{1 + \cosh\left(\frac{W_{pp}}{L_{pp}}\right)}{\sinh\left(\frac{W_{pp}}{L_{pp}}\right)} \right] \quad (2.46)$$

$$I_{nnho} = q \frac{AD_h n_{ho}}{L_{nn}} \left[\frac{1 + \cosh\left(\frac{W_{nn}}{L_{nn}}\right)}{\sinh\left(\frac{W_{nn}}{L_{nn}}\right)} \right]. \quad (2.47)$$

Using equation (2.28) through (2.31) and the definition of the diffusion currents given in equations (2.40) and (2.41), the APD equivalent circuit can be constructed as shown in Figure 2.3. The APD output current, I_{APD} , will be given by

$$I_{APD} = I_{ppe} + I_i + I_p + (C_s + C_j) \frac{dV_{BIAS}}{dt} + I_d, \quad (2.48)$$

where

$$I_i = \frac{V_i}{R_{it}} \quad (2.49)$$

$$I_p = \frac{V_p}{R_{pt}}, \quad (2.50)$$

and C_s and C_j are the parasitic and junction capacitance, I_d is the sum of the leakage and tunneling currents and V_{BIAS} is the applied APD bias voltage.

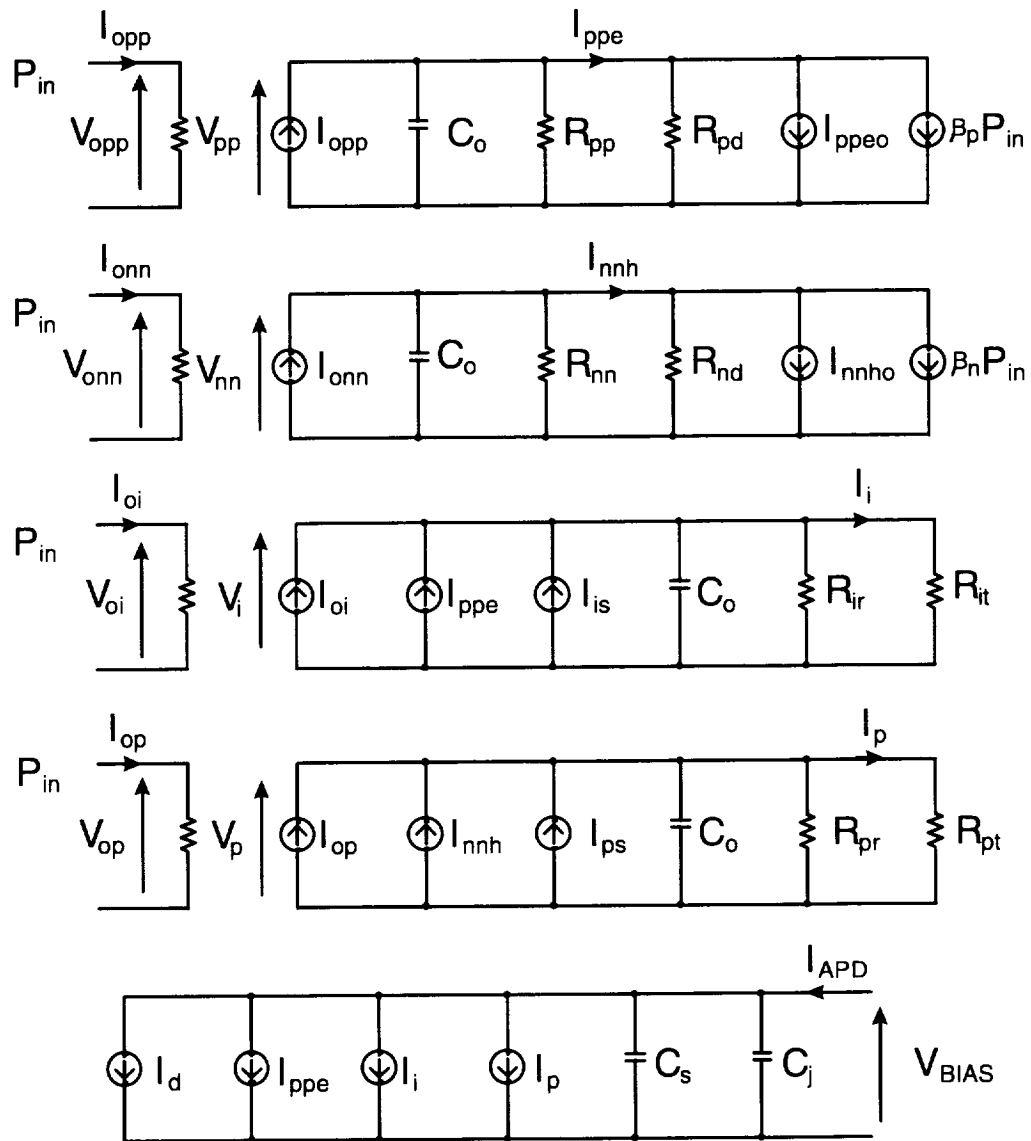


Figure 2.3 APD equivalent circuit

2.3. Model validation

In order to validate the discussed model, a silicon reach-through APD was simulated. The APD is manufactured by EG&G (model number C30902E). Table 2.1 gives some parameters of this APD as well as for silicon at a temperature of 300 K.^{30,35-40}

Table 2.1 Silicon APD parameters at 300 K.

Parameter	Value
$A(\text{mm}^2)$	0.196
$W_{pp}(\mu\text{m})$	1
$W_i(\mu\text{m})$	15
$W_p(\mu\text{m})$	4.5
$W_{nn}(\mu\text{m})$	10
R	0.35
$N_A(\text{cm}^{-3})$	5×10^{12}
$N_D(\text{cm}^{-3})$	5×10^{12}
$N_i(\text{cm}^{-3})$	1.5×10^{10}
$D_e(\text{cm}^2\text{s}^{-1})$	34.2
$D_h(\text{cm}^2\text{s}^{-1})$	11.9
$\tau_{ppe}(\mu\text{s})$	30
$\tau_{nnh}(\mu\text{s})$	20
$\tau_{ier}(\mu\text{s})$	30
$\tau_{phr}(\mu\text{s})$	20

2.3.1. Model parameters

The values of the electric field were approximated by two step functions under constrain of equal bias voltage for both the simulated and approximated profiles shown earlier in Figure 2.2b and 2.2c. The electric field step function relates to the applied bias voltage by

$$E_i = V_{\text{BIAS}} / (W_i + 6.5W_p) \quad \text{and} \quad E_p = 6.5E_i, \quad (2.51)$$

where E_i and E_p are the electric in the i and p layers respectively. Since the device built-in potential is neglected, these relations are only valid near the breakdown bias voltage of the APD.

The impact ionization coefficients for electrons and holes as a function of the electric field in the range of 2×10^5 to 5×10^5 V/cm were obtained from ref. 41 and applied for the i and p regions.

The electron and hole drift velocity can be obtained as a function of the electric field from the empirical formula³⁷

$$v = v_s \frac{E/E_c}{\left[1 + (E/E_c)^\beta\right]^{1/\beta}}, \quad (2.52)$$

where v_s is the carrier saturation velocity, E_c is the critical field defined by the ratio of the carrier saturation velocity to its mobility and β is a constant. The values of the saturation velocity, mobility and the constant β are 1×10^7 and 0.8×10^7 cm/s, 1320 and 460 cm²/Vs and 0.9 and 0.8 respectively for electrons and holes.

The absorption coefficients for the various layers were assumed the same. The absorption coefficient as a function of the wavelength of the incident light was taken from ref. 42 for the 800 to 1100 nm wavelength range. The data were fitted using polynomial fit and applied to the model.

2.3.2. Steady state performance

The spectral response of the APD under investigation was obtained from the manufacturer data sheet and is shown in Figure 2.4 at a temperature of 295 K.³⁴ Also shown in the same figure the spectral response obtained after applying the model to the

same device assuming a 215 V bias voltage and 300 K temperature. Comparing the two curves we note that the model spectral response has a lower responsivity values with a maximum near the 870 nm. The responsivity \mathfrak{R} was obtained using the relation.

$$\mathfrak{R} = \frac{I_{APD}}{P_{in}}. \quad (2.53)$$

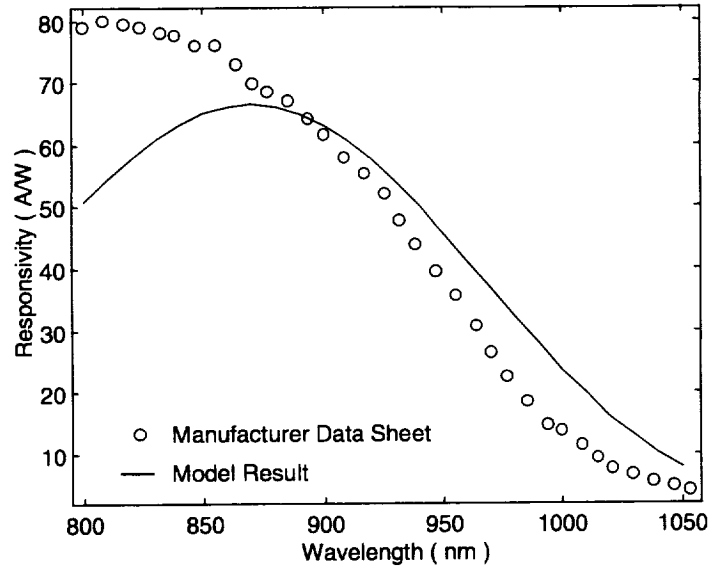


Figure 2.4 APD spectral response obtained from the manufacturer data sheet at 295 K and from the model at 300 K and 215 V.

The quantum efficiency variation with wavelength is shown in Figure 2.5 obtained from the manufacturer and the model.^{21,34} In order to obtain this relation, the model was run while setting the impact ionization coefficients to zero. Therefore, the responsivity gave a measure to the quantum efficiency η according to the relation.

$$\eta = \frac{hc}{q\lambda} \mathfrak{R} \Big|_{G=1} \quad (2.54)$$

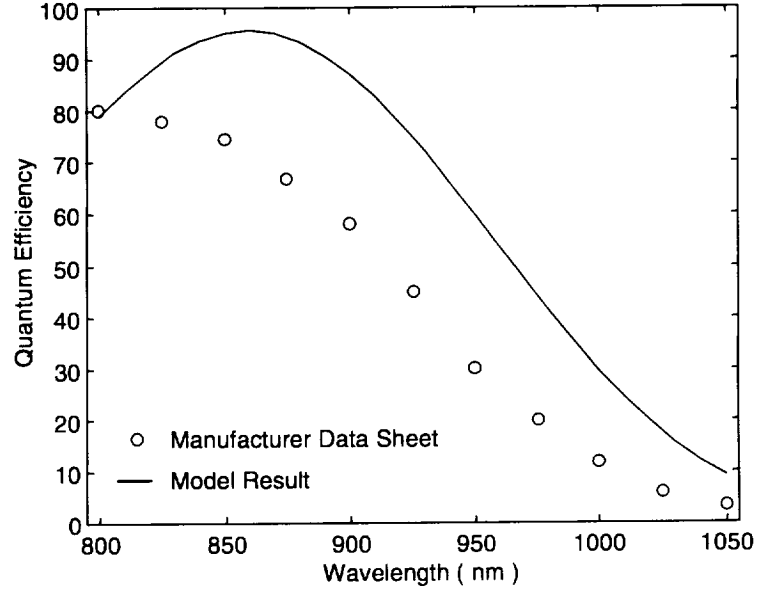


Figure 2.5 APD quantum efficiency versus wavelength at obtained form the manufacturer and form the model at 300 K and 215 V bias.

Although the results of figures 2.4 and 2.5 indicate the lack of accuracy in the model parameters, the device gain variation with respect to wavelength can be predicted at the given operating voltage. The accuracy of the model parameters is very critical in the model stability and results, especially in the multiplication region, as will be shown later.

Figure 2.6 shows the responsivity variation with bias voltage obtained form ref. 34 and the model both assuming constant wavelength of 830 nm.^{21,34} The model result indicates that the APD bias voltage of 215 V is near-breakdown voltage which is about 8 V less than the manufacturer corresponding voltage at similar temperature.

As shown in Figure 2.6, the large deviation between the simulated results and the manufacturer data at low operating bias voltage was expected. This was indicated earlier in equation (2.51) since the natural built-up potential is neglected. This affects the impact ionization rate leading to decrease of the responsivity at lower voltage biases.

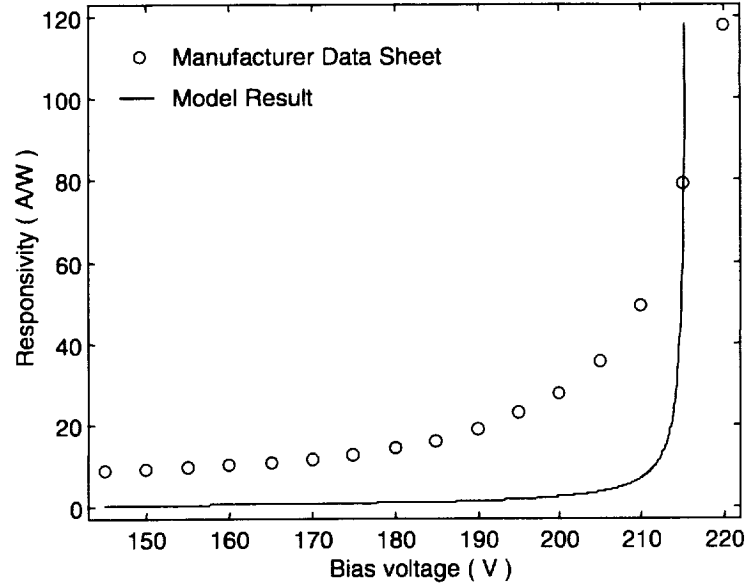


Figure 2.6 APD responsivity variation with bias voltage at 830 nm obtained from the manufacturer data sheet at 293 K and from the model at 300 K.

To demonstrate the model sensitivity to the device multiplication width, W_p , referring to (2.13) we can define a multiplication stability constant C_{MS} as

$$C_{MS} = v_{ph} \zeta_{ph} + v_{pe} \zeta_{pe} - \frac{1}{\tau_{phr}} - \frac{1}{\tau_{pht}}, \quad (2.55)$$

in which the electron impact ionization and the hole transient time terms are the dominant. The value of this constant determines the stability of the device since it controls the feedback of the multiplication process. Figure 2.7 investigates the variation of the stability constant and the resulted responsivity with the width of the multiplication region W_p . The values of the multiplication stability constant shown to the left of the stability limit line are positive while the values to the right are negative. W_p affect the hole transient time according to

$$\tau_{pht} = \frac{W_p}{v_{ph}}. \quad (2.56)$$

It was found that any positive values of C_{MS} causes model failure because it causes an unstable positive feedback. Although the magnitude of the negative values of C_{MS} controls the APD gain and thus its responsivity, the practical value of the responsivity lies within a small region of the multiplication width. The bias voltage is another factor affecting the multiplication stability constant, since it controls both the charge carrier velocity and impact ionization coefficients. This explains the sudden increase of the responsivity with bias voltage as shown in Figure 2.6.

Practically, when manufacturing these devices, it is very hard to keep the multiplication width consistent. This explains why similar APD part numbers from the same manufacturer have different operating bias voltages with different characteristics.²²

The value of the responsivity is also affected by the initial doping concentration of the donor atoms in the n^+ region. As shown in Figure 2.8, at a constant acceptor concentration, increasing the doping level of the donors reduces the responsivity. A doping level of 5×10^{12} is a reasonable limit for manufacturing devices with similar characteristics as the device under investigation. Shown in the same figure the effect of the acceptor atoms doping concentration in the p^+ region, at constant donor concentration, which has a smaller effect.

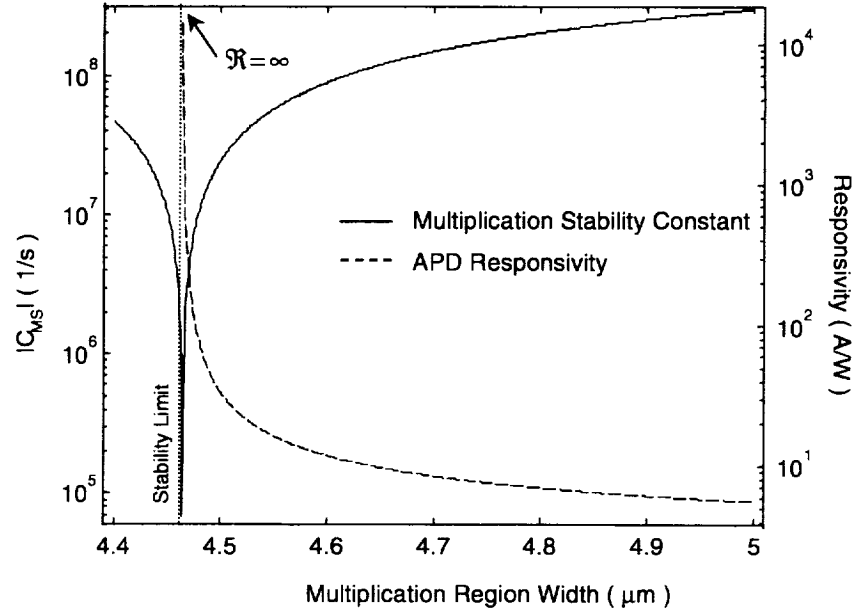


Figure 2.7 Responsivity and multiplication stability constant variation with the multiplication width, obtained at 800 nm wavelength and 215 V bias.

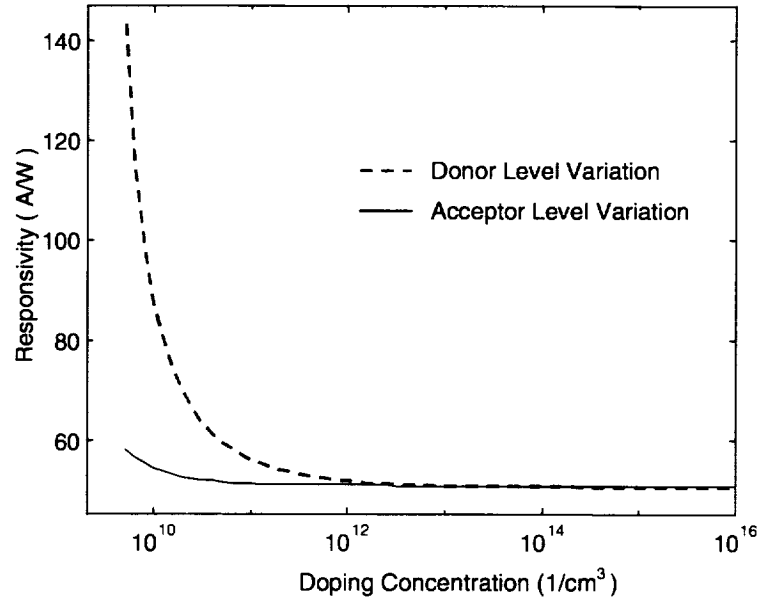


Figure 2.8 Donor and acceptor concentration effect on the APD responsivity at 800 nm wavelength and 215 V bias voltage.

As pointed out by applying the continuity equation, increasing the donor concentration increases the electron diffusion current to the absorption region. This has

the effect of increasing the recombination rate with holes leading to decrease the photo generated carries (holes) resulting in responsivity reduction. Increasing the donor level more, responsivity saturation will be resulted, since the diffused electrons recombined with all the generated holes. A Similar effect occurs due the increase of the acceptor level. However, since the acceptor diffusion current take place in the multiplication region where the photo charge carriers got multiplied, it has a lower effect on the responsivity.

One application of this model is to study the effect of different APD parameters on its characteristics. This is demonstrated in Figure 2.9, which gives the effect of changing the width of the i or absorption region on the spectral response. By increasing the absorption depth the spectral response curve shifts to the infrared. Referring to equation (2.51), the degradation of the peak points is due to the considerable reduction in the electric field of the absorption region, E_i , since the bias voltage was assumed constant (215 V) for all cases. This spectral response shift is known commercially as infrared enhanced APDs.

The value of the absorption width, W_i , is limited by two main factors. Reducing W_i to a low value limits the absorption depth and the acceleration distance required by the charge carriers to gain sufficient energy for the impact ionization process. On the other hand, increasing W to large value causes losses in the carriers due to recombination.

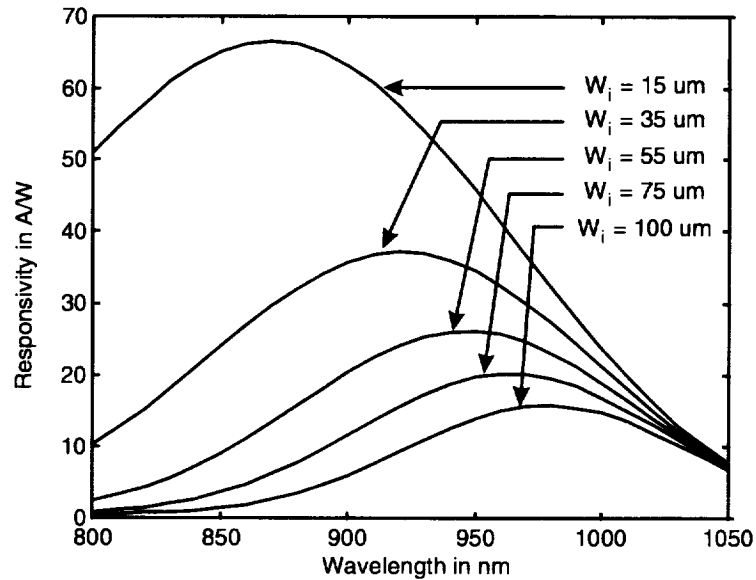


Figure 2.9 Spectral response variation with the width of the absorption region obtained at 300 K and 215 V.

2.3.3. Transient performance

To test the APD model in the transient state, an input optical pulse was simulated and applied to the model. This pulse had a square waveform with 100 ps duration and 1 μW amplitude at 800 nm. The APD output current is shown in Figure 2.10 for different operating bias voltage. The rise time was observed to be constant at about 80 ps. The fall times were 450 and 780 ps for 140 and 215 V bias voltages respectively. This indicates that the rise time has a negligible variation with bias voltage, while the fall time increases with the increase in the voltage. The rise time generally depends on the speed of the photon absorption process within the device; therefore, it has nothing to do with the bias voltage. On the other hand, the bias voltage affects the speed of the charge carriers and their number. That's why it affects the fall time. The sudden changes in the APD current

shown in Figure 2.10 at the rising and falling instances are due to the sharp edges of the square wave of the simulated input power.

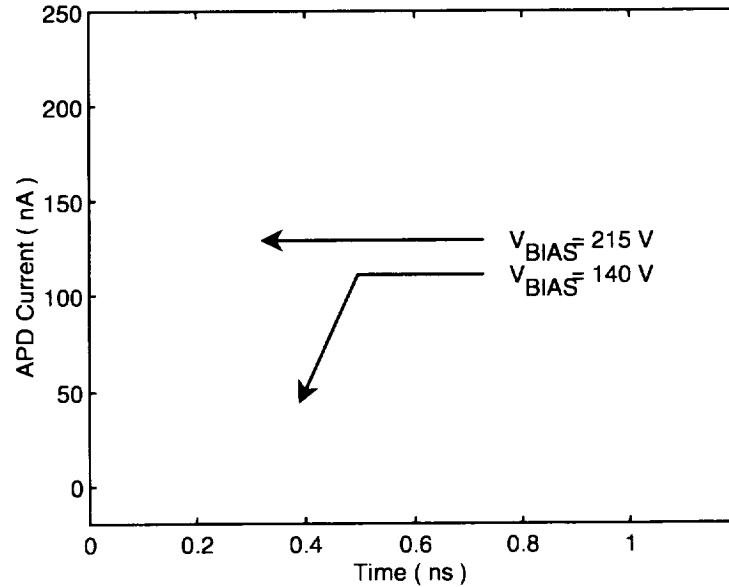


Figure 2.10 APD output current with a square wave input power of 100 ps duration and 1 μ W amplitude at 800 nm, obtained at 140 and 215 voltage biases.

This model is also suitable for performing some tests to the APD which are practically destructive to the device. Figure 2.10 shows the simulated APD output current during breakdown. This was simulated assuming an applied bias voltage of 215.7 V and a step input power of 1 μ W as shown in the same figure. The breakdown time, shown in the same figure, was defined as the time interval between applying the input power and the rapid increase of the APD current up to 10% of its normal value at starting. The 10 % value was suitable enough since the APD current has a rapid increase to infinity indicating device damage. Figure 2.11 shows the relation between the magnitude of the breakdown

voltage and the breakdown time indicating that increasing the applied breakdown voltage speeds up the breakdown time.

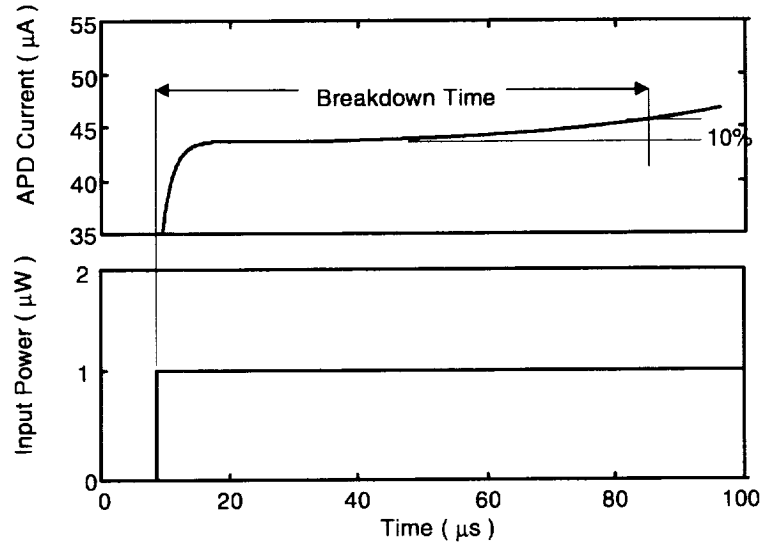


Figure 2.11 APD output current during breakdown simulated with an applied voltage bias of 215.7 V and a step input power of 1 μW . The breakdown time is defined as the time interval between applying the input power and the increase of the APD current up to 10% of its steady-state value.

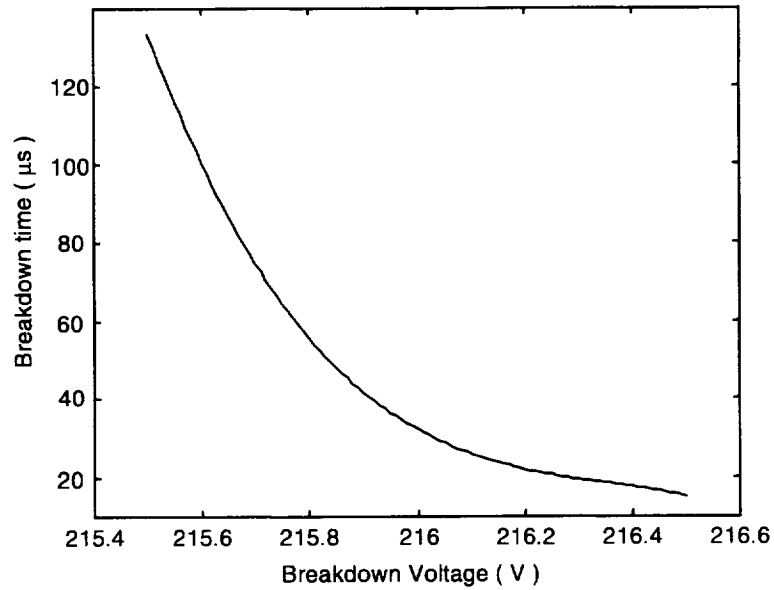


Figure 2.12 APD breakdown time variation with breakdown voltage bias.

For low light detection, an APD can be operated in the Geiger mode or photon counting.^{31,43-46} In this mode, the device is biased with a voltage above its breakdown value leading to increase the device gain. Therefore, it will be very sensitive and any absorption of a small amount of photons will cause avalanche breakdown which can be detected as current pulse. In this mode of operation, it is important to apply such over-breakdown bias for short time intervals known as the counting bin to control the avalanche breakdown. Increasing the counting bin will cause damage to the device.³¹

Although the switching action was assumed to the input power, the characteristics shown in Figure 2.11 is important for defining the bin duration for an APD operating in the Geiger mode. With the current model, switching the bias voltage was difficult to obtain. This is due to the dependence of many parameters on the bias voltage which had to be calculated before starting the simulation.

2.3.4. Model conclusion and limitations

A drift-diffusion model for four layer APDs has been developed. This model is a modification of the Chen and Liu PIN-APD model. The model was used to drive an APD equivalent circuit and can be used to simulate the device transient and steady state response. For the validation purpose the model parameters were chosen as close as possible to an actual device. Reasonable agreement between the model results and the manufacturer data sheet indicated the validity of the model. This model can be used for device structure modification as to enhance the spectral response of a device or for destructive tests such as breakdown.²¹

There were many assumptions associated the construction of this model which make it limited. The limitations of the model include the effect of temperature, low bias voltage operation, simulation of the device characteristics and response near saturation and noise modeling.

CHAPTER III

AVALANCHE PHOTODIODE: CHARACTERIZATION AND SELECTION

A group of silicon based avalanche photodiode (APD) detectors, with different structures, were characterized from different manufacturers. The main concern in these experiments was to calibrate these APDs and to investigate the influence of their high voltage bias and temperature on the APD responsivity and to examine their active area uniformity and noise performance.²² With these results, an optimal detector was chosen for the new atmospheric water vapor DIAL detection system. The detection system can operate at 720, 820 or 940 nm wavelengths which correspond to water vapor absorption lines.^{18,22,47}

The APDs that were characterized are given in Appendix A as well as a summary of the characterization results. The results of the reach-through structure (RTS) APD C30955E⁴⁸ currently used in the LASE instrument and the super low ionization coefficient (SLIK) APD C30649E⁴⁹ will be discussed in detail in this chapter. Both APDs are manufactured by EG&G.⁴⁷⁻⁴⁹

3.1. Experimental setup

The experimental setup for the APD responsivity calibration is shown in Figure 3.1. The light source was a broad-band halogen lamp supplied by a stabilized power supply to insure stable spectrum and intensity. The lamp output is filtered by a 600-nm long-pass filter to prevent higher order dispersion of shorter wavelengths from being collected in

first-order dispersion in the range of 600 to 1100 nm. The chopper was used to modulate the optical signal for dc offset elimination at the detector output and to allow for phase-locked detection. The monochromator was used to separate the light input into its spectral components. An integrating sphere was used to diffuse the exiting light to insure uniform intensity at the detector.^{22,45,47,50}

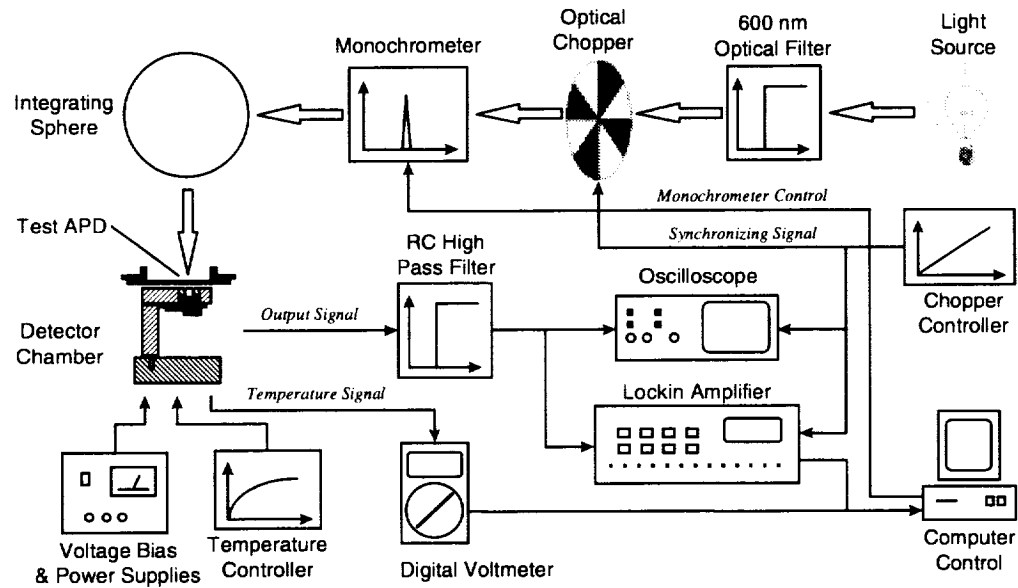


Figure 3.1 APD experimental setup for the spectral response determination.

The APD output was filtered by a high-pass filter to eliminate dark current and background radiation offsets. An oscilloscope was used to check the detected signal and to obtain its peak-to-peak value, V_{p-p} , and a lock-in amplifier was used to accurately measure the signal rms value, $V_{lock-in}$. The chopper controller adjusted the chopping frequency to 200 Hz and supplied synchronization signals for the other instruments.^{22,45}

The APDs are biased using a high voltage source. The APD current variation, representing the change in the light intensity, was converted to a voltage signal using a

trans-impedance amplifier (TIA).^{24-27,51-52} The TIA configuration is shown in Figure 3.2a, where R_f is the amplifier feedback resistance and R and C act as a low pass filter to eliminate any bias voltage ripples. The test detector was placed on a printed circuit board and put inside a chamber, as shown in Figure 3.2b. The chamber was located on a three-dimensional, computer-controlled, translation stage for alignment. Nitrogen gas flow was used to prevent condensation of water vapor on the detector window at low temperature and to avoid dust accumulation. A temperature controller and a thermoelectric cooler (TEC) were used to fix the temperature of the APD under test.⁵³ Water circulation provided forced cooling to the TEC for low temperature settings. The APD temperature was measured with a temperature sensor and a digital voltmeter. A personal computer sent commands to the monochromator to adjust the wavelength for the spectral scan, and it acquired the lock-in amplifier and the temperature readings using a GPIB data acquisition card.^{22,47}

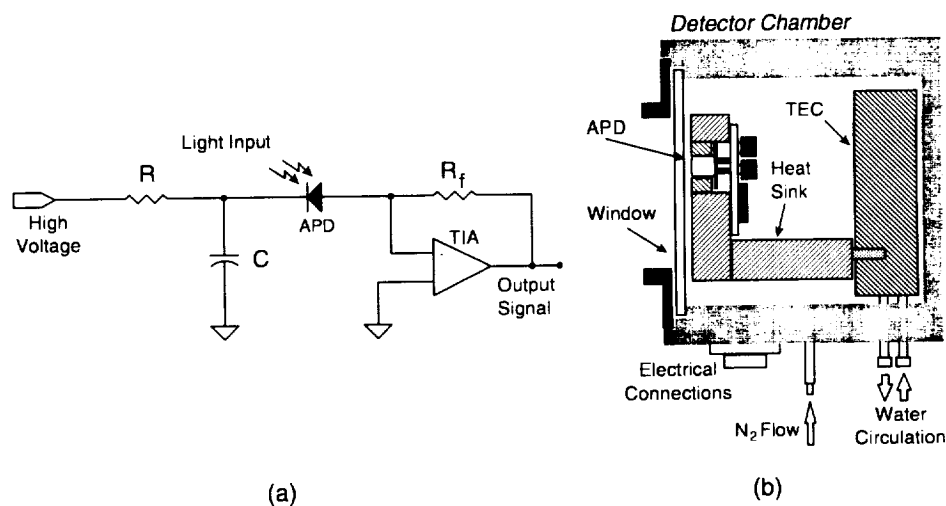


Figure 3.2 (a) APD bias circuit and the trans-impedance amplifier connection
(b) APD chamber used to mount and stabilize the device temperatures.

The APD spectral response was measured over a 600 to 1100 nm wavelength range. Comparison was made with a NIST (National Institute of Standards and Technology) calibrated reference detector by placing each detector in the same uniform light field at the same position. The distance between the light outlet and the detector active area was 150 mm. For alignment purposes, a microscope with a 200 μm depth of focus was used to position all detectors as shown in Figure 3.3. Applying the inverted square function, the worst-case deviation of the intensity at the detector was $\pm 0.53\%$. Errors due to positioning of the detectors can cause absolute calibration uncertainty of less than 1%. The microscope was placed on a kinematic mount (1 μm placement precision) so that it could be removed from the optical path during the wavelength scan and precisely replaced in the path for detector positioning.^{22,47}

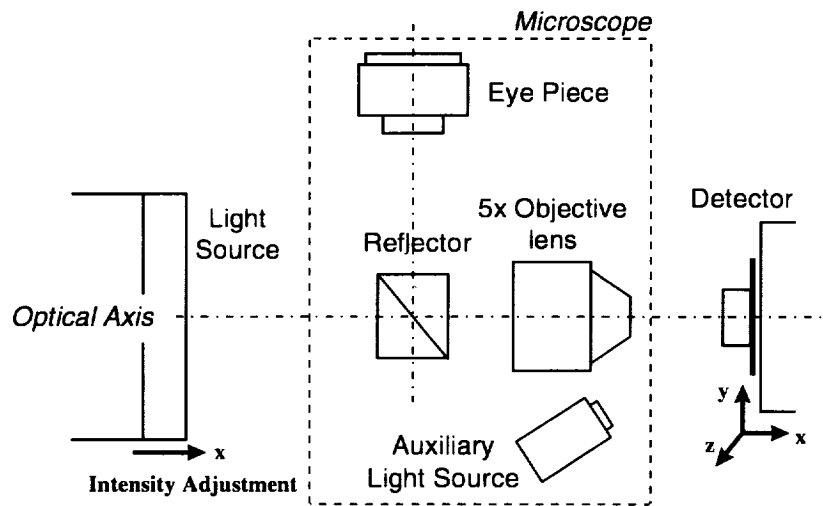


Figure 3.3 APD alignment setup using microscope.

3.2. Avalanche photodiode calibration

The slits of the monochromator were adjusted to have a wavelength band-pass of 10 nm. Because the halogen spectral maximum output was at 690 nm, the monochromator was set at this value and the chopping factors were determined for both the reference and test detectors using the relation

$$CF = \frac{V_{\text{lock-in}}}{V_{\text{p-p}}} \quad (3.1)$$

Knowing the spectral response of the reference detector, shown in Figure 3.4a, the responsivity of the test detectors was determined by comparison using the relation

$$\mathfrak{R}_d = \frac{V_{d(\text{lock-in})}}{V_{r(\text{lock-in})}} \cdot \frac{CF_r}{CF_d} \cdot \frac{R_r}{R_d} \cdot \frac{A_r}{A_d} \cdot \mathfrak{R}_r \quad (3.2)$$

at each wavelength increment of 10 nm, where \mathfrak{R}_r and \mathfrak{R}_d are the responsivity of the reference detectors and test detector respectively, $V_{r(\text{lock-in})}$ and $V_{d(\text{lock-in})}$ are their output voltages, all at the same wavelength. CF_r and CF_d are the chopping factors, R_r and R_d are the feedback resistors and A_r and A_d are the sensitive areas of the reference and test detectors respectively.^{22,47}

The spectral response of the tested detectors is shown in Figure 3.4b. To compare the results with the manufacturer data sheets, room temperature and manufacturer specified bias voltage were used. The APD responsivity is directly proportional to the wavelength of the incident light.^{24-27,54} This is true as indicated in Figure 3.4, for wavelengths from 600 nm to the point where the response begins to roll off. Ideally, the roll off point would be sharp and correspond to the energy band-gap of silicon. At this cutoff, the responsivity decreases sharply due to insufficient energy in the incident photons

for the generated electrons to overcome the band-gap energy, resulting in reduction of the APD quantum efficiency. The deviation from the ideal cutoff found in our characterized APDs was mainly due to charge collection inefficiency of photons outside the depletion region of the APD which was dependent on the type and level of the doping materials used to manufacture the device.²⁸

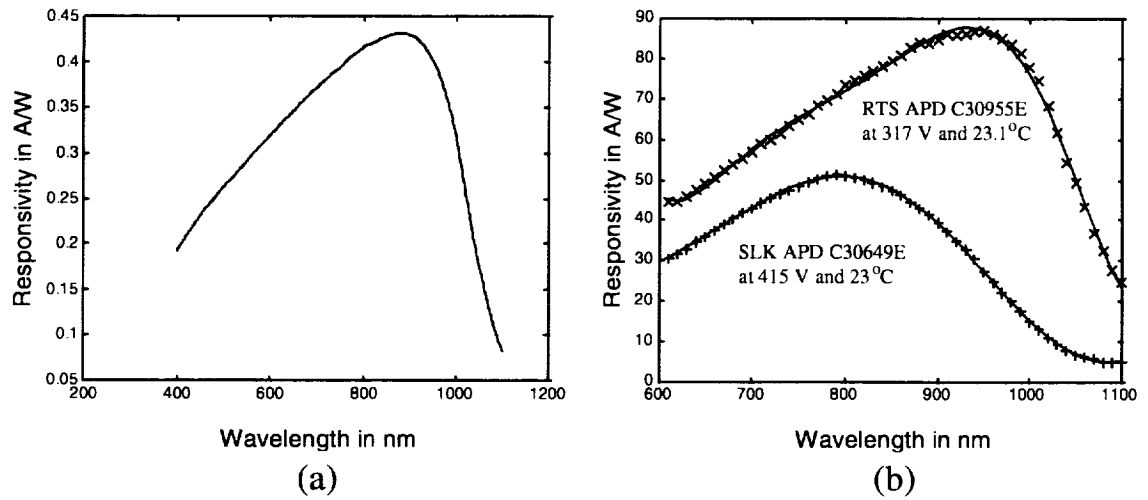


Figure 3.4 Spectral response of the (a) reference detector and (b) test detectors.

3.3. Temperature dependent responsivity

At fixed bias voltage and wavelength, the responsivity of an APD detector increases with decreasing temperature. Low temperature operation of an APD leads to an increased output signal due to the increase in the device gain. Low temperature operation also decreases the dark current noise level, which results in increasing the detector signal-to-noise ratio.^{26-27,55-58}

Experiments investigating the effect of APD temperature on the spectral response were performed. An empirical relationship for the responsivity versus temperature was

obtained. The nitrogen gas purge and the water circulation allowed the APD operating temperature to be adjusted from nearly 0 °C to room temperature. It is important to remember that a lower operating temperature causes the detector breakdown voltage to decrease; therefore, the APD voltage bias must be chosen carefully while performing this test to avoid device destruction.²²⁻⁴⁷

The setup shown in Figure 3.1 was used but only for the test detectors in this experiment. During the experiment, the detector voltage bias was kept constant to insure that the spectral response variation is only due to changes in temperature. Using the alignment setup shown in Figure 3.3, the detector position with respect to the light source was adjusted to the same value of the responsivity calibration experiment to insure the same input light intensity.

The temperature controller shown in Figure 3.1 fixed the operating point for each spectral scan. For each temperature set point, the system was allowed to reach equilibrium before proceeding with the experiment. This whole procedure was repeated for each APD under investigation.

For each APD the following characterization results were presented:

- The APD detector output voltage variation with wavelength, $\{V_n(\lambda)\}$
- The APD temperature variation with wavelength, $\{T_n(\lambda)\}$

Ideally, the temperature should be kept constant during this experiment. This was not true in our case due to some deficiencies in the temperature controller used in the experimental setup. Therefore, we had to record the temperature for each wavelength increment $\{T_n(\lambda)\}$. To obtain the APD temperature, T_n , this data set was averaged according to²²

$$T_n = \overline{\{T_n(\lambda)\}}. \quad (3.3)$$

At the same temperature T_n and using the calibration data, the detector output voltage variation was converted to a responsivity variation with respect to wavelength. This procedure was repeated for every temperature setting giving the spectral response variation with temperature shown in Figures 3.5a and 3.5b for the C30649E and C30955E, respectively.

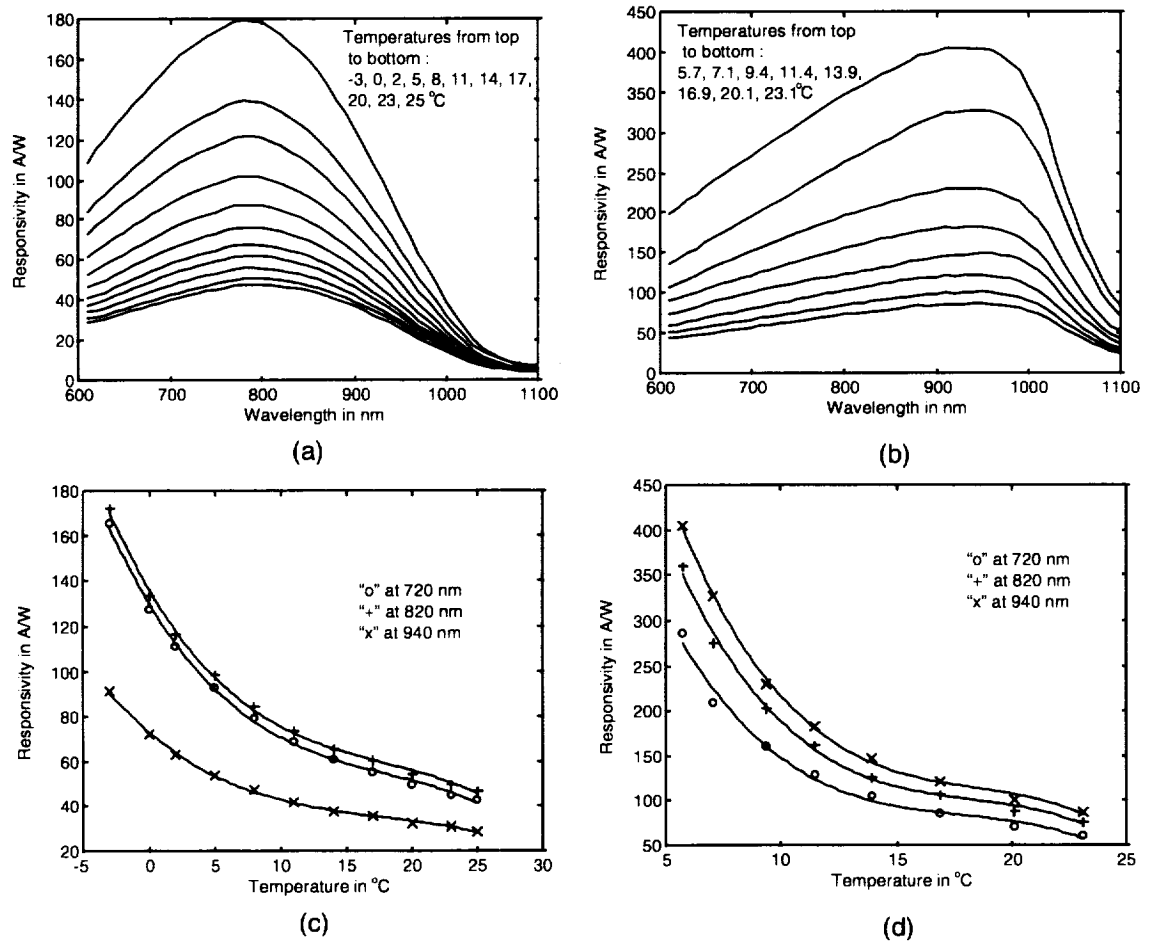


Figure 3.5 APD spectral response and responsivity variation with temperature for the (a) SLIK C30649E and (b) RTS C30955E structures respectively.

To obtain the responsivity variation with temperature, the analysis of the data starts by constructing a responsivity vector, $\{\mathfrak{R}(T)\}$, and a temperature vector, $\{T\}$, at a certain wavelength, λ_x , as shown in the following:

$$\{\mathfrak{R}(T)\} = \{\mathfrak{R}_1(\lambda_x) \quad \mathfrak{R}_2(\lambda_x) \quad \Lambda \quad \mathfrak{R}_n(\lambda_x) \quad \Lambda \quad \mathfrak{R}_N(\lambda_x)\} \quad (3.4)$$

$$\{T\} = \{T_1 \quad T_2 \quad \Lambda \quad T_n \quad \Lambda \quad T_N\}. \quad (3.5)$$

Applying a polynomial curve fit the responsivity variation with temperature at λ_x , took the form

$$\mathfrak{R}(T)|_{\lambda_x} = \sum_{m=0}^M a_m \cdot T^m, \quad (3.6)$$

where M is the curve fit order and N is the index for maximum temperature. The responsivity-versus-temperature relations for the SLIK and RTS APDs are shown in Figures 3.5c and 3.5d. The relations for the rest of the APDs are given in Appendix A.

This experiment determines the APD temperature stability requirements by obtaining the responsivity partial derivative with respect to temperature which is given by

$$\left. \frac{\partial \mathfrak{R}(T)}{\partial T} \right|_{\lambda_x} = \sum_{m=0}^M m \cdot a_m \cdot T^{(m-1)}. \quad (3.7)$$

For example, a temperature deviation (ΔT) of 0.1 °C near an operating temperature of 10 °C for the 820 nm wavelength at rated bias voltage will result in a responsivity deviation of $\Delta \mathfrak{R} = 0.3$ and 2.2 A/W, leading to a relative error of 0.4% and 1.2% for the SLIK and RTS structures, respectively. This indicates that the SLIK structure is more stable with respect to temperature variation. This fact is clear from Figure 3.6 which shows the relative error in the APD responsivity as a function of temperature at the three water vapor absorption wavelengths of interest, assuming a 1 °C temperature variation. Also

clear from this figure is that the responsivity relative error due to temperature variation does not depend that much on the operating wavelength.⁴⁷

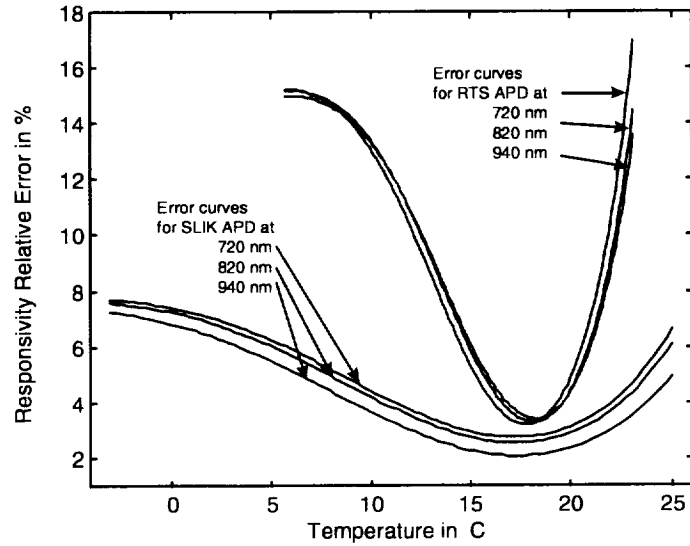


Figure 3.6 SLIK and RTS APD structures relative error in responsivity due to 1 °C temperature variation obtained at 720, 820 and 940 nm water vapor absorption wavelengths.

3.4. Bias voltage dependent responsivity

At fixed temperature and wavelength, the responsivity of an APD increases with increasing bias voltage up to the breakdown voltage. This is due to the increased internal electric field leading to the transfer of more energy to the photo-charge carriers which enhances the impact ionization process. Bias voltage above breakdown causes rapid charge carrier generation which usually leads to device damage.^{24-47,59}

This experiment investigated the effect of the APD bias voltage variation on the spectral response and obtained a responsivity versus bias voltage relation at the water vapor DIAL wavelengths of interest. Similar to the previous experiment the setup shown

in Figure 3.1 was used for the test APDs. During the experiment, the APD temperature was kept constant to insure that the spectral response variation is only due to the bias voltage. The detector position with respect to the light source was adjusted to the same value of the responsivity calibration experiment to insure the same light intensity input.

Using the high voltage supply, the detector bias is set to a certain value and the temperature was stabilized by the temperature controller. Then, the output peak-to-peak voltage was measured using the oscilloscope and its rms value was measured using the lock-in amplifier to calculate the chopping factor. Next, the scan sequence started from 600 to 1100 nm with a step increment of 10 nm. For each step increment the wavelength, output voltage and temperature were recorded using the computer. Finally, the experiment was repeated for a set of different bias voltages. This procedure was repeated for each APD under investigation.

At the end of this experiment, each APD had a group of data files describing its output voltage variation with wavelength at a given bias voltage. The value of the bias voltage, V_{Bn} , is measured directly from the high voltage supply. For a certain APD at a given bias voltage the available data was as follows:

- The APD detector output voltage variation with wavelength, $\{V_n(\lambda)\}$
- The APD temperature variation with wavelength, $\{T_n(\lambda)\}$

The detector output voltage variation was converted to responsivity variation with respect to wavelength using the calibration data. This procedure was repeated for every voltage bias setting giving the spectral response variation with bias voltage.

To obtain the responsivity variation with bias voltage at a certain wavelength λ_x , we use the spectral response variation with bias voltage to form two vectors. A responsivity vector $\{\mathfrak{R}(V_B)\}$ and a voltage bias vector $\{V_B\}$ where defined as

$$\{\mathfrak{R}(V_B)\} = \{\mathfrak{R}_1(\lambda_x) \ \mathfrak{R}_2(\lambda_x) \ \Lambda \ \mathfrak{R}_n(\lambda_x) \ \Lambda \ \mathfrak{R}_N(\lambda_x)\} \quad (3.8)$$

$$\{V_B\} = \{V_1 \ V_2 \ \Lambda \ V_n \ \Lambda \ V_N\} \quad (3.9)$$

Using a polynomial curve fit, the responsivity variation with bias voltage is given by

$$\mathfrak{R}(V)_{\lambda_x} = \sum_{m=0}^M a_m \cdot V^m, \quad (3.10)$$

where M is the curve fit order and N is the index for maximum voltage bias. This analysis was applied to each APD at 720, 820 and 940 nm wavelengths.^{22,47}

The experimental results are shown in Figure 3.7 for the C30649E and C30955E APDs. For each detector, the spectral response variation with bias voltage is shown on the set of curves to the left and the responsivity variation with bias voltage on the right. The results for the rest of the APDs are given in Appendix A.

To obtain the APD bias voltage stability, the partial derivative of the responsivity with respect to bias voltage is obtained from

$$\left. \frac{\partial \mathfrak{R}(V)}{\partial V} \right|_{\lambda_x} = \sum_{m=0}^M m \cdot a_m \cdot V^{(m-1)}. \quad (3.11)$$

For example, with both APDs operating at their rated bias voltage and for a voltage deviation (ΔV) of 1 V at 820 nm wavelength, the responsivity deviations ($\Delta \mathfrak{R}$) are 2.28 and 1.54 A/W for the SLIK and RTS APDs, respectively, which is a relative error of 4.6% and 2% for the SLIK and RTS structures, respectively. This indicates that the RTS structure is less sensitive to voltage variations. This fact is clear from Figure 3.8 which

shows the relative error in the APD responsivity as a function of the bias voltage normalized to the APD rated bias. These relations are given at the three water vapor absorption wavelengths of interest assuming 1-V deviation in the bias voltage. Also clear from this figure is that the responsivity relative error due to bias voltage does not depend significantly on the operating wavelength.⁴⁷

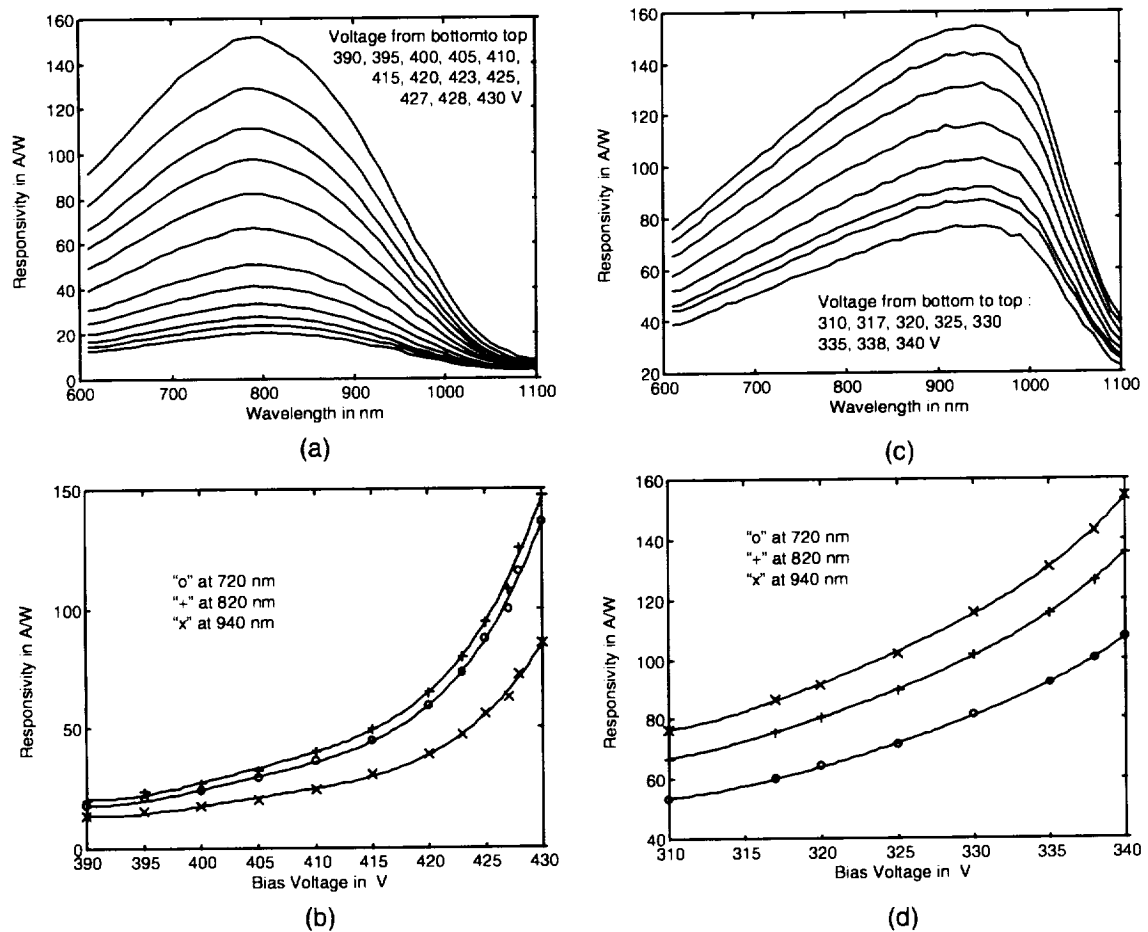


Figure 3.7 APD spectral response and responsivity variation with bias voltage for the (a) SLIK and (b) RTS structures respectively.

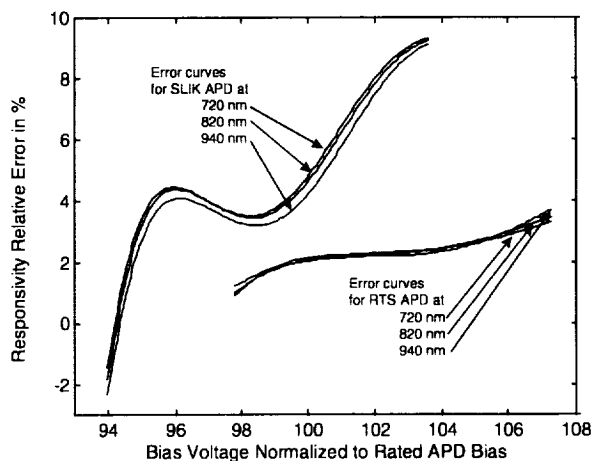


Figure 3.8 SLIK and RTS APD structures relative error in responsivity versus normalized bias voltage due to 1-V deviation in the bias voltage obtained at 720, 820 and 940 nm water vapor absorption wavelengths.

3.5. Responsivity uniformity scan

The APD sensitive area can be considered as a group of point detectors distributed along its surface. Ideally, this distribution is uniform with each of these point detectors having the same responsivity for similar operating conditions; therefore, the overall responsivity distribution should be constant along the APD surface. Practically, this is not true due to defects in the APD manufacturing process.^{22,28}

In this experiment, we investigated the uniformity of the APD responsivity along its surface and determined its active area. This can be achieved using a relatively small spot size light source and scan it across the detector area measuring the APD output voltage as a function of light spot position resulting in a responsivity map of the APD area. The small spot size light source was achieved using the setup shown in Figure 3.9. A 633-nm He:Ne laser was used to obtain a light beam which was focused by a microscope objective. The position of the detector was adjusted with the computer controlled three-dimensional

translation stage. The motion of the detector was adjusted so that the focused laser beam spot and the APD sensitive area remained in the same plane. A neutral density filter was used to avoid APD saturation.

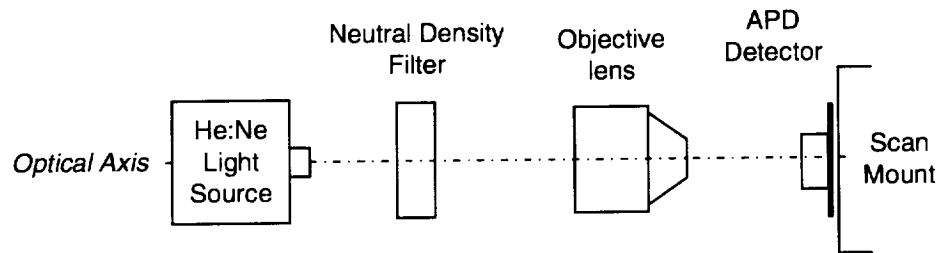


Figure 3.9 Responsivity uniformity scan setup.

The laser focusing optical system was calibrated to determine the displacement between the laser focus at its minimum waist and the visual focus of the microscope system shown in Figure 3.3. In order to obtain this calibration a pinhole was mounted on a three-dimension translation stage, as shown in Figure 3.10. The laser focus was determined by positioning the pinhole such that the maximum laser output was observed on the detector. The laser focus was measured with the micrometer on the translation stage. The visual focus was determined by viewing the best focus of the pinhole through the eyepiece. The test detectors were positioned by finding the visual focus of the detector surface and then translating to the laser focus by the calibrated displacement as described above.^{28,60}

During the scan sequence, the detector moves in a two-dimension sequence with a fixed step size then the data is plotted and analyzed. The normalized surface scan results for the tested APDs are shown in Figure 3.11.

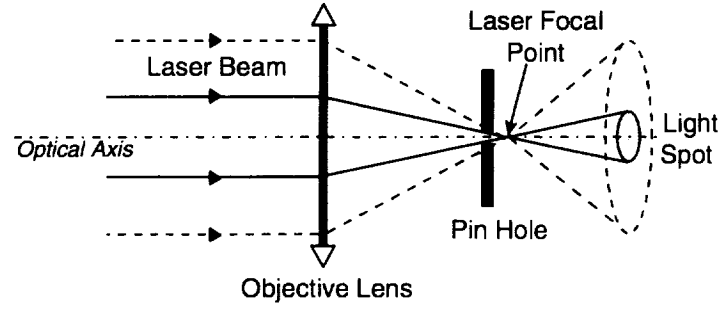


Figure 3.10 Laser focal point evaluation setup using a pinhole.

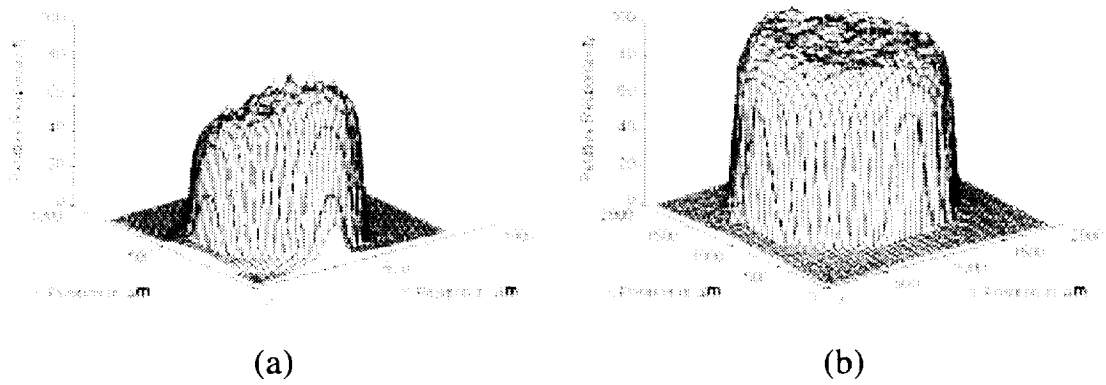


Figure 3.11 APD surface scan for the (a) SLIK and (b) RTS APDs.

In some DIAL systems, the light intensity is focused on a small region of the detector. Therefore, these surface scan data can be used to calculate the responsivity correction factor since the calibration of the APD considers the average responsivity over the entire detector active area. On the other hand, the surface scan data can be used to determine the APD hot spots which are points on the APD surface with very high responsivity relative to the average. The hot spots may cause a problem since at high light intensities the charge carriers concentration will increase at this position leading to increased power dissipation at this spot possibly resulting in local damage of the APD area.²²

The areas for the SLIK and RTS APDs were measured to be 0.238 and 1.692 mm² which is close to the manufacturer values of 0.25 and 1.5 mm², respectively. The non-uniformity of the APD surface was defined by the ratio of the standard deviation to the mean of the responsivity along the surface. The non-uniformity was measured to be 14.9% and 6.1% for the SLIK and RTS APD, respectively, which indicates that this particular RTS device is more uniform relative to the SLIK APD.

3.6. Noise measurement

The APD noise measurements were performed using a spectrum analyzer with a one Hz normalized spectrum at 10 kHz. Appropriate care was taken to insure that the detector dark current was the dominant noise source. The measured power spectral noise, n (in dB_m), was converted to the APD noise current spectral density, I_n , by the equation

$$I_n = \frac{\sqrt{10^{0.1n} \cdot R_L \cdot 10^{-3}}}{R_f}, \quad (3.12)$$

where R_L is a 50 Ω APD load resistance. Table 3.1 gives the noise current spectral density. The noise equivalent power (NEP) was obtained using the relation²⁴⁻⁴⁷

$$NEP = \frac{I_n}{\mathfrak{R}}. \quad (3.13)$$

The NEP for both SLIK and RTS APDs is shown in Figure 3.12. The SLIK structure shows a lower noise than the RTS. This might be due to the smaller detector area; thus, the figure-of-merit (D^*) was obtained for the tested detector at its responsivity calibration bias voltage and temperature using the relation^{25-27,58}

$$D^* = \frac{\sqrt{A}}{NEP}. \quad (3.14)$$

This confirmed the fact that the SLIK structure has lower noise at shorter wavelengths up to about 950 nm. The results of this experiment are very important since it directly indicates that the SLIK would be the best detector for the water vapor DIAL detection system based on its lower noise.⁴⁷

Table 3.1 APD noise measurement results.

APD	λ Nm	I_n $A/Hz^{1/2}$	NEP $fW/Hz^{1/2}$	D^* $cmHz^{1/2}/W$
C30649E	720	2.3×10^{-13}	1.8	2.77×10^{13}
	820		1.7	2.90×10^{13}
	940		3.1	1.57×10^{13}
C30955E2	720	1.7×10^{-12}	28.0	4.75×10^{12}
	820		22.2	5.99×10^{12}
	940		19.4	6.84×10^{12}

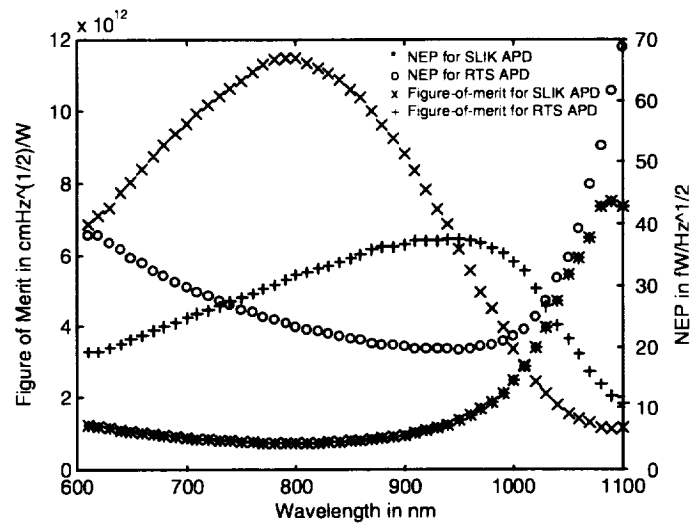


Figure 3.12 SLIK and RTS APD structures noise-equivalent-power and figure-of-merit measurements as a function of wavelength obtained with rated bias voltage at room temperature.

3.7. Frequency response

This experiment required the investigation of the responsivity variation of the SLIK APD with respect to the frequency of the input signal and to determine its cutoff frequency. This was done to check the manufacturer stated bandwidth and compare this bandwidth to the whole system bandwidth according to the Nyquist criterion.⁵¹ APDs have a very wide bandwidth in the order of giga-hertz, but due to the existence of the TIA in the APD package, the frequency response will be limited by the internal amplifier bandwidth which will be on the order of tens mega-hertz.^{24-27,39-40}

The experimental setup of Figure 3.1 was modified for the APD frequency response and shown in Figure 3.13. It consists of a 720-nm laser diode controlled by a pulse generator. The power supply is used to bias the laser diode driver circuit consisting of a buffer amplifier and a voltage-to-current converter. The output laser beam was split in order to apply part of the optical signal to the reference detector while the other part was applied to the test APD. The reference detector bandwidth was used to measure the input signal applied to the APD under test. Next, the output of both detectors was measured by a digital oscilloscope and a spectrum analyzer. The function of the oscilloscope was to check the magnitude of the output signal while the spectrum analyzer measured the frequency spectrum. When necessary, a neutral density filter was used to reduce the light intensity to avoid saturating the test APD. The electronic high pass filter was used to eliminate dc offsets in the detector output.²²

Using the setup discussed above and after aligning the optics, we set the APD bias voltage to its manufacturer specified value at room temperature. Then, we applied an optical signal to the detectors after choosing a suitable neutral density filter and checked their

output using the oscilloscope. Next, setting the frequency of the input optical signal to a certain value f_i , by using the pulse generator the amplitude of the fundamental frequency components of the APD input and the output signals, R_i and C_i respectively, are recorded in dB_m using the spectrum analyzer. This corresponds to one data point in the frequency domain. By changing the frequency setting of the pulse generator and repeating the same procedures, we obtained the complete frequency scan starting from 100 kHz to 1 MHz, with frequency increments of 100 kHz for frequencies lower than 1 MHz, and a 1-MHz step for frequencies up to 20 MHz. The spectrum analyzer was set to a frequency range from 50 kHz to 20 MHz with each data point averaged 30 times.

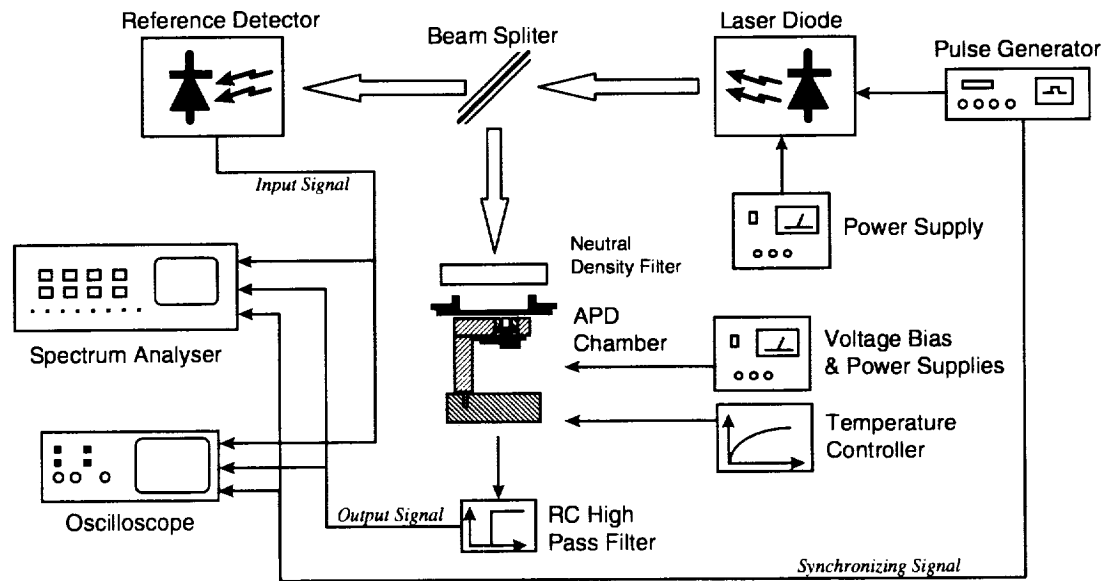


Figure 3.13 Frequency response experimental setup.

After collecting the data in the frequency range of interest, the analysis was done using MATLAB.⁶¹ First, the data was stored in three vectors, $\{f\}$, $\{C\}$ and $\{R\}$,

equivalent to the frequency increments and the corresponding outputs and inputs. Then, the gain vector $\{G\}$, in dB_m , was calculated for each frequency setting from

$$G_i = C_i - R_i. \quad (3.15)$$

The gain-frequency relation was obtained by applying a polynomial curve fit to the gain vector with respect to the frequency vector. By plotting this relation, we can obtain the cut-off frequency from the intersection between the curve and the -3dB line drawn from the low frequency gain.

The previous experiment was used to obtain the frequency response for the SLIK APD as mentioned above. The actual data and the curve fit of the frequency response are shown in Figure 3.14. The measured cutoff frequency was 12.75 MHz which is close to the manufacturer value (12 MHz).

3.8. Avalanche photodiode selection results

A group of APDs were characterized in order to choose a suitable detector for the new water vapor DIAL detection system. The characterization focused on two main APD structures, the reach through structure which is currently used in the LASE detection system and the newer SLIK structure. The SLIK structure APD showed better performance due to its lower noise, which will lead to an increase in the signal-to-noise ratio of the detection system by at least a factor of 10 over the current system.¹⁷ The EG&G SLIK APD package C30649E was selected because of the following advantages:

- Built-in, low noise, trans-impedance amplifier.
- Built-in thermoelectric cooler and thermistor for APD temperature control.

- The trans-impedance amplifier feedback resistance is cooled along with the detector, reducing the Johnson noise.

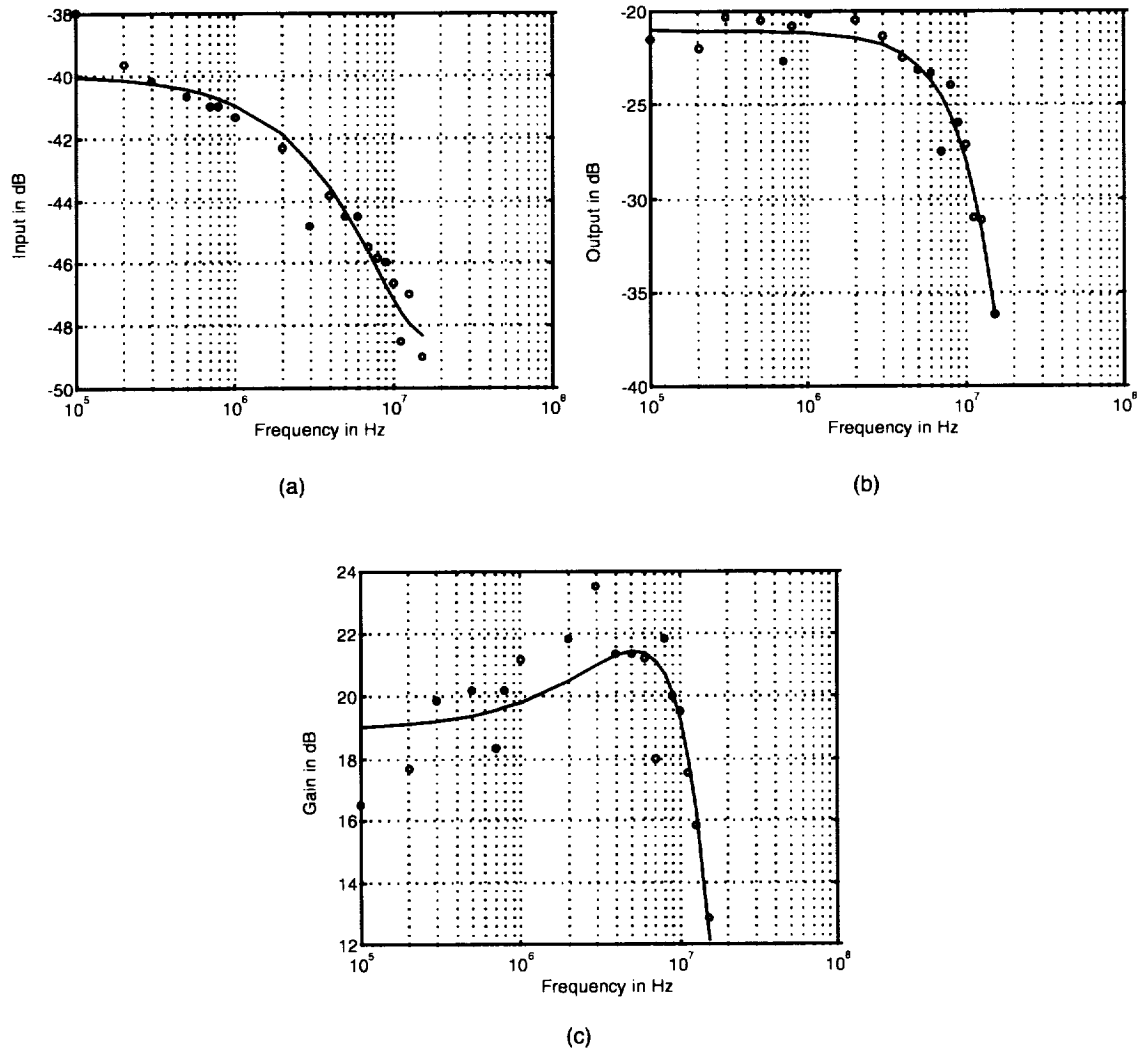


Figure 3.14 SLIK APD (a) input and (b) output variation with frequency and (c) frequency response obtained at 336V bias and 23 °C temperature.

A drawback in the selected APD arises from its small area (0.24 mm^2) compared to the LASE APD (1.7 mm^2) which might produce alignment difficulties. However, its lower noise strongly recommends it for the development of the new system.

CHAPTER IV

DETECTION SYSTEM DESIGN AND LABORATORY PERFORMANCE

The main goal of this research effort is to increase the signal-to-noise ratio (SNR) of the water vapor DIAL detection system by a significant factor compared to the LASE instrument.^{7,18} Also, it is required to design the system to a compact size suitable for mounting directly on the receiver telescope with output data compatible with a simple computer interface. In this chapter, the design details of the water vapor DIAL detection system will be discussed, as well as its laboratory performance.^{18-20,62}

4.1. Detection system design

A block diagram of the new water vapor DIAL detection system is shown in Figure 1.2. The APD detected light signal is applied to the analog circuit shown in the block diagram of Figure 4.1. The analog circuit is designed to control the operation of the APD package and to condition its output signal in preparation for the 14-bit digitizer.

The laser return signal is focused onto the 0.5-mm diameter APD sensitive area. The APD output signal is applied to the signal conditioning stage, which consists of three substages. In DIAL applications, the transmitted laser pulses might hit a large amount of water vapor or aerosol layer, such as clouds, resulting in high levels of backscattered light which could overload the system. These overload signals are a major problem since they saturate the detector and cause “hanging” of the digitizer, which leads to loss of some data words. The clipping circuit is used to protect the digitizer by clipping these overload

signals to a predefined level. For normal signals the clipping circuit acts as a voltage-follower amplifier. The APD overload is prevented using a current limiting resistor R as shown in Figure 4.1.⁶²

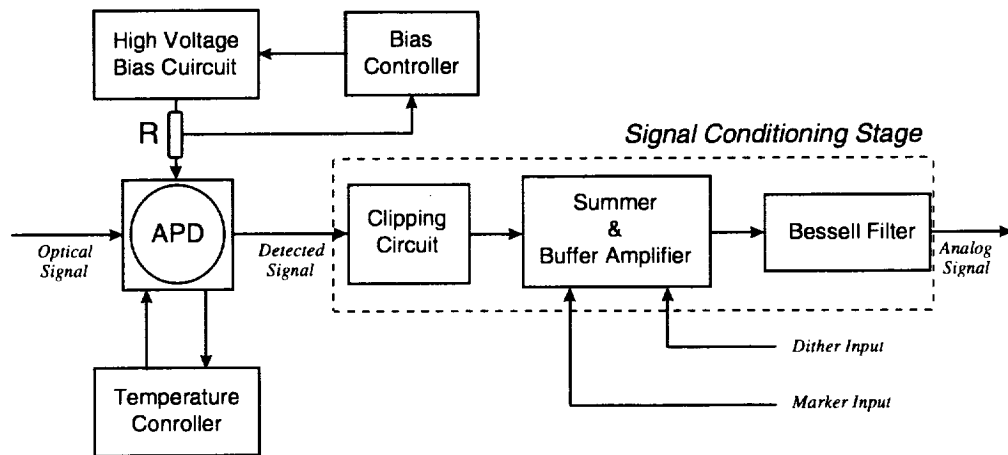


Figure 4.1 Block diagram of the analog circuit.

Following this stage is a summer and buffer amplifier, designed to provide an additional gain to the detected signal in order to achieve a 2-V maximum peak-to-peak value which is compatible with the digitizer maximum input range. Also, it adds a marker and dither signals to the detected signal. The marker signal is used to mark the beginning of the useful data, while the dither is used to add a low level sinusoidal signal for better digitization performance.^{18,62}

Finally, the signal is applied to a Bessel filter, with a 2.5-MHz cutoff frequency. This filter limits the system bandwidth in order to reduce the high frequency noise and restrict the signal frequency with respect to the digitizing frequency according to the Nyquist criterion.^{39,51}

Since the APD responsivity is a strong function of its voltage bias and temperature, two proportional integral (PI) controllers were used. The first is a voltage controller which can be adjusted manually to apply a constant bias to the APD. The second is a temperature controller with a fixed set point. This controller is used to cool the detector with respect to the ambient temperature.⁶⁸

The output, detected signal from the analog circuit is applied to the digital circuit. The digital circuit was designed mainly to operate as a waveform digitizer but also performs some simple data processing such as averaging DIAL lidar return signals (hardware averaging) and monitoring the detection system performance. Figure 4.2 shows a block diagram of the main components of the digital circuit. The 14-bit, 10-MHz analog-to-digital converter (ADC) is used to convert the analog lidar signal from the detector to a digital format. The dual-port RAM is used for temporary data storage and it also isolates the 10-MHz digitizer frequency from the 16-MHz microcontroller frequency.^{19-20,62}

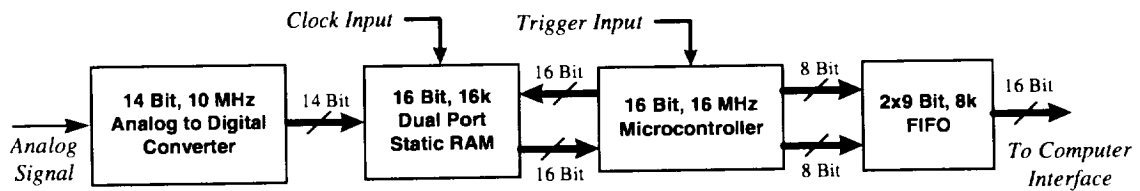


Figure 4.2 Block diagram of the digital circuit.

Approximately 400 μ s before the DIAL laser fires, a trigger pulse is generated and is used as a precursor that informs other systems that the laser is about to fire. This pulse is sensed by the microcontroller and acts to synchronize the detection system with the laser transmitter. A 10-Hz maximum laser firing frequency is assumed in this design, although a

higher repetition rate could be accommodated. Also, the microcontroller will be used for on-line data averaging and house keeping.²⁰

Finally, the first-in-first-out (FIFO) memory is used to output the final data to the recording system. Again, the FIFO separates the 16-MHz microcontroller operating frequency from the output data transfer rate which is dependent on the computer interface. The computer interface used with the detection system was a parallel input-output interface with a maximum of 20 MSPS data transfer rate. This interface is fully controllable by C++ software. The final data is stored in an output file which is accessible with any other software package.

4.1.1. Analog circuit

The signal conditioning stage is the most critical stage in the whole detection system since any noise contribution from this stage to the detected signal will directly affect the useful data. Figure 4.3 shows the circuit diagram of this stage. In the text the various components of the system are referred to by their letter designation. Details of circuit schematics are given in Appendix B, and the component listing is given in Appendix C. Operational amplifier U7 is a clipping op amp which operates as a voltage follower for the detected signal provided that the signal lies within the clipping limits. The upper clipping limit is set to 2.5 V using R24 and R25. This limit is chosen only for the op amp stability and has no influence on the output since the detected signal coming from the APD package is always negative with a maximum theoretical value of zero. The lower clipping limit is set by a -1.5 V reference voltage (Appendix B). Resistor R26 acts as the load resistance for the op amp as recommended by the manufacturer. The output of the

clipping op amp is then applied to U8 which is a gain and summer amplifier. Using this op amp the signal gain is set to 3 using R27 and R26. Another gain of 0.5 is applied to the signal using the R30 and R31 voltage divider, leading to a total end-to-end gain of 1.5 which was chosen so that the maximum APD output fit the maximum digitizer limit. This voltage divider is used for termination according to the maximum power transfer condition of Thevenin's theorem.⁵¹ The summation of the marker and the dither inputs to the detected signal is obtained using R28 and R29, respectively.^{40,52, 63,64}

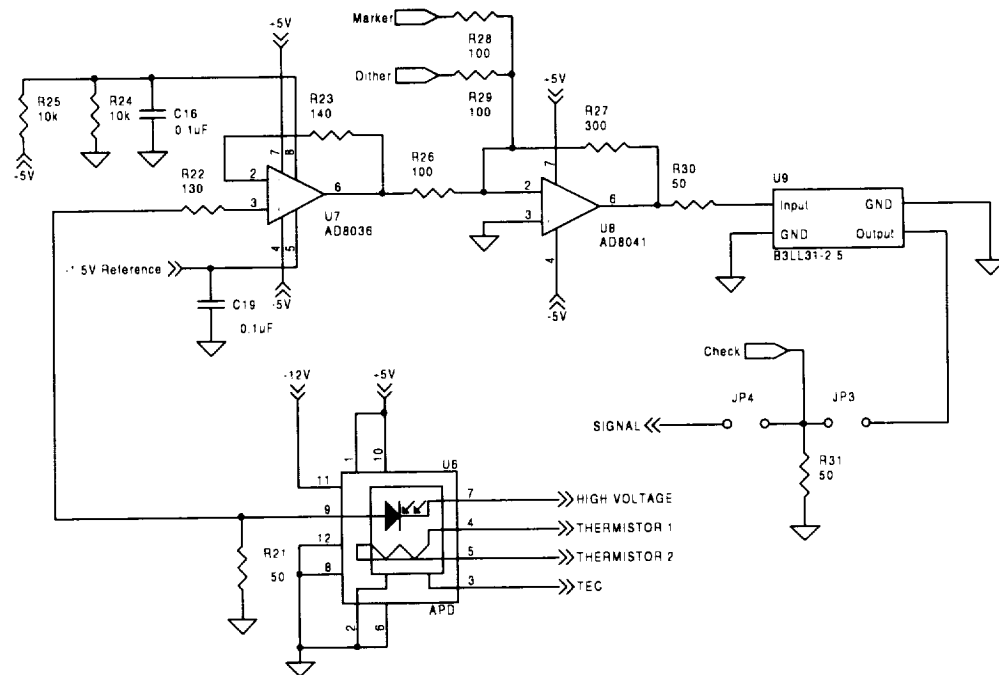


Figure 4.3 Circuit diagram of the signal conditioning stage.

The final output is then filtered using U9 which is a 3 pole, 2.5-MHz, low-pass Bessell filter. The Bessell filter was selected due to its excellent performance regarding the phase shift for real time data. In order to check the output signal from this stage, the

voltage across R31 can be accessed using an external connector. Also, this connector can be used to inject an external voltage to the digitizer according to the JP3 and JP4 jumper settings.⁶⁵

Figure 4.4 shows the circuit diagram of the APD high voltage bias controller. The APD voltage bias is supplied from U4, a high voltage module. The control of the high voltage was obtained using U3, a dual op amp chip, with one op amp acting as the proportional controller set to a gain of 4 using R3 and R4 and the other as the integral controller set to an RC time constant of 0.04 s using R5 and C5. Diode D1 is used to ensure positive control voltage to U4. Potentiometer R7 is used to set the APD high voltage between 292 and 365 V. The output high voltage is applied to a low-pass filter formed by R8 and C8 to eliminate any bias ripples. In addition, R8 limits the APD current for overload protection, and C9 supplies it with instantaneous in-rush current. A potential divider formed by R9 through R13 is used as the voltage feedback to the controller. Voltage monitoring is obtained after the proportional controller with a voltage reading V_{BM} related to the high voltage bias V_{BIAS} by the equation^{66,67,51}

$$V_{BM} = \frac{V_{BIAS}}{14.91} - 20. \quad (4.1)$$

The APD package was supplied from the manufacturer with a built in TEC cooler and a thermistor. The temperature status of the detector is sensed by the thermistor by placing it in an arm of a Wheatstone bridge formed by R15, R16, R17 and R18, as shown

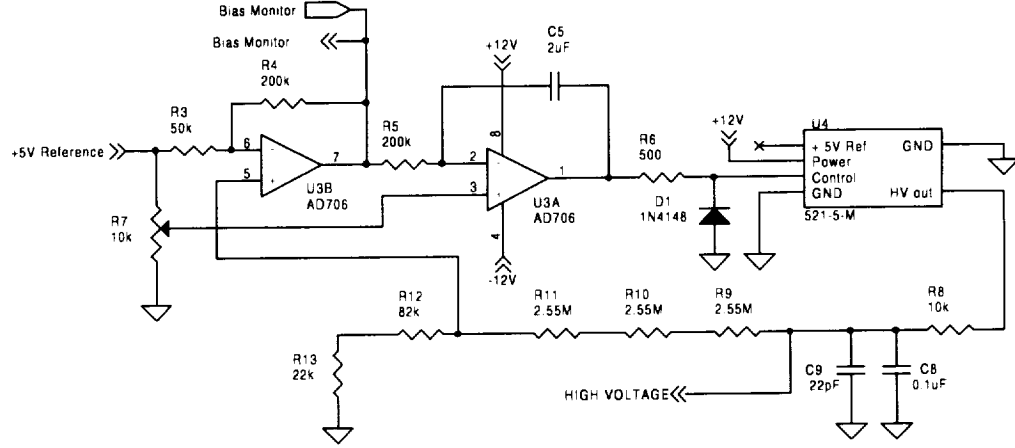


Figure 4.4 APD voltage bias controller circuit diagram.

in the circuit diagram of Figure 4.5. The value of R_{18} determines the balance condition of the bridge therefore setting the detector temperature. Since the thermistor resistance R_T is given by⁴⁹

$$R_T = 10^4 \cdot e^{\left[3940 \left(\frac{1}{T} - \frac{1}{298}\right)\right]}, \quad (4.2)$$

and the bridge balance condition is⁵¹

$$\frac{R_{15}}{R_{16}} = \frac{R_T}{R_{17} + R_{18}} = 1. \quad (4.3)$$

Therefore, the temperature setting, in Kelvin, will be given by

$$T = \left\{ \frac{\ln \left(\frac{R_{18} + 33 \times 10^3}{10^4} \right)}{3940} + \frac{1}{298} \right\}^{-1}. \quad (4.4)$$

Equation (4.4) indicates that the minimum temperature setting is selected by R_{17} ($33 \text{ k}\Omega$) and is equal to 0.3°C with R_{18} short-circuited. Temperatures lower than this value usually cause problems due to condensation of water vapor on the detector window. Zener diode

D2 is used to supply the bridge by its zener voltage V_Z equal to 5.1 V. The zener current limit is set by R14.⁵³

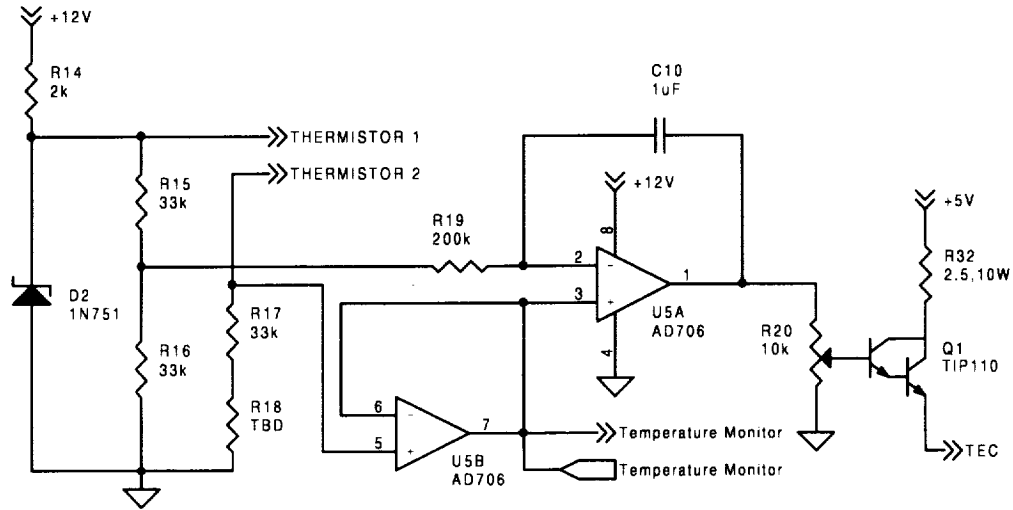


Figure 4.5 APD temperature controller circuit diagram.

The bridge balance is sensed by an instrumentation amplifier formed by the dual op amp U5,⁵² with one op amp acting as a voltage follower for the temperature monitor and the other acting as both the proportional integral controller with RC time constant of 0.02 s set by R19 and C10. The controller output is applied to a potentiometer R20 to set the TEC current by controlling the collector emitter current of the Darlington transistor Q1.⁶⁸ Resistor R32 is a 10 W resistor used to set the maximum TEC current to 2 A according to its manufacturer specification. The temperature monitor voltage reading V_{TM} will be given in terms of the zener voltage by⁵³

$$V_{TM} = \frac{R17 + R18}{R17 + R18 + R_T} V_Z. \quad (4.5)$$

After starting the circuit when the detector temperature reaches its steady state value the monitor voltage will be simply given by

$$V_{TM} = \frac{1}{2} V_z. \quad (4.6)$$

This voltage can be read directly using an output connector to indicate the temperature stability of the APD.⁵³

Referring to Figure 4.3, the conditioned analog signal “SIGNAL” will be applied to the digitizer, provided that both jumpers are shorted. A high input impedance instrument, such as an oscilloscope, can access this signal using the “CHECK” terminal.

4.1.2. Digital circuit

The conditioned analog signal was applied to a 14-bit, 10-MHz ADC, as shown in the block diagram of Figure 4.6. The input digitizer range was set to be from 0 to 2 V. Therefore, the maximum allowable output signal from the detector package is given by

$$2 \times \frac{\text{ADC Upper Limit}}{\text{Signal Conditioning Gain}} = 2 \times \frac{2}{-3} = -1.33 \text{ V} \quad (4.7)$$

while the clipping op amp U7 lower limit was set to -1.5 V . This was done to insure the linearity of the signal conditioning stage by avoiding the non-linear knee between the linear and clip regions in the op amp input-output characteristics.

A 10-MHz clock signal was externally applied to the ADC. Therefore, it continuously digitizes the analog signal during each clock cycle. The digitized data was buffered and stored in a certain memory location in a 16-bit, 16 k, dual-port RAM. The data storage location or address was set by a 13-bit counter formed by cascading three 4-bit binary counters and a JK flip flop. The counter and the RAM share the same 10-MHz

clock in order to synchronize them with the ADC. Connecting the most significant bit (MSB) of the left RAM address to the supply enables the counter only to access its upper half while the lower half of the RAM is kept for data averaging proposes. Thus, the maximum real time window for the digitized data can be obtained by

$$\text{Data Time Window} = \frac{\text{Storage Space}}{\text{Clock Frequency}} = \frac{16 \times 1024 / 2}{10 \times 10^6} = 819.2 \mu \text{ sec} \quad (4.8)$$

which is enough to record both the on and off line DIAL laser signal returns.

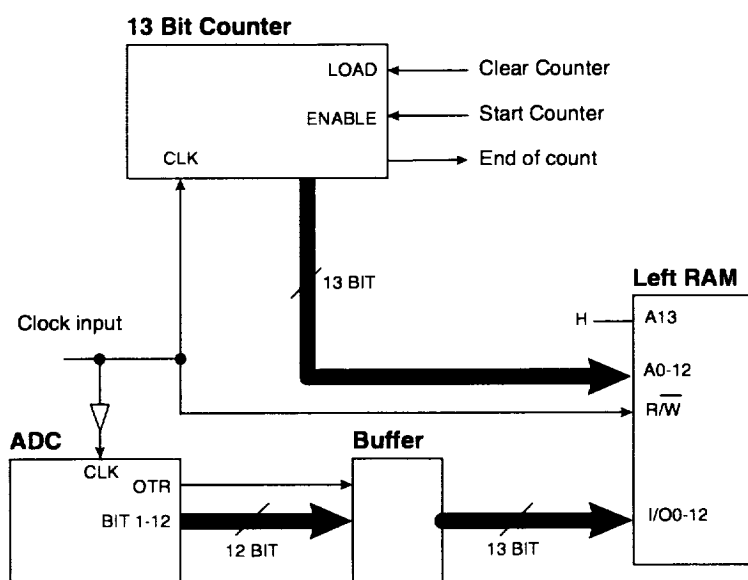


Figure 4.6 Block diagram of the data collect and store circuit.

The counter operation is controlled by the microcontroller. At the beginning of the circuit operation, the microcontroller sends a clear signal to the counter resetting its output to the left address 2000H equivalent to the right address C000H which is the first storage location in the RAM, as shown in Figure 4.7. The ADC output will be continuously stored in this location until the trigger signal is received.

3FFFH	ADC Output Data Storage	FFFFH
2000H		C000H
1FFFH	Data Averaging	BFFFH
0000H		8000H
	FIFO	7FFFH
		7000H
	Control Word	6FFFH
		6000H
	NOT USED	5FFFH
		4000H
	Internal Program Storage EPROM	3FFFH
		2080H
	NOT USED	
	Register File	00FFH
		0000H

Figure 4.7 System memory map.

When the microcontroller senses the trigger signal, it sends a start count or “counter enable” signal to the counter causing it to address successive memory locations in the RAM in order to store the useful data. After scanning half the memory, when the counter reaches its maximum count of 1FFFH, which is equivalent to memory in the address of 3FFFH, an “end-of-count” signal will be sent back to the microcontroller indicating the end of the time window record. Therefore, the useful data will be available to the microcontroller in the address range from C000H to FFFFH, as shown in the memory map in Figure 4.7.⁶⁹⁻⁷³

The 16-MHz, 87C196KB-16 microcontroller is shown in the block diagram of Figure 4.8. The memory map of the microcontroller and the RAM is shown in Figure 4.7. The microcontroller address and data are shared on the same bus using address latching. The microcontroller address is decoded to access the right address of the RAM, a FIFO and a dip switch. The memory section, starting with the nibble 7, is reserved to access the FIFO as will be discussed in the output stage. While the memory section, starting with the nibble 6, was reserved for the control word, set by on-board 8-bit dip switches S1, the “not used” address range from 4000H to 5FFFH can be used for system upgrades to the 87C196KC microcontroller.⁷⁴⁻⁷⁸

After storing the ADC data in the RAM, the counter sends an “end-of-count” signal to the microcontroller. The microcontroller starts to transfer and add the data from the upper half of the RAM to its lower half for averaging. At the end of each averaging cycle, the data will be transferred to the FIFO which is waiting to transfer data to the reading device. The dip-switch output is buffered and was used to give the microcontroller a control word to indicate the averaging times required with a maximum of 4 averages. Also, it indicates the record length which could be 1, 2, 4 or 8 k words corresponding to 102.4, 204.8, 409.6 or 819.2 μ s, respectively. (In case of record length less than 8k, the ADC data will still be stored in 8k and the first 4k, 2k or 1k will be considered and the rest of the data will be neglected.)⁶²

One advantage of the selected microcontroller is its built-in 8 channel 10-bit ADC, two channels of which are reserved for the detector bias voltage and temperature monitor readings.⁷⁵⁻⁷⁶

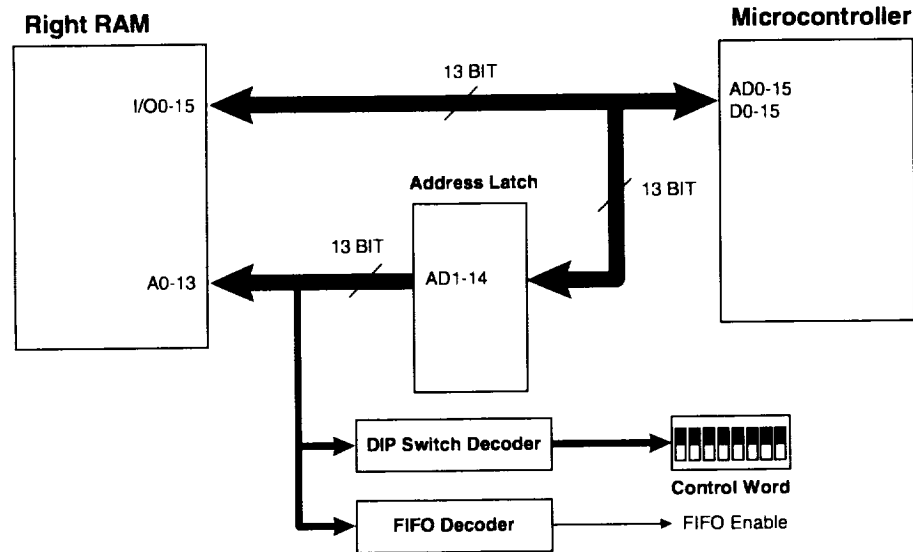


Figure 4.8 Microcontroller connection block diagram.

Figure 4.9 shows the block diagram of the output stage of the digital circuit. The FIFO is formed by a parallel connection of two 8-k, 9-bit FIFO's memories to form an 18-bit word to handle the 16-bit data.⁷⁷ The output data was buffered and applied to four 4-channel, TTL-compatible optical isolators. These isolators are used to isolate the circuit and the reading device grounds.⁷⁹ Finally, the data was read using a SCXI connector. The FIFO write and reset operations are controlled by the microcontroller, while the FIFO read is controlled by the reading device.⁸⁰ In order to check the correct sequence of data handling, the empty flags of both FIFOs are read by the microcontroller. Any unequal state of these flags indicates a FIFO failure or data crash.

After the microcontroller sends the complete data set to the FIFO, it sends a "FIFO ready" signal to the reading device to synchronize it with the system. Both the FIFO ready and FIFO read signals are also optically isolated by U37 which are opto-couplers with dual separate channels, once again to separate the grounds to minimize noise pick up.

Finally, the microcontroller controls the FIFO reset signal in order to reset the FIFO before the first writing operation.⁶²

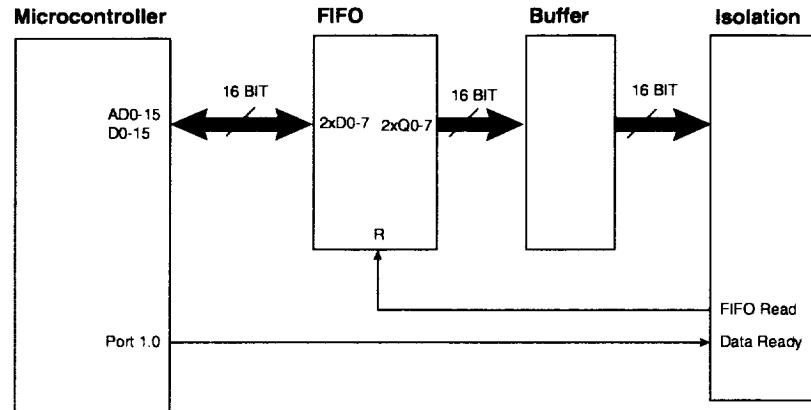


Figure 4.9 Block diagram of the output stage.

4.2. Detection system settings

This detection system was built on one 312-gm, 15x9 cm² printed circuit board using surface-mount technology. This was very challenging because of the sensitivity of the different elements to the board layout, since analog signals were subjected to different noise pick-up sources from the high switching frequency digital signals. The board layout was carefully designed to separate the analog and digital circuits on the two board sides with ground isolation between them. The whole detection system is optically isolated from any external instrument such as the clock generator, trigger input and computer. The only electrical connection between the detection system and any external device will be through the power supplies that had proper filtering and isolating the power grounds from the circuit grounds. The calculated power consumption of the card is 21.1 W (see Appendix C).^{18-20,62}

4.2.1. Microcontroller program

Figure 4.10 shows the flowchart of the microcontroller program. After switching on the power supplies, the start sequence begins by resetting the microcontroller chip and configuring its port, as shown in Figure 4.11. Port 1 is used for the counter and FIFO control and monitoring, while port 2 is used for sensing the trigger input and serial communication if used.⁷⁴

The microcontroller then reads the control word from the dip switch for averaging and record length settings, as shown in Figure 4.12. Then, it starts an infinite loop by clearing the counter in order to address the first data storage location in the RAM (2000H as shown in Figure 4.7). The microcontroller then enters a waiting loop for the trigger input. This trigger comes from the lidar transmitting system. If the trigger signal is sensed, the microcontroller starts the counter in order to store the output digitized data from the ADC. During this time, the microcontroller waits for the “end-of-count” signal from the counter.

If the microcontroller sensed the end of count signal, indicating the storage of the useful data, it starts transferring the data. The amount of the transferred data is 1, 2, 4 or 8 k words depending on the record length setting. If averaging was not used, the data will be transferred directly to the FIFO, and the data ready signal will be transmitted to the reading device. The sequence will be repeated in the next cycle. If averaging was used, the data will be transferred to the averaging memory locations as indicated in Figure 4.7; then, the cycle will be repeated to acquire additional data to be added to the previous data. After completing the number of averages, the final averaged data will be sent to the FIFO, and a ready signal will be transmitted to the reading device and the sequence repeated.

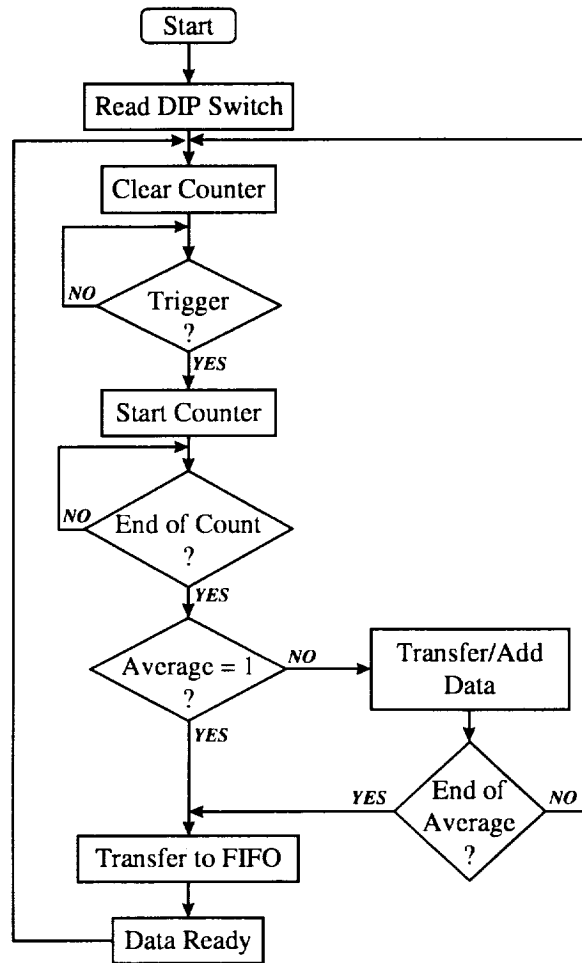


Figure 4.10 Flowchart of the microcontroller program.

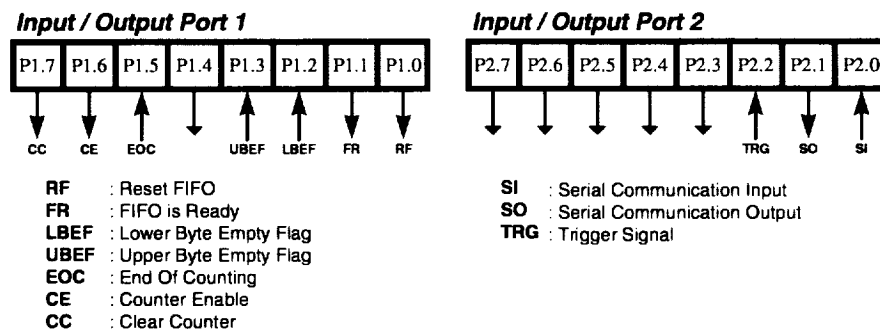


Figure 4.11 Microcontroller ports 1 and 2 configuration.

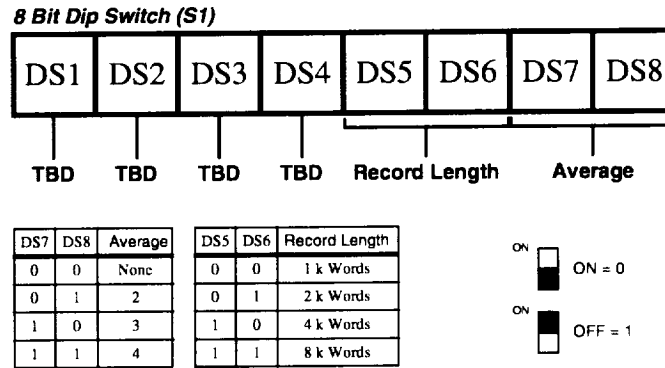


Figure 4.12 Dip switch configuration.

4.2.2. Data acquisition card

The final data stored in the FIFO is transferred to a personal computer using the PCI-DIO-32HS parallel input-output data acquisition card manufactured by National Instruments, Inc.,⁸⁰ The PCI-DIO-32HS is the state-of-the-art input-output data acquisition card which can be software configured using C++ language and can acquire data with up to a 20-MHz data transfer rate.⁸¹ The flowchart of the card program is shown in Figure 4.13 while the card connection to detection system is shown in Figure 4.14.

The card waits for the microcontroller data ready signal which is sensed by an acknowledge pin (ACK). If this signal is set, the card will start a pattern of data request signals (REQ) which will be used to read the FIFO using two parallel ports. This data set will be stored in a vector. Successive data sets will be added to this vector according to the number of the software averaging setting. The final averaged data is stored in an output file representing the DIAL detected signal.

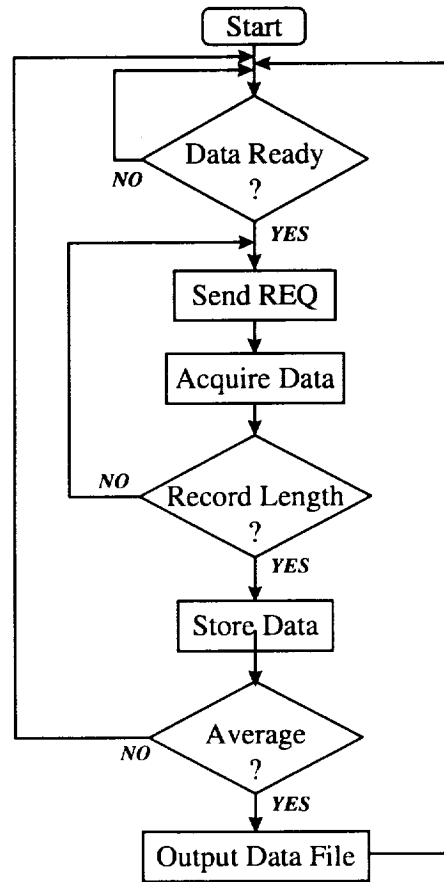


Figure 4.13 Flowchart of the PCI-DIO-32HS data acquisition card.

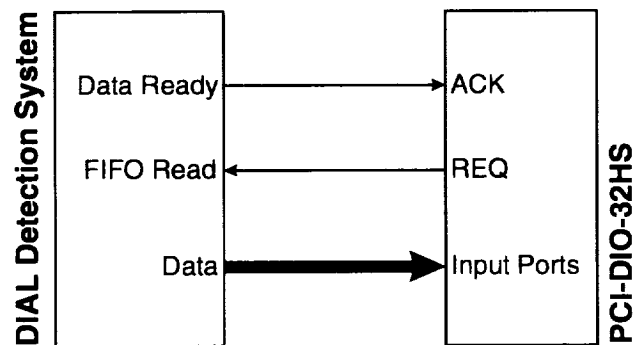


Figure 4.14 PCI-DIO-32HS data acquisition card connection to the detection system.

The whole system operation is summarized in the data flow diagram of Figure 4.15. The limitations of the averaging time T_A , transfer to FIFO time, T_F , and the external transfer time, T_E , are given in table 4.1.

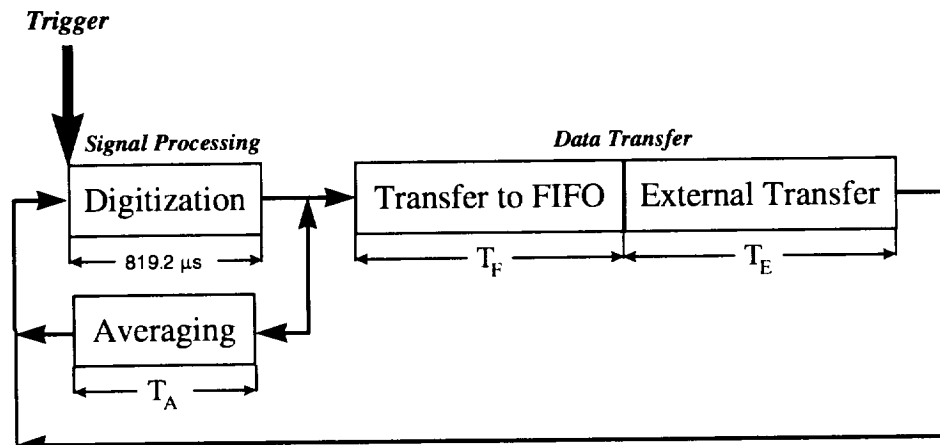


Figure 4.15 Detection system data flow diagram.

Table 4.1 Timing intervals for different record lengths.

Record Length		T_A Ms	T_F ms	T_E ms	Laser Frequency Hz (maximum)
k word	μ s				
1 k	102.4	10.3	11	0.6	90.1
2 k	204.8	20.5	22	1.2	45
4 k	409.6	41	44	2.5	22.5
8 k	819.2	82	88	4.9	11.3

4.3. Laboratory performance testing

The laboratory performance testing was performed on the individual circuits and for the whole system. The setup of the detection system performance testing is shown in Figure 4.16. The DIAL return signal was simulated using a 788-nm wavelength laser diode. A diffuser and neutral density filter (NDF) with variable settings were used to

condition the optical signal in terms of uniformity and intensity. The check point was used to either observe the analog circuit output or to inject an external signal to the digital circuit.

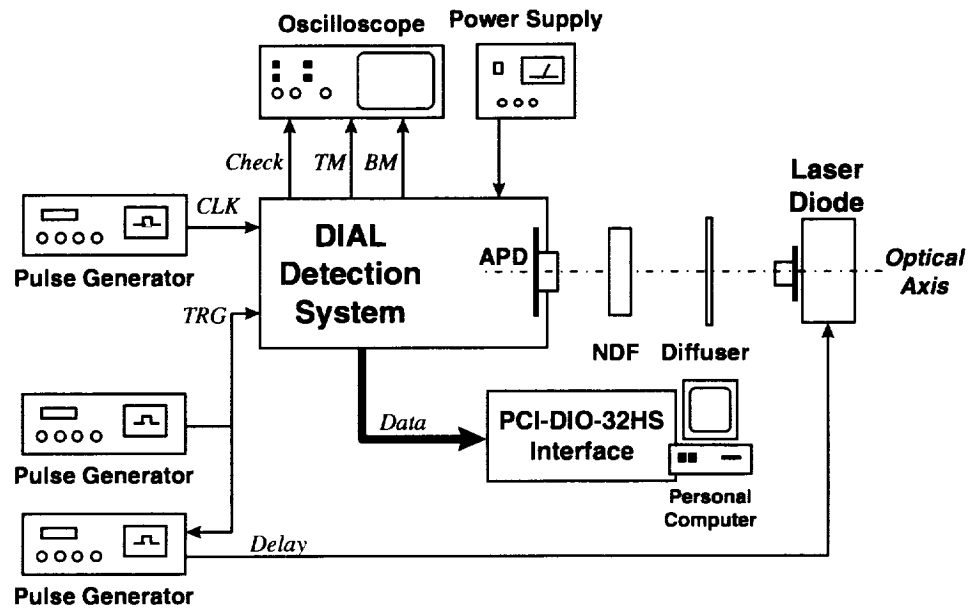


Figure 4.16 Experimental setup for detection system laboratory performance testing.

4.3.1. Temperature and bias voltage controllers performance

The APD temperature was set to $0.3\text{ }^{\circ}\text{C}$ by setting R18 equal to zero. For an initial APD temperature of $23.6\text{ }^{\circ}\text{C}$, Figure 4.17 shows the transient response of the APD temperature monitor voltage V_{TM} , the thermistor resistance, the APD temperature and the TEC current. The rise time is approximately 5 s, and the 5-percent settling time is approximately 50 s with about $2\text{ }^{\circ}\text{C}$ of overshoot. The steady-state temperature was $0.3 \pm 0.3\text{ }^{\circ}\text{C}$. The temperature measurement is obtained by converting the temperature monitor voltage to a thermistor resistance according to equation (4.5), and then this is

further converted into temperature according to equation (4.4). From Figure 4.17a and c, it is interesting to note a linear relationship between the APD temperature, T , and the temperature monitor voltage, V_{TM} over a 30 °C operating range which is approximated by

$$T \approx 17.2 \cdot V_{TM} - 43.6. \quad (4.9)$$

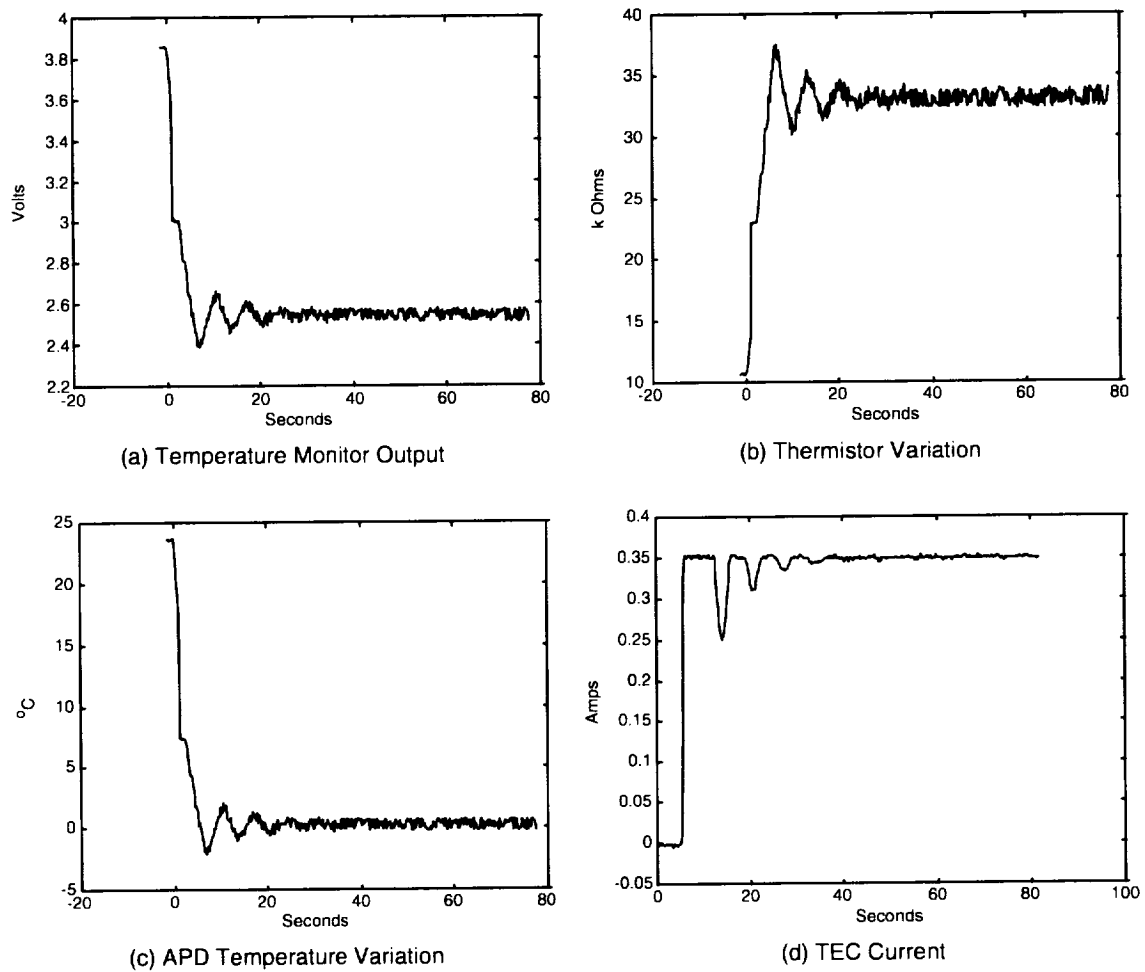


Figure 4.17 APD temperature controller response (a) temperature monitor, (b) thermistor resistance variation, (c) temperature variation and (d) TEC current.

Figure 4.17d shows a steady-state TEC current of approximately 0.35 A which corresponds to a steady state TEC input power of 174 mW. For successful temperature

controller operation, the maximum ambient temperature is 27 °C. Since the controller was designed to cool the detector, the minimum ambient temperature is theoretically equal to the controller temperature setting.⁵³

The APD voltage bias controller was set to produce a bias voltage of 336 V. This value was chosen to avoid breakdown at low operating temperature. Figure 4.18 shows the turn-on transients APD voltage bias monitor and its bias voltage obtained using equation (4.1). The measured steady state bias is 336.6 ± 0.6 V with a settling time of 1.3 s and rise time of 75 ms with an undershoot of 297.4 V.

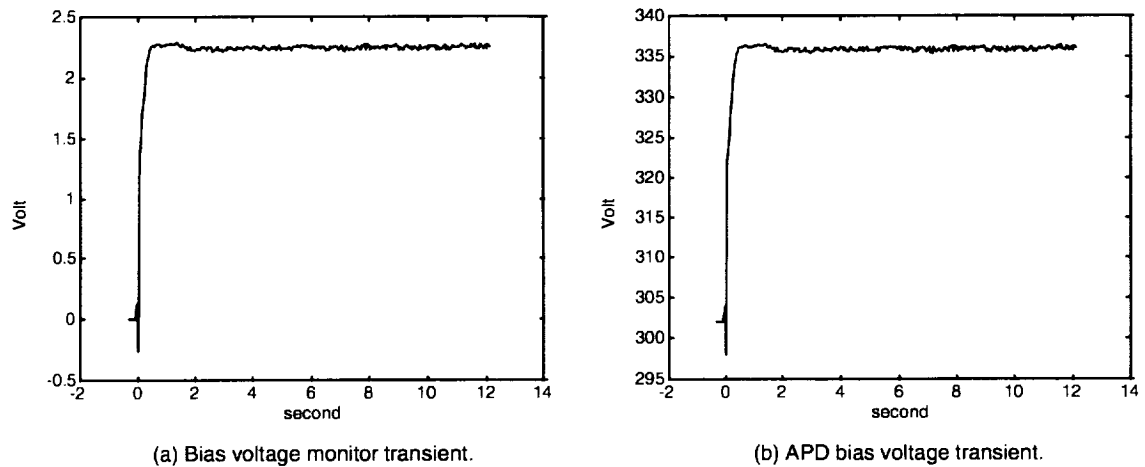


Figure 4.18 APD voltage bias monitor and bias voltage transients.

4.3.2. Signal conditioning circuit performance

In order to evaluate the signal conditioning stage gain, the APD output was replaced by a calibrated voltage input, and the output was then measured. Figure 4.19 shows the normalized gain versus the input voltage. The mean gain along the input range of the signal conditioning stage was measured to be 1.52 with 0.2 % standard deviation. The

clipping action of this stage is clear and starts at an input signal of 1.33 V corresponding to an output of 1.99 V which is compatible with the ADC. The frequency response of the signal conditioning stage is shown in Figure 4.20. This was measured by applying a known sinusoidal input and measuring the change in the amplitude and phase due to the change in the frequency. The input frequency was varied from 1 kHz to 3 MHz. The cutoff frequency at -3 dB is 2.4 MHz which is compatible with the digitization frequency of 10 MHz.⁸²

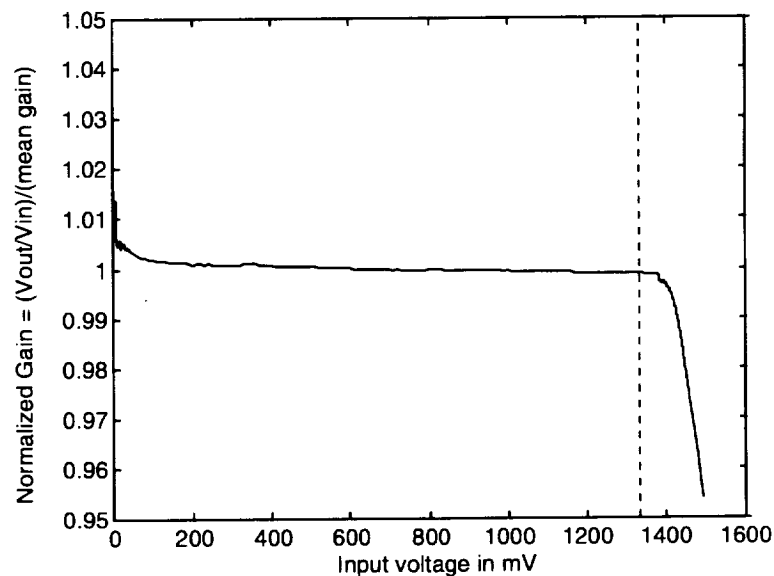


Figure 4.19 Signal conditioning stage normalized gain versus input voltage.

Figure 4.21 shows the APD and the signal conditioning stage noise spectrum obtained with no input (dark conditions) using a spectrum analyzer with 400 averages. This measurement suggested the use of batteries instead of power supplies to eliminate the power frequency harmonics noise pickup shown in the figure. The battery operation

spectrum shows the $1/f$ noise with a knee at 3 kHz. Pickup noise at the fundamental power frequency is clear from the figure and can be eliminated by proper shielding in the final packaging. The average integrated noise was found to be $150 \text{ nV/Hz}^{1/2}$ in the operating frequency range which indicates that the APD noise contribution is the dominant source. Considering the 2.5 MHz system bandwidth and the APD responsivity, this corresponds to a minimum detectable signal level of $1.5 \times 10^{-5} \text{ W/m}^2$.

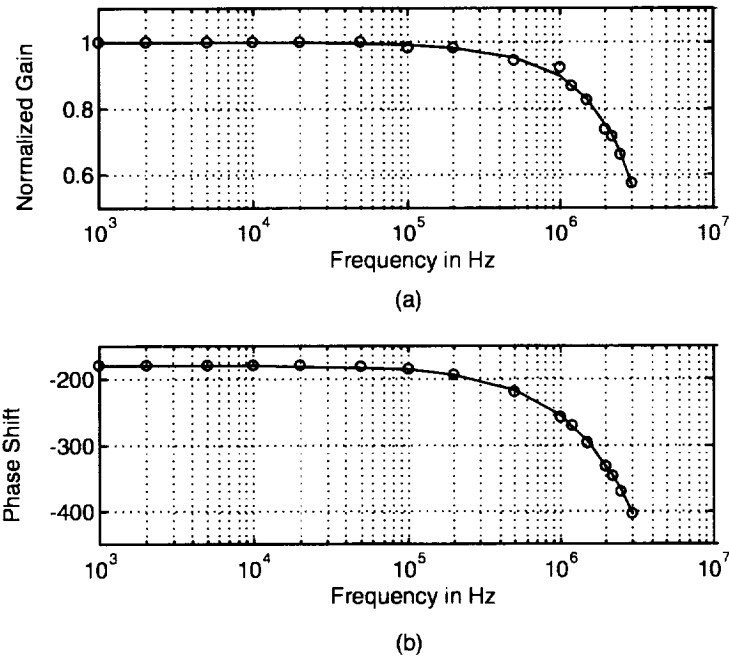


Figure 4.20 Signal conditioning stage frequency response for the (a) gain and (b) phase shift.

4.3.3. Digitizer performance

Several operational tests were performed to check the operation of the digital circuit. These tests included the following:

- The microcontroller ability to access the dip-switch, RAM and FIFO.

- The counter ability to address the RAM.
- The interface card ability to read the FIFO.

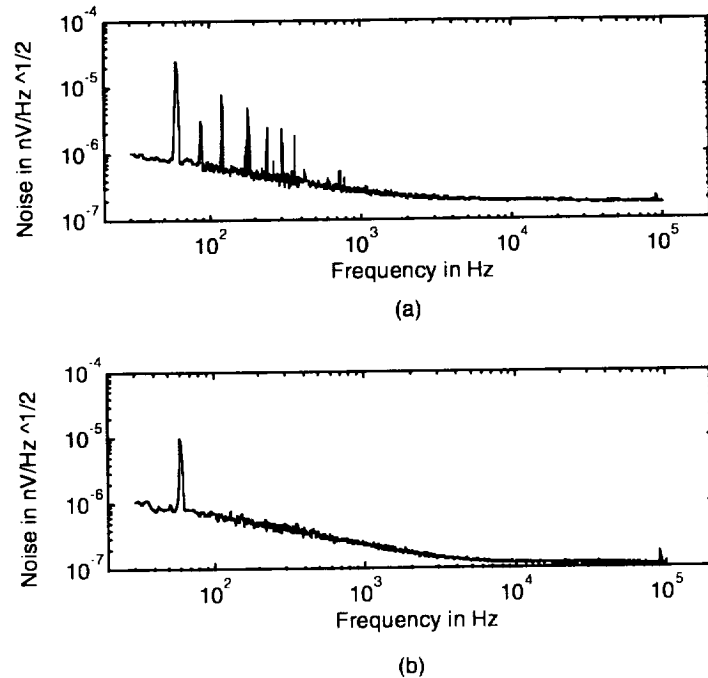


Figure 4.21 APD and signal conditioning stage low frequency noise spectrum using (a) power supplies and (b) batteries.

In order to test the performance of the whole digitizer circuit, a histogram test was applied to check for any missing codes. In the histogram test, a sine-wave is applied to the digitizer input with a non-coherent frequency with the sampling rate of the digitizer. The amplitudes of this signal must be selected slightly out of the digitizer range to insure the coverage of all possible codes. Several samples of the input signal were taken and the occurrence of every possible ADC output is counted.⁸³ The selected sine-wave for this test had a 4.95-kHz frequency with 2.03 V peak-to-peak and 997.3 mV offset levels, shown in Figure 4.22a. The over and under range data shown in the figure insures that the input signal covers the whole digitizer range; therefore, all codes must be present in the

histogram plot. The histogram plot is shown in Figure 4.22b for 500 cycles. The height of each point is proportional to the total number of times that code occurred. Missing codes would appear at zero height. Figure 4.22b indicates no missing codes.

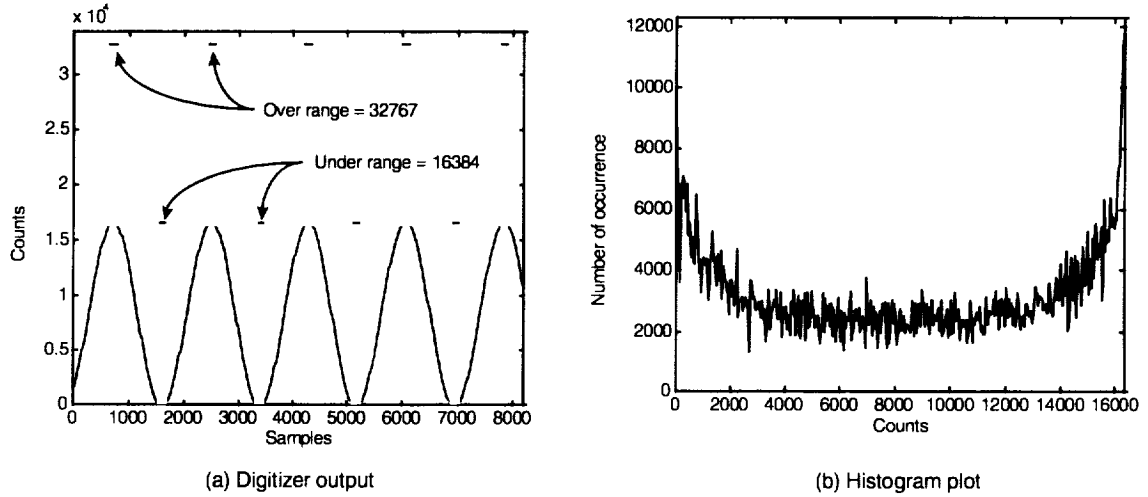


Figure 4.22 (a) Input sine-wave signal to the digitizer and (b) the histogram plot which indicates no missing codes.

4.3.4. Overall system performance

Testing of the whole detection system was performed in order to characterize its gain and SNR. The input optical signal was obtained from a 788-nm laser diode corresponding to an APD responsivity of 117.5 A/W at a bias voltage of 336 V and 0.3 °C operating temperature. The laser diode current and temperature were kept constant using a driver circuit and a temperature controller to stabilize its operation. Single-shot pulsed signals with 100 μ s duration and variable intensities were obtained to measure the gain and SNR. Neutral density filters were used for changing the laser input intensity. Using the setup shown in Figure 4.16, the experimental intensity level was varied between a

minimum of $8.5 \times 10^{-5} \text{ W/m}^2$ to a maximum of $8.42 \times 10^{-2} \text{ W/m}^2$ to insure the linearity of the system. Figure 4.23a shows the system output in counts versus the input light intensity which indicates a linear relation with a constant total gain of $183,960 \text{ counts}/(\text{W/m}^2)$ over the characterized range. Figure 4.23b shows the SNR versus the input laser intensity. The SNR was obtained by squaring the ratio of the detected pulse mean value to its standard deviation. A minimum SNR of 2.7 was obtained in this experiment.

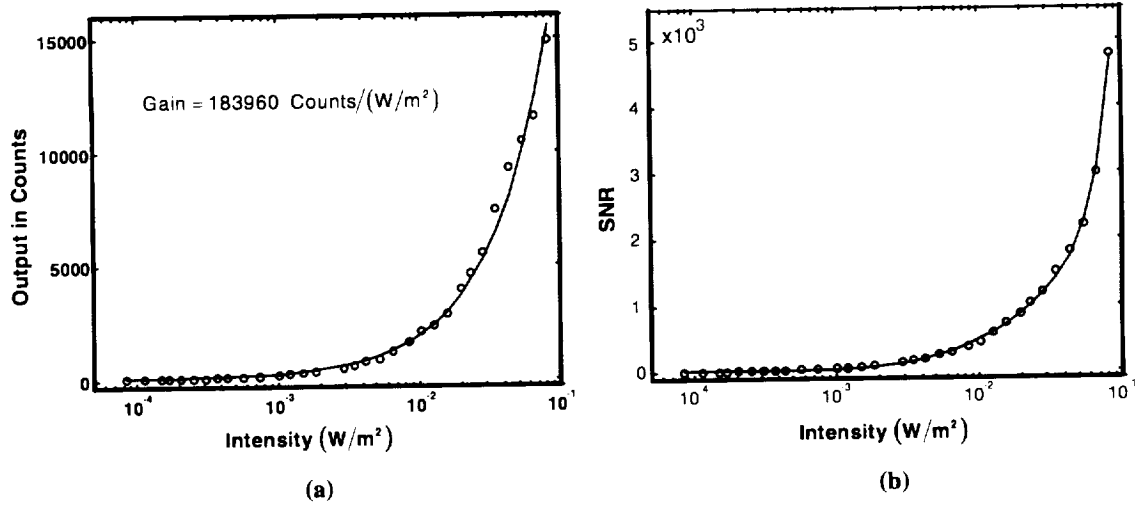


Figure 4.23 (a) System output in counts versus input light intensity obtained with no averaging at 788 nm and (b) the corresponding signal-to-noise ratio.

In order to determine the minimum measurement capabilities of the system, the lidar return signals were simulated in order to obtain the minimum water vapor detection capabilities of the system. To convert the lidar detected signals into a water vapor number density profile the DIAL equation is used which is given by

$$N(R) = \frac{1}{2 \cdot \Delta R \cdot \Delta \sigma} \ln \left[\frac{P_{\text{OFF}}(R_2) \cdot P_{\text{ON}}(R_1)}{P_{\text{OFF}}(R_1) \cdot P_{\text{ON}}(R_2)} \right], \quad (4.10)$$

where N is the water vapor number density, ΔR is the range cell, $\Delta\sigma$ is the differential absorption cross section and P_{ON} and P_{OFF} are the DIAL on-line and off-line return signals, respectively. Ideally, if the on-line and off-line return signals are identical, the water vapor number density should be zero, as indicated in the above equation.

Applying this concept to the detection system, one can estimate the minimum detectable water vapor number density, which is determined by the system noise as shown in Figure 4.24. Therefore, the laser diode was configured to give two identical exponential decaying pulses with a 30 μ s time constant as shown in Figure 4.24a. The first pulse was to simulate the on-line return while the second pulse was to simulate the off-line pulse.

Figures 4.24b and c show the single shot water vapor number density obtained for the lower and upper troposphere, respectively, with no averaging. The DIAL calculations were performed using a range cell of 300 m and water vapor differential absorption cross section of $10 \times 10^{-24} \text{ cm}^2$ and $150 \times 10^{-24} \text{ cm}^2$ for the lower and upper troposphere, respectively, as specified by the LASE detection system. The DIAL calculation indicated a minimum detectable water vapor number density of $6.7 \times 10^{16} \text{ cm}^{-3}$ for the lower troposphere and $4.5 \times 10^{15} \text{ cm}^{-3}$ for the upper troposphere. These water vapor number densities are comparable to those for the LASE instrument which are $5 \times 10^{17} \text{ cm}^{-3}$ and $5 \times 10^{14} \text{ cm}^{-3}$ for lower and upper troposphere, respectively, with 1000 shot averages. This indicates the improved water vapor detection capabilities of the new system by a factor of 9 for the upper troposphere measurements.²⁰

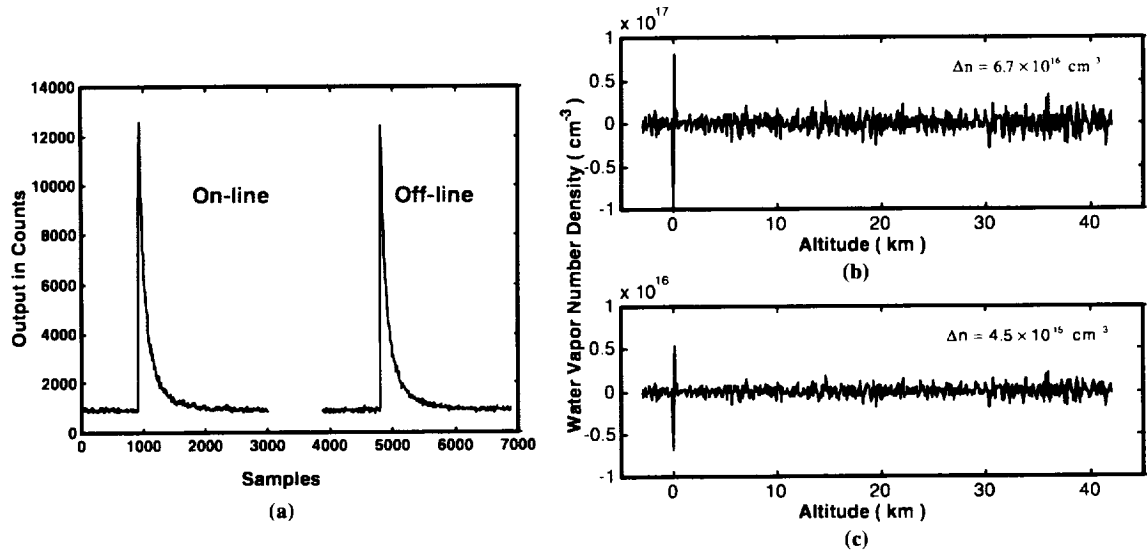


Figure 4.24 (a) Simulated lidar return signals. (b) Water vapor number density noise floor for the lower troposphere and (c) for the upper troposphere.

CHAPTER V

THE LIDAR THEORY

In this chapter, the derivation of the backscattering lidar equation will be discussed. The modification of the equation to include the absorption and the geometry of the receiver system also will be given. Based on the backscattering-absorption lidar equation, the differential absorption lidar (DIAL) equation will be derived. Finally, application of the backscattering lidar equation for measuring aerosols will be discussed as well as the application of the DIAL equation for water vapor measurement.

5.1. The Lidar Equation

The scattering form of the lidar equation defines the received atmospheric backscattered laser power in terms of laser pulses propagated into the atmosphere and collected by the receiver that is located near the laser transmitter. The variation in the received intensity is used to determine the density profile of atmospheric molecules and aerosols as a function of the altitude.

Under the assumption of a pulsed lidar, the variation in the signal power $\Delta P(\lambda, R)$ received by the detection system in the wavelength range $(\lambda, \lambda + \Delta\lambda)$ from the range element $(R, R + \Delta R)$ is given by⁵

$$\Delta P(\lambda, R) = \int J(\lambda, R, r) \cdot \Delta\lambda \cdot \Delta R \cdot p(\lambda, R, r) dA(R, r), \quad (5.1)$$

where $J(\lambda, R, r)$ is the laser-induced spectral radiance at wavelength λ , at position r in the range R per unit range interval, $p(\lambda, R, r)$ is the probability that radiation of wavelength λ

scattered from position r at range R will be detected and $dA(R,r)$ is the element of the target area at position r and range R .

The target spectral radiance $J(\lambda, R, r)$ depends on the nature of the interaction between the laser radiation and the target medium. For elastic or inelastic scattering medium, $J(\lambda, R, r)$ will be given by⁵

$$J(\lambda, R, r) = \beta(\lambda_L, \lambda, R, r) \cdot I(R, r), \quad (5.2)$$

where $I(R, r)$ is the laser intensity at position r and range R and $\beta(\lambda_L, \lambda, R, r)$ is the volume backscattering coefficient given by⁵

$$\beta(\lambda_L, \lambda, R, r) = \sum_i N_i(R, r) \cdot \left\{ \frac{d\sigma(\lambda_L)}{d\Omega} \right\}_i \cdot \mathfrak{I}_i(\lambda), \quad (5.3)$$

where $N_i(R, r)$ is the number density of scatterer species i , $\{d\sigma(\lambda_L)/d\Omega\}$ is the differential scattering cross section under irradiation with laser radiation at wavelength λ_L and $\mathfrak{I}_i(\lambda)$ is the fraction of the scattered radiation that falls into the wavelength interval $(\lambda, \lambda + \Delta\lambda)$.

The probability $p(\lambda, R, r)$ will be affected by several factors which are included in the equation⁵

$$p(\lambda, R, r) = \frac{A_o}{R^2} \cdot T(\lambda, R) \cdot \xi(\lambda) \cdot \xi(R, r), \quad (5.4)$$

where A_o/R^2 is the acceptance solid angle of the receiver optics with A_o being the area of the telescope mirror, $T(\lambda, R)$ is the atmospheric transmission factor at wavelength λ over the range R , $\xi(\lambda)$ is the spectral transmission factor of the receiver which includes the effect of any spectral selecting elements such as filters and $\xi(R, r)$ is the overlap factor or the geometrical form factor defined as the probability of radiation from position r at the range R being detected based on geometrical considerations. In this section, $\xi(R, r)$ will be

assumed dependent only on the overlap area between the transmitted laser beam and the receiver telescope field of view. In sections 5.1.1 and 5.1.2, this term will be discussed in detail in terms of the receiver optics.

To evaluate the total power of the return signal collected by the receiver at the instance t (where $t = 2R/c$ represents the time interval between the propagation of the laser pulse to the range R and the returned radiation to reach the receiver), equation (5.1) must be integrated with respect to both the received wavelength and the range R . The range integral is to account for the radiation reaching the receiver from any position along the path of the laser pulse from which scattering occurs. The wavelength integral is to consider the total receiver spectral window $\Delta\lambda_o$ centered at λ , which is usually defined by the optical filter. Therefore, equation (5.1) can be expressed in the form⁵

$$P(\lambda, t) = \int_0^{R=ct/2} dR \int_{\Delta\lambda_o} d\lambda \int J(\lambda, R, r) \cdot p(\lambda, R, r) \cdot dA(R, r). \quad (5.5)$$

Substituting equations (5.2) and (5.4) into equation (5.5) yields:

$$P(\lambda, t) = A_o \int_0^{R=ct/2} \frac{dR}{R^2} \int_{\Delta\lambda_o} \xi(\lambda) \cdot d\lambda \int \beta(\lambda_L, \lambda, R, r) \cdot T(\lambda, R) \cdot \xi(R, r) \cdot I(R, r) \cdot dA(R, r) \quad (5.6)$$

The assumption that the observed radiation from the scattering medium is as narrow as that of the laser radiation and that both are much smaller than the receiver spectral window $\Delta\lambda_o$, suggest that both $\mathfrak{I}_i(\lambda)$ and β can be treated as delta functions. Furthermore, assuming that the scattering medium is homogenous over the overlap between the field of view and the laser beam results in equation (5.6) being written in the form:

$$P(\lambda, t) = A_o \xi(\lambda) \int_0^{R=ct/2} \beta(\lambda_L, \lambda, R) \cdot T(\lambda, R) \cdot \frac{dR}{R^2} \int \xi(R, r) \cdot I(R, r) \cdot dA(R, r). \quad (5.7)$$

As mentioned above, the assumption that the probability $\xi(R, r)$ is unity where the field of view of the receiver overlaps with the laser beam and zero elsewhere, and that the lateral distribution of the laser pulse is uniform over an area $A_L(R)$ at the range R , results in

$$\int \xi(R, r) \cdot I(R, r) \cdot dA(R, r) = \xi(R) \cdot I(R) \cdot A_L(R). \quad (5.8)$$

Equation (5.7) can be written as

$$P(\lambda, t) = A_o \xi(\lambda) \int_0^{R=ct/2} \beta(\lambda_L, \lambda, R) \cdot T(\lambda, R) \cdot \xi(R) \cdot I(R) \cdot A_L(R) \frac{dR}{R^2}. \quad (5.9)$$

For simplicity, assume that the temporal shape of the laser pulse is a rectangle of the duration τ_L . Then, the limits of the range integration of equation (5.9) are $c(t-\tau_L)/2$ to $ct/2$. Furthermore, the range of interest is much larger than the pulse duration. Thus, the range dependent parameters can be treated as constants over the small interval of the range integration. Then, the total received power can be expressed by

$$P(\lambda, t) = A_o \xi(\lambda) \cdot \beta(\lambda_L, \lambda, R) \cdot T(\lambda, R) \cdot \xi(R) \cdot I(R) \cdot A_L(R) \frac{c\tau_L/2}{R^2}. \quad (5.10)$$

For a rectangular laser pulse of duration τ_L , the intensity is given by

$$I(R) = \frac{E_L T(\lambda_L, R)}{\tau_L A_L(R)}, \quad (5.11)$$

where E_L is the output energy of the laser pulse and $T(\lambda_L, R)$ is the atmospheric transmission factor at the laser wavelength to range R . From the Beer-Lambert law, the transmission factors in equations (5.10) and (5.11) are given by

$$T(\lambda_L, R) = \exp\left(-\int_0^R \kappa(\lambda_L, R) dR\right) \quad (5.12)$$

and

$$T(\lambda, R) = \exp\left(-\int_0^R \kappa(\lambda, R) dR\right), \quad (5.13)$$

where $\kappa(\lambda_L, R)$ and $\kappa(\lambda, R)$ are the atmospheric attenuation coefficients at the laser and detected wavelengths, respectively. Combining equation (5.12) and (5.13) leads to the total atmospheric transmission factor

$$T(R) = T(\lambda, R) \cdot T(\lambda_L, R) = \exp\left(-\int_0^R \{\kappa(\lambda_L, R) + \kappa(\lambda, R)\} dR\right). \quad (5.14)$$

The increment of radiation energy at wavelength λ received by the detector during the interval $(t, t+\tau_d)$, where τ_d is the integration period for the detector, is given by

$$E(\lambda, R) = \int_{2R/c}^{\tau_d + 2R/c} P(\lambda, t) dt. \quad (5.15)$$

combining equations (5.10), (5.11), (5.14) and (5.15) yields the scattered laser energy received within the detector's response time, τ_d :

$$E(\lambda, R) = E_L \xi(\lambda) \cdot T(R) \cdot \xi(R) \frac{A_o}{R^2} \beta(\lambda_L, \lambda, R) \frac{c\tau_d}{2}. \quad (5.16)$$

This is known as the basic scattering lidar equation.

For more general laser pulse shape, the average radiation power is given by

$$P_L = \frac{E_L}{\tau_L}, \quad (5.17)$$

and equation (5.16) will be modified to

$$P(\lambda, R) = P_L \frac{A_o}{R^2} \xi(\lambda) \cdot \xi(R) \cdot \beta(\lambda_L, \lambda, R) \frac{c\tau_L}{2} \cdot \exp\left(-\int_0^R \kappa(R) dR\right), \quad (5.18)$$

where from equation (5.14)

$$\kappa(R) = \kappa(\lambda_L, R) + \kappa(\lambda, R). \quad (5.19)$$

In the case of elastic (Mie or Rayleigh) scattering, the detected wavelength will be equal to the laser wavelength and will be given by

$$P(\lambda, R) = P_L \frac{A_o}{R^2} \xi(\lambda) \cdot \xi(R) \cdot \beta(\lambda_L, R) \frac{c\tau_L}{2} \cdot \exp\left(-2 \int_0^R \kappa(\lambda_L, R) dR\right). \quad (5.20)$$

Equation (5.18) is the scattering lidar equation, while equation (5.20) is a special case which is often used in the differential absorption lidar technique.

5.1.1. Receiver optics geometry

In the development of the scattering lidar equation the geometrical probability factor $\xi(R, r)$ was assumed unity wherever the field of view of the receiver optics overlaps the laser beam and zero elsewhere. Also, the distribution of the laser intensity was assumed uniform across the target plane. These assumptions are practical for long range measurements. For short range measurements these factors must be considered.

A more general form of the laser intensity at the range R given in equation (5.11) is

$$I(R, r, \psi) = \frac{P_L T(\lambda_L, R)}{\pi W^2(R)} F(R, r, \psi), \quad (5.21)$$

where r is the radial displacement of the point of interest in the target plane from the telescope axis and ψ is the corresponding azimuth angle from a vertical plane passing through this axis. As shown in Figure 5.1, $W(R)$ is the radius of the laser pulse in the

target plane, and $F(R, r, \psi)$ is the distribution of the laser power over the target plane at the instant of interest. The Gaussian distribution is common in this case and therefore

$$F(R, r, \psi) = \exp\left(-\left(\frac{r^*}{W(R)}\right)^2\right), \quad (5.22)$$

where

$$r^* = (r^2 + d^2 - 2 \cdot r \cdot d \cdot \cos \psi)^{1/2} \quad (5.23)$$

and d represent the separation of the laser beam and telescope axis. Assuming a TEM_{00} mode laser, the radius of the laser beam is given by

$$W(R) = (W_o^2 + \theta^2 R^2)^{1/2}, \quad (5.24)$$

where W_o is the laser output aperture radius and θ is half of the laser divergence angle.

Also, the radius of the field of view of the telescope at range R is given by

$$r_T(R) = r_o + \phi R, \quad (5.25)$$

where r_o is the effective radius of the telescope mirror and ϕ is half of the field of view angle of the telescope.

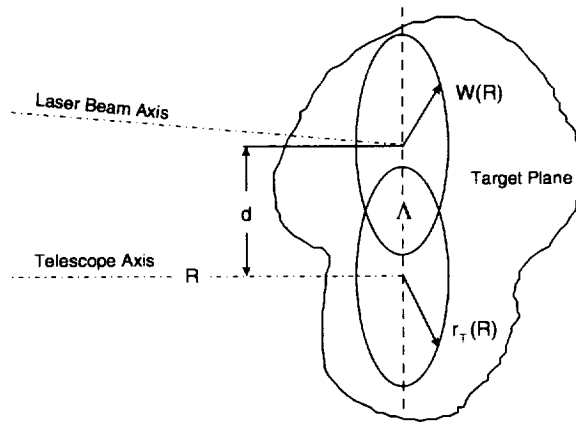


Figure 5.1 Geometry of the target plane at range R .

Substituting equation (5.21) in equation (5.7) will yield the total scattered laser power received by the detection system in the temporal duration τ_L and is given by

$$P(\lambda, t) = P_L \xi(\lambda) r_o^2 \int_{R=c(t-\tau_L)/2}^{R=ct/2} \frac{\beta(\lambda_L, \lambda, R) \cdot T(R)}{W^2(R) R^2} dR \times \int_{r=0}^{r_T} \int_{\psi=0}^{2\pi} \xi(R, r, \psi) \cdot F(R, r, \psi) \cdot r \cdot dr d\psi. \quad (5.26)$$

This equation can be further simplified considering that the range R is much greater than the laser pulse length; therefore, the range dependent functions can be considered constants in the small integration period. Thus, equation (5.26) can be written as

$$P(\lambda, t) = P_L \frac{c\tau_L}{2} \xi(\lambda) \frac{r_o^2}{R^2} \beta(\lambda_L, \lambda, R) \frac{T(R)}{W^2(R)} \times \int_{r=0}^{r_T} \int_{\psi=0}^{2\pi} \xi(R, r, \psi) \cdot F(R, r, \psi) \cdot r \cdot dr d\psi. \quad (5.27)$$

In this case, the telescope effective area can be defined as

$$A(R) = \frac{A_o}{\pi W^2(R)} \times \int_{r=0}^{r_T} \int_{\psi=0}^{2\pi} \xi(R, r, \psi) \cdot F(R, r, \psi) \cdot r \cdot dr d\psi, \quad (5.28)$$

where $A_o = \pi r_o^2$. Therefore, the scattering lidar equation (5.18) can be re-written as

$$P(\lambda, R) = P_L \frac{A(R)}{R^2} \xi(\lambda) \cdot \beta(\lambda_L, \lambda, R) \frac{c\tau_L}{2} \cdot \exp\left(-\int_0^R \kappa(R) dR\right) \quad (5.29)$$

in which $A(R)$ in equation (5.29) has replaced $A_o \xi(R)$ in equation (5.18).

5.1.2. Geometrical form factor for simple overlap

Using equation (5.28), the definition of the geometrical form factor $\xi(R)$ is given by

$$\xi(R) = \frac{1}{\pi W^2(R)} \times \int_{r=0}^{r_T} \int_{\psi=0}^{2\pi} \xi(R, r, \psi) \cdot F(R, r, \psi) \cdot r \cdot dr d\psi. \quad (5.30)$$

Assuming a uniform intensity distribution over the area of illumination at the range R and considering a biaxial receiver system in which the laser axis is separated from the telescope optical axis by a distance d , the geometrical form factor can be taken as a simple overlap factor and can be written as

$$\xi(R) = \frac{\Lambda\{r_T(R), W(R), d(R)\}}{\pi W^2(R)}, \quad (5.31)$$

where Λ is the area overlap function. The separation between the laser and telescope axes in the target plane is

$$d = d_o - R\delta, \quad (5.32)$$

where d_o is the separation at the lidar receiver and δ is the inclination angle between the laser and the telescope axes.

The area overlap function assumes three cases as indicated in Figure 5.2. The first (a) in which the telescope field of view does not overlap with the laser, the second (b) in which there will be a partial overlap and the third (c) will be for full overlap. Therefore, Λ will be given by^{5,84-85}

$$\Lambda = \begin{cases} 0 & d > r_T + W \\ W^2 \psi_w + r_T^2 \psi_r - r_T d \sin \psi_r & |r_T - W| < d < r_T + W, \\ \pi r_T^2 & d < |r_T - W| \end{cases} \quad (5.33)$$

where

$$\psi_w = \cos^{-1} \left(\frac{d^2 + W^2 - r_T^2}{2Wd} \right) \quad (5.34)$$

and

$$\psi_r = \cos^{-1} \left(\frac{d^2 + r_T^2 - W^2}{2r_T d} \right). \quad (5.35)$$

The situation of partial overlap is shown in Figure 5.3.

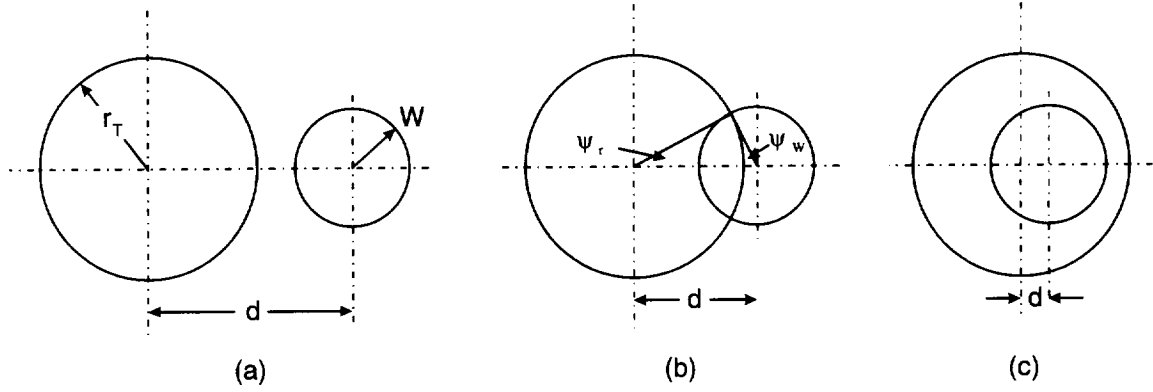


Figure 5.2 The three possible cases for telescope field of view and laser overlap functions, (a) no overlap (b) partial overlap and (c) total overlap.

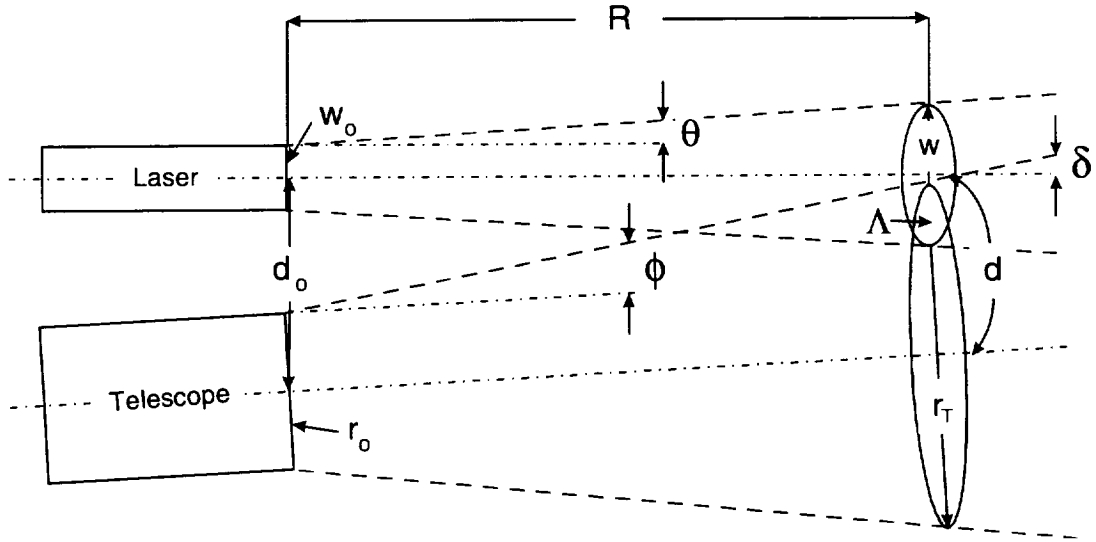


Figure 5.3 Geometry of the biaxial lidar illustrating the condition of partial overlap.

Introducing non-dimensional parameters as

$$z = \frac{R}{r_0}, \quad A = \frac{r_0}{w_0}, \quad D = \frac{d_0}{r_0}, \quad \rho(z, \phi) = \frac{r_T}{r_0} = 1 + z\phi, \quad s(z, \delta) = \frac{d}{r_0} = D - z\delta,$$

$$\varpi(z, \theta) = \frac{W}{W_0} = \{1 + z^2 \theta^2 A^2\}^{1/2}, \quad \text{and} \quad y(z, \theta, \phi) = \frac{\varpi^2(z, \theta)}{\rho^2(z, \phi) A^2},$$

the overlap factor $\xi(R)$ can be expressed by^{5,84-85}

$$\xi(R) = \begin{cases} 0 & d > r_T + W \\ \frac{\psi_w(z)}{\pi} + \frac{1}{\pi y(z)} \left[\psi_r(z) - \frac{s(z)}{\rho(z)} \sin \psi_r(z) \right] & |r_T - W| < d < r_T + W, \\ r_T^2(R)/W^2 & d < |r_T - W| \end{cases} \quad (5.36)$$

where

$$\psi_w(z) = \cos^{-1} \left(\frac{s^2(z) + y(z)\rho^2(z) - \rho^2(z)}{2s(z)\rho(z)\sqrt{y(z)}} \right) \quad (5.37)$$

and

$$\psi_r(z) = \cos^{-1} \left(\frac{s^2(z) + \rho^2(z) - y(z)\rho^2(z)}{2s(z)\rho(z)} \right). \quad (5.38)$$

5.2. The DIAL Equation

Differential absorption lidar (DIAL) is a powerful technique to selectively measure the density of molecules in the atmosphere as a function of altitude. It involves using two laser pulses of slightly different wavelength. One is chosen to coincide with a strong absorption feature of the specific molecular of interest and is known as the on-line wavelength λ_{on} . The other is tuned to the side of the absorption feature where there is no absorption and is known as the off-line wavelength λ_{off} as illustrated in Figure 5.4.

The derivation of the DIAL measuring technique starts by considering the scattering lidar equation (5.20) and modifying the total attenuation coefficient $\kappa(\lambda, R)$ to

$$\kappa(\lambda, R) \equiv \kappa'(\lambda, R) + N(R)\sigma(\lambda), \quad (5.39)$$

where $\kappa'(\lambda, R)$ is the attenuation coefficient exclusive of the absorption contribution from the molecular of interest, $N(R)$ is the number density of the molecular species at range R and $\sigma(\lambda)$ is the absorption cross section at wavelength λ . Therefore, applying the lidar equation (5.20) at both the on and off-line wavelengths respectively, we get

$$P(\lambda_{\text{on}}, R) = P_L \frac{A_o}{R^2} \xi(\lambda_{\text{on}}) \xi(R) \beta(\lambda_{\text{on}}, R) \frac{c\tau_L}{2} \exp\left(-2 \int_0^R [\kappa(\lambda_{\text{on}}, R) + N(R)\sigma_{\text{on}}(\lambda_{\text{on}})] dR\right) \quad (5.40)$$

$$P(\lambda_{\text{off}}, R) = P_L \frac{A_o}{R^2} \xi(\lambda_{\text{off}}) \xi(R) \beta(\lambda_{\text{off}}, R) \frac{c\tau_L}{2} \exp\left(-2 \int_0^R [\kappa(\lambda_{\text{off}}, R) + N(R)\sigma_{\text{off}}(\lambda_{\text{off}})] dR\right) \quad (5.41)$$

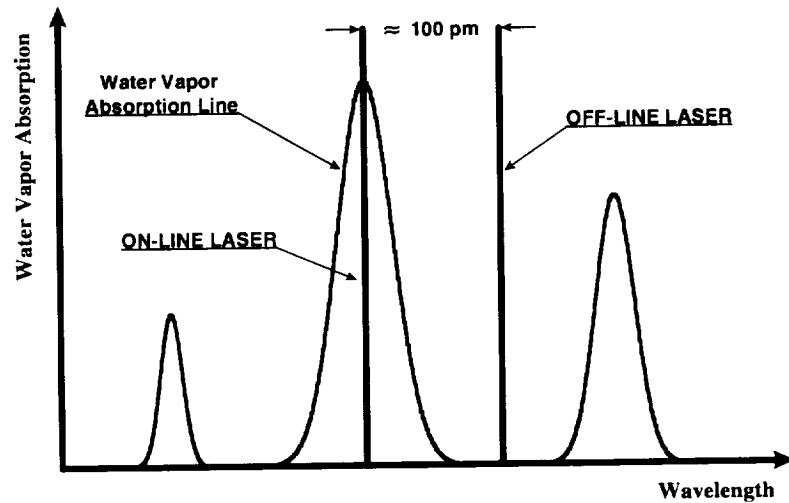


Figure 5.4 DIAL on-line and off-line wavelengths relative to water vapor absorption line.

Then, the ratio of the return signals at the two wavelengths is obtained by dividing equation (5.40) by (5.41) to obtain

$$\frac{P(\lambda_{\text{on}}, R)}{P(\lambda_{\text{off}}, R)} = \exp\left(-2 \int_0^R N(R) \Delta\sigma dR\right), \quad (5.42)$$

where the difference between the on and off-line wavelengths is less than 0.1 nm. Therefore, one can assume that the receiver spectral transmission factor is independent of wavelength over this small interval and similarly for the volume backscattering coefficients and atmospheric attenuation coefficients. Also, the output laser power is assumed equal for both wavelengths, and $\Delta\sigma = \sigma_{\text{on}} - \sigma_{\text{off}}$ is the differential absorption cross section.

To evaluate the integration in equation (5.42), we use two successive ranges, R_1 and R_2 respectively, to obtain

$$\frac{P(\lambda_{\text{on}}, R_1)}{P(\lambda_{\text{off}}, R_1)} = \exp\left(-2 \int_0^{R_1} N(R) \Delta\sigma dR\right) \quad (5.43)$$

$$\frac{P(\lambda_{\text{on}}, R_2)}{P(\lambda_{\text{off}}, R_2)} = \exp\left(-2 \int_0^{R_2} N(R) \Delta\sigma dR\right). \quad (5.44)$$

Therefore,

$$2\Delta\sigma \int_{R_1}^{R_2} N(R) dR = \ln \left[\frac{P(\lambda_{\text{on}}, R_1) P(\lambda_{\text{off}}, R_2)}{P(\lambda_{\text{off}}, R_1) P(\lambda_{\text{on}}, R_2)} \right]. \quad (5.45)$$

The number density function can be assumed constant in the small interval $\Delta R = R_2 - R_1$ which defines the range cell. Hence, we get

$$N(R) = \frac{1}{2\Delta\sigma \Delta R} \ln \left[\frac{P(\lambda_{\text{on}}, R_1) P(\lambda_{\text{off}}, R_2)}{P(\lambda_{\text{off}}, R_1) P(\lambda_{\text{on}}, R_2)} \right]. \quad (5.46)$$

Equation (5.46) is known as the differential absorption lidar or DIAL equation, and it is used to obtain the number density of a specific molecular species as a function of range.

5.3. Applied Lidar Measurement Technique

In a typical lidar system, the return scattered radiation is collected by the receiver telescope and then applied to a detector using focusing optics in order to convert the optical signal into an electric one. Furthermore, the electric signal is digitized and stored in digital form in a storage device. The stored data is available in the form of digitizer counts versus number of samples, as shown in Figure 5.5. Knowing the digitization frequency f_s and considering the speed of light in air, the sample intervals can be transformed into altitude or range using the range cell R_c relation

$$R_c = \frac{c}{2f_s} . \quad (5.47)$$

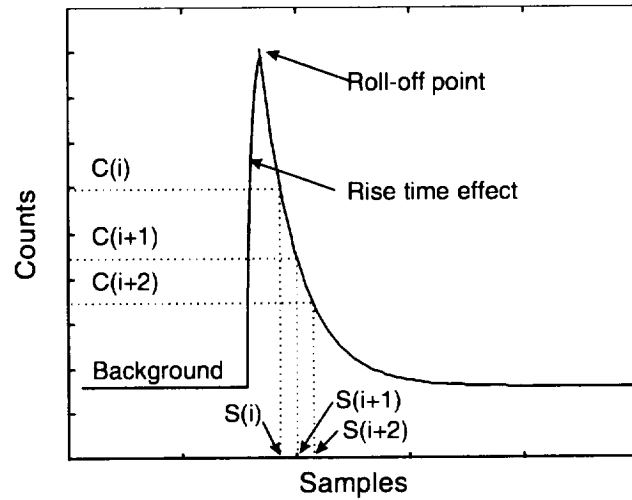


Figure 5.5 Ideal lidar return signal as obtained from the digitizer output.

The roll-off from the peak count in the return signal defines the beginning of the useful data. The maximum altitude or range is obtained by considering the minimum count, which corresponds to the receiver system signal-to-noise ratio, after subtracting the signal background.

5.3.1. Aerosol measurement

To measure the aerosol density as a function of altitude, the visible and infrared laser beams are used.⁸⁶ These wavelengths are not absorbed but scattered by the molecular and aerosols species; thus, we can use the backscattering lidar equation (5.20). The atmospheric volume backscattering coefficient has the form of

$$\beta(\lambda_L, R) \approx \beta(R) = N(R) \frac{\sigma^s(\lambda)}{4\pi}. \quad (5.48)$$

To obtain the aerosol profile (relative measurements) equation (5.20) can be simplified to

$$P(R) = (\text{constant}) \cdot \frac{N(R)}{R^2} \cdot O_T, \quad (5.49)$$

where the geometrical probability factor $\xi(R)$ is considered unity for full overlap and O_T is the optical thickness defined by the exponential term of equation (5.20) considering the atmospheric attenuation coefficients of scattering species⁸⁷. Comparing the aerosol profile to the standard atmospheric number density $N_{STD}(R)$ ⁸⁸, results in the aerosol scattering ratio expressed by

$$N(R) = N_{STD}(R) \cdot N_{SR}(R). \quad (5.50)$$

Considering the digitizer gain G_d expressed in counts/(W/m²), the digitizer counts, C_d , can be converted to the return signal power and the aerosol scattering ratio can be obtained by

$$N_{SR}(R) = \frac{1}{G_d(\text{constant})} \cdot \frac{C_d(i)R^2}{O_T N_{STD}(R)} \quad (5.51)$$

and

$$R = i \cdot \frac{R_c}{2f_s}, \quad (5.52)$$

where i is the sample number. To avoid the complexity of evaluating the constant term of equation (5.51), the scattering ratio is usually normalized to the standard atmospheric number density at a chosen altitude.

5.3.2. Water vapor measurement

Using the DIAL equation (5.46), the water vapor number density $N_{wv}(R)$ can be obtained from the digitizer data according to

$$N_{wv}(R) = \frac{1}{2\Delta\sigma\Delta R} \cdot \frac{C_{off}(i+1) \cdot C_{on}(i)}{C_{off}(i) \cdot C_{on}(i+1)} \quad (5.53)$$

and

$$R = i \cdot \frac{R_c}{2f_s}, \quad (5.54)$$

where C_{on} and C_{off} are the on- and off-line return signal in counts. In order to smooth the water vapor profile, averaging can be used for M data points where

$$C'(i) = \frac{\sum_{j=i}^M C(j)}{M}. \quad (5.55)$$

In this case, the range cell given in equation (5.47) will be modified to

$$R_c = \frac{c}{2f_s} M. \quad (5.56)$$

CHAPTER VI

VALIDATION OF THE DETECTION SYSTEM

The validation of the new water vapor detection system is discussed in this chapter. The new detection system was connected to a telescope with focusing optics and filter to construct a lidar receiver system. This receiver system was used to measure the atmospheric return signals for relative aerosol and absolute water vapor density measurements as a function of altitude. The aerosol measurement was obtained simultaneously with NASA Langley Research Center ozone and aerosol DIAL system.^{6,84} The water vapor measurement was obtained by using a telescope and a laser transmitter manufactured by Science and Engineering Services, Inc. (SESI).⁸⁹⁻⁹² The measured water vapor profile was compared with profiles obtained from Dulls Airport and Wallops Island radiosondes.⁹³

6.1. Receiver system setup

The new water vapor DIAL detection system was attached to a telescope and focusing optics in order to build a lidar receiver system. The receiver is compatible with radiation in the visible for aerosol measurement and near infrared region for water vapor density measurements. A schematic diagram of this receiver system used for both aerosol and water vapor measurements is shown in Figure 6.1.

Both 30.5 cm and 35.6 cm diameter telescopes were used to collect backscattered radiation for aerosol and water vapor measurements respectively. These telescopes had a Newtonian design with parabolic mirrors to focus the radiation and a flat mirror to turn

the focus on an optical fiber. A mechanism was used to allow the telescope to move in two-dimension plane to focus the backscattered signal. The optical fiber had a 1 mm diameter silica core and a doped silica clad of 1.1-mm with a 0.28 numerical aperture. This optical fiber was custom designed by Cerme Optic, Inc. with an operating wavelength range of 200 to 1200 nm. The use of the optical fiber eliminates the need to align the focusing optics with the telescope for compact receiver systems.

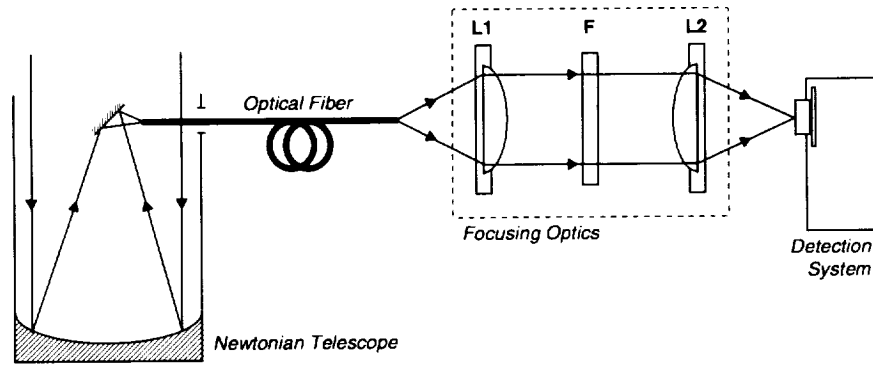


Figure 6.1 Water vapor DIAL detection system as a part of the receiver.

The focusing optics consists of a plano-convex lens L1, a narrow-band interference filter F and another plano-convex lens L2, as indicated in Figure 6.1. The filter was changed according to the wavelength of the transmitted laser. The output beam is aligned with the APD sensitive area using a three-dimension translation-stages mechanism to move the detection system. Assuming a Gaussian beam distribution and considering the diffraction effect, the light spot diameter at the focus d_A containing 84% of the total energy (Airy disk diameter) is defined by

$$d_A = 2.44 \frac{\lambda \cdot F}{D}, \quad (6.1)$$

where F and D are the focal length and the diameter of the focusing lens $L2$. The focal spot diameter was checked for every operating conditions in order to insure that the APD sensitive area is not over-flown by the incoming light.

The alignment of the focusing optics with the APD sensitive surface was tested by simulating the lidar return using a stroboscope as a light source as shown in Figure 6.2. The telescope collects the reflected light signal from the ceiling and the focusing optics focuses the optical signal onto the APD. The trigger generator is used for synchronizing the detection system with the stroboscope optical signal. This was done by triggering both devices simultaneously with the delay unit used to adjust the collected signal in the digitizer time window. The alignment was obtained by moving the detection system in three-dimensions to give the optimum output signal from the detection system as shown in Figure 6.3.

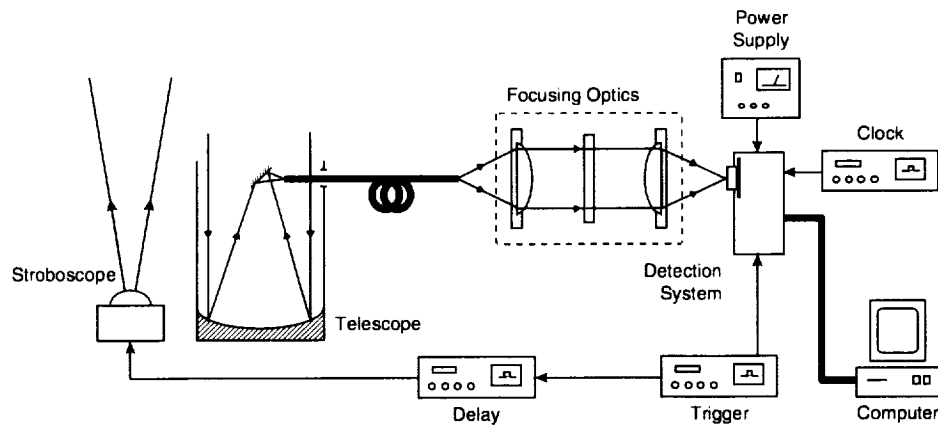


Figure 6.2 Focusing optics alignment setup with the detection system.

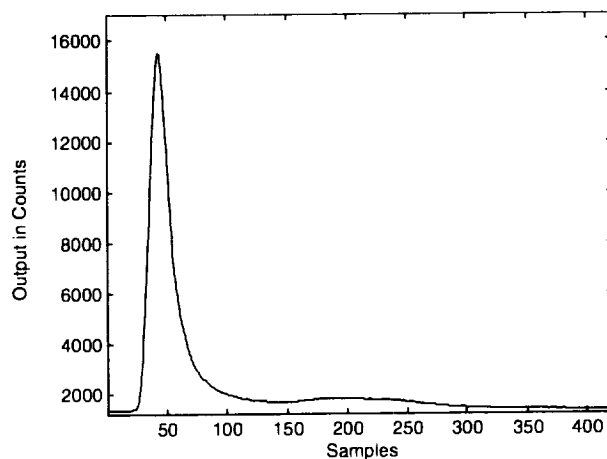


Figure 6.3 Detection system output corresponding to the best alignment.

6.2. Detection system validation with NASA airborne DIAL system

Simultaneous measurements of aerosol profiles were obtained using both the new detection system and the NASA Langley Research Center airborne DIAL system, as shown in Figure 6.4. The measurements were obtained during ground testing of the system carried out on October 7, 1999.

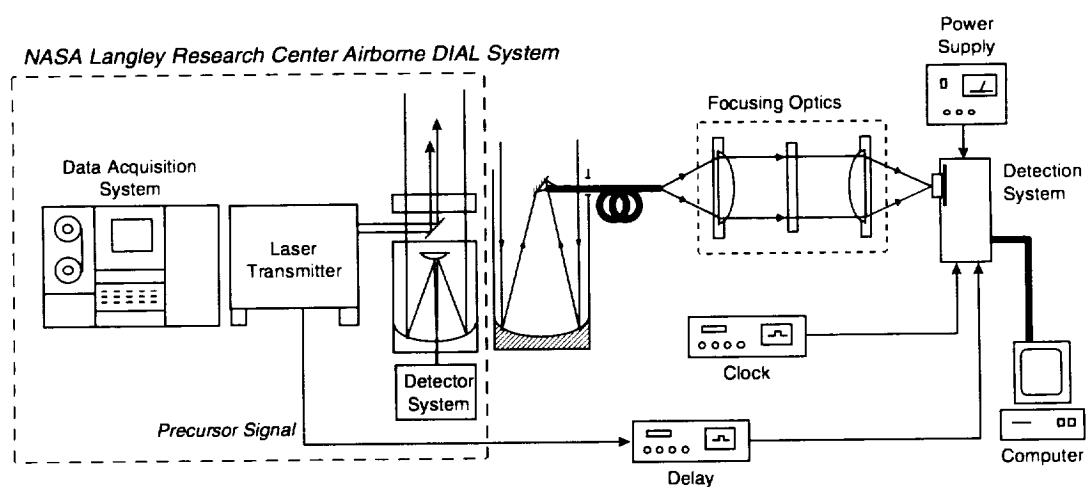


Figure 6.4 Detection system validation setup with NASA Langley Research Center airborne DIAL system.

The NASA DIAL system consists of a laser transmitter, a receiver with a telescope and a data acquisition system. The DIAL system measured aerosol backscattered profiles at 598-, 622- and 1064-nm wavelengths. The visible wavelengths were compatible with the new detection system and were used to validate it. The visible wavelengths were separated by 300 μ s with pulse energies of about 50 mJ for both wavelengths and a pulse duration of 15 ns. The laser fire frequency was 30 Hz while the receiver digitization rate was 1 MHz.

The new detection system was synchronized with the NASA DIAL system through the laser precursor signal which defines the time duration between the two laser pulses. This signal was applied to a delay stage, the output of which was used to trigger the new detection system. This delay was applied in order to adjust the backscattered return signals with the digitizer time window. The measured return signals from the new DIAL detection system are shown in Figure 6.5a and b for the 589- and 622-nm wavelengths respectively. The signals were obtained using 24 shot averages with 5-MHz digitization frequency applied using a separate clock generator. The digitization frequency was reduced in order to extend the time window to 1.64 ms. The 622-nm return signal shown in Figure 6.5 indicates an over-load which resulted in clipping of the return signal. As a result of the clipping stage, this over-load did not affect the measurement. This was indicated in Figure 6.6a which shows the aerosol profiles obtained from both systems compared to the atmospheric standard molecular density. The large aerosol return at lower altitude is due to the atmosphere boundary layer. The disagreement between the measurements at lower altitude may be due to the telescope misalignment in the near field region. Figure 6.6b shows similar profiles obtained at the-598 nm wavelength. The aerosol profiles of the new

detection system where calculated by applying equations (5.51) and (5.52) using a 300 m range cell.

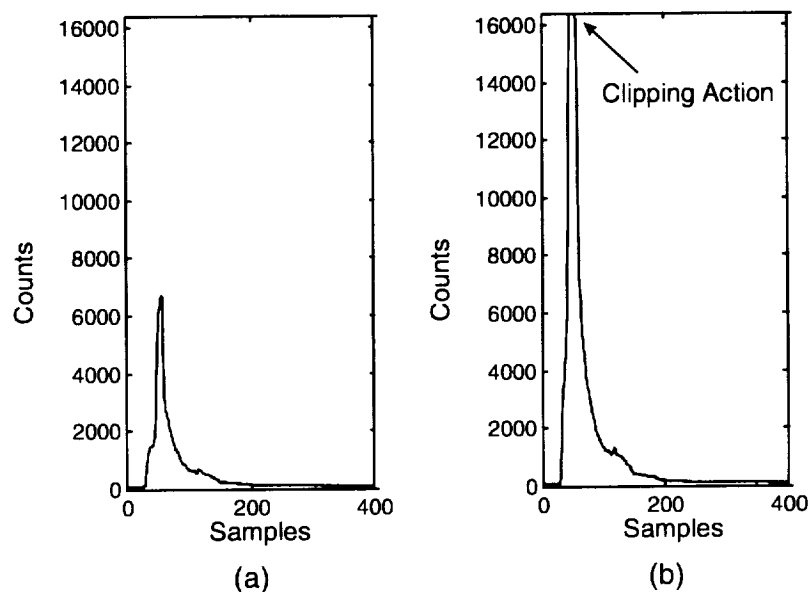


Figure 6.5 New detection system return signal obtained at (a) 598 nm and (b) 622 nm with 24 shot average and 5 MHz digitization frequency.

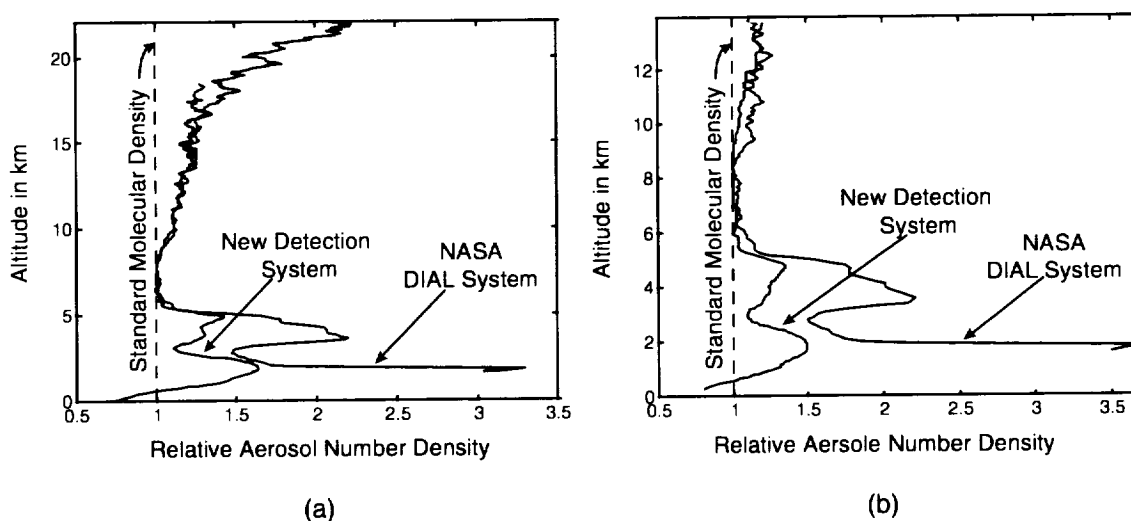


Figure 6.6 Aerosol profiles obtained from the NASA DIAL system and the new detection system at (a) 622 nm and (b) 598 nm compared to the atmospheric standard molecular density.

6.3. Water vapor DIAL detection system validation

Science and Engineering Services, Inc. of Burtonsville MD, has developed a compact diode-pumped Cr:LiSAF tunable laser to be used as the transmitter for water vapor DIAL measurements from robotic aircraft. This system operates at 816-nm wavelength with a maximum laser pulse energy of 25 mJ and a repetition rate of 5 Hz.

The new water vapor DIAL detection system was used with this transmitter. The optical fiber cable and the focusing optics were used in conjunction with a 30 cm diameter telescope to form a coaxial DIAL transmitter-receiver system. On November 5, 1999, this DIAL system was used to measure the atmospheric water vapor profile. The return signals for the on- and off-line are shown in Figure 6.7 for a 1000 shot average and 10-MHz digitization frequency. The on- and off-line wavelengths are 815.3251 and 815.3278, respectively, and the corresponding differential absorption cross-section is $5 \times 10^{-24} \text{ cm}^2$. The laser energy was about 20 mJ per pulse. The water vapor profile was compared to profiles obtained from radiosonde data from both Dulles Airport near Washington, D.C., and NASA Wallops, Wallops Island VA, as given in tables 6.1 and 6.2 respectively. Figure 6.8 shows the water vapor profiles from the radiosondes and the DIAL system obtained using a 600 m range cell. The water vapor mass mixing ratio, r , obtained from the radiosonde data were converted to number density, n , according to the relation

$$n = \frac{N_A}{M} \cdot r \cdot \rho_s, \quad (6.2)$$

where N_A is Avogadro's number, M is the molecular weight of water which is equal to 18 kg/kmole and ρ_s is the air density. According to the ideal gas law, since the air density is a function of both temperature and pressure, its value was obtained as a function of altitude

referring to the standard atmospheric data of the United States at zero altitude, where the air pressure, temperature and density are 1.01325×10^3 mBar, 288.15 K and 1.225 kg/m^3 respectively.⁸⁷

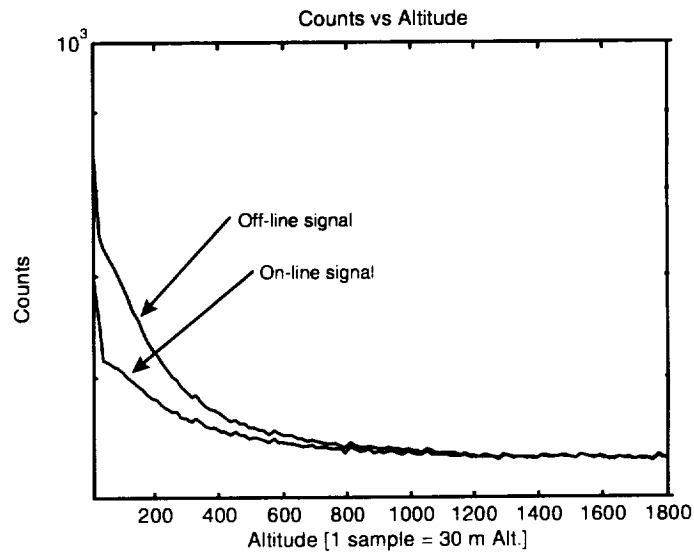


Figure 6.7 On and off-line return signals.

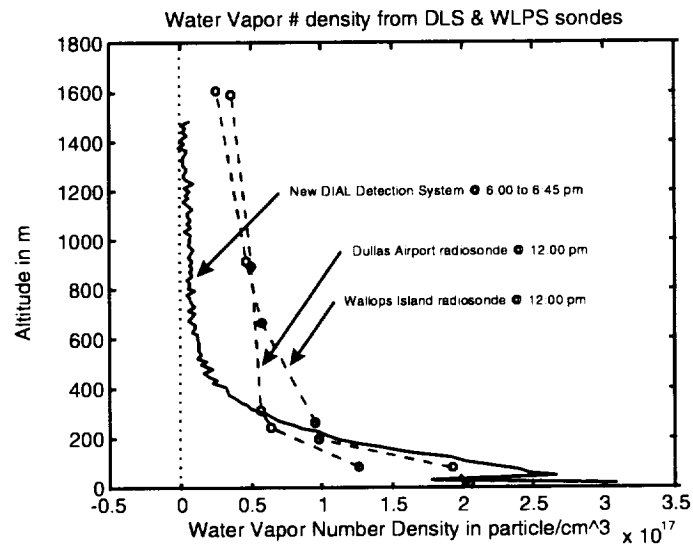


Figure 6.8 Water vapor profiles obtained from the new system and radiosondes.

Table 6.1 Dulles Airport water vapor profile data on November 5, 1999 at 12:00 pm.

Altitude M	Temperature °C	Pressure mBar	Density kg/m ³	Water Vapor	
				gm/kg	Cm ⁻³
82	-2.3	1020	1.31193	2.89	1.3x10 ¹⁷
242	9.2	1000	1.23382	1.55	6.4x10 ¹⁶
309	13.8	992	1.20432	1.39	5.6x10 ¹⁶
893	9.2	925	1.14128	1.31	5.0x10 ¹⁶
1587	4.0	850	1.06842	1.00	3.6x10 ¹⁶

Table 6.2 Wallops Island water vapor profile data on November 5, 1999 at 12:00 pm.

Altitude M	Temperature °C	Pressure mBar	Density kg/m ³	Water Vapor	
				gm/kg	cm ⁻³
16	8.6	1030	1.2735	4.81	2.0x10 ¹⁷
80	9.8	1022	1.2483	4.58	1.9x10 ¹⁶
195	13.8	1008	1.2237	2.38	9.7x10 ¹⁶
262	13.4	1000	1.2157	2.33	9.5x10 ¹⁶
664	11.0	953	1.1684	1.47	5.7x10 ¹⁶
911	9.2	925	1.1413	1.20	4.6x10 ¹⁶
1606	4.0	850	1.0684	0.71	2.5x10 ¹⁶

Figure 6.8 indicates a good agreement between the DIAL system and the radiosonde systems specially in the near-field. The deviation in the far-field might be due to the difference in measurement location and time. Therefore, the expected return signal had to be calculated using the lidar equation.

The measured return signals were compared to the expected return signal, calculated from the lidar equation (5.16). Both signals are shown in Figure 6.9. To obtain this profile, the geometrical form factor was considered for total overlap condition and was calculated using equation (5.36). The transmitted laser beam had a 2-mm diameter with 10^{-3} radian divergence angle and 3×10^{-3} radian telescope field of view. The total atmospheric transmission factor was calculated considering the optical thickness and the standard atmospheric number density given in equations (5.49) and (5.50) respectively. Good

agreement between the measured and calculated profiles, as shown in Figure 6.9, indicates the validity of the new DIAL detection system.

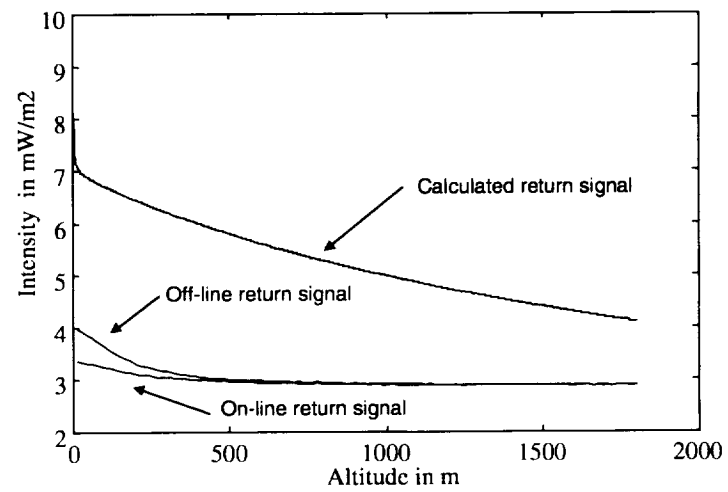


Figure 6.9 Measured and calculated return signals.

CHAPTER VII

CONCLUSIONS

In this dissertation, an advanced water vapor DIAL detection system was designed, constructed and evaluated. The system consists of an advanced APD detector, an analog circuit and a digital circuit all on one, small size low mass, printed circuit board. The system was interfaced to a personal computer. Both atmospheric aerosol and water vapor concentration profiles were measured using this system.

The optical detector is a critical device in this system. A drift diffusion model was developed for the APD to better understanding the device operation. This model is suitable to solve for the device transient and steady-state operation assuming a four-layer structure such as the reach-through and SLIK APD structures. An equivalent circuit was also presented in order to model these devices in circuit simulation packages.

The APD choice was based on characterizing a group of such devices with different structures from different manufactures. The characterization results indicate the better performance of the SLIK structure over the reach-through structure in terms of noise and device stability with respect to temperature. The selected advanced APD package had the advantages of a built-in TEC and thermistor for temperature control and built-in trans-impedance amplifier for direct current to voltage conversion.

The new detection system consists of an analog circuit and a digital circuit. The analog circuit was designed using state-of-the-art electronics and controlled the APD in terms of operating temperature and bias voltage. Also, it consists of a signal conditioning stage, which adjusted the APD output to be compatible with the digitizer circuit.

The digital circuit consists of a digitizer, microcontroller and output circuit. The digitizer was constructed using a state-of-the-art 14-bit, 10-MHz ADC, a dual port RAM and a 13-bit counter to address the storage locations of the ADC output. The microcontroller was used to synchronize the detection system with the laser fire pulse. Also, it can perform real time averaging of the recorded data and monitor the APD operating bias voltage and temperature. The output stage consists of a FIFO which is used to collect the digital data and transfer it to a personal computer for storage.

The system design assumes an external power supply, clock and trigger signals. The whole system was integrated onto one small printed circuit board suitable to be mounted directly on the lidar receiver telescope. The final digital data is read using a parallel input-output interface with up to a 20 MHz data transfer rate. The operation of this interface is completely controllable using software. The final data is stored in an ASCII file which is accessible with any data handling software. The summary of the detection system performance parameters is given in table 7.1.

The detection system validation started by reviewing the theory of the lidar remote sensing technique with a special focus on the DIAL measuring technique. The transformation from raw data representing the detection system output into a meaningful atmospheric water vapor profile was also discussed. The integration of the detection system into a complete receiver, using focusing optics and a telescope allowed the validation of the system experimentally. One validation experiment was obtained by measuring relative aerosol profiles simultaneously with the NASA Langley Research Center airborne aerosol and ozone DIAL system. The other validation experiment was obtained by integrating the new receiver system with a laser transmitter manufactured by

Science and Engineering Services Inc., and measuring water vapor profile which were compared to Dulles Airport and Wallops Island water vapor radiosonde results. Both experiments demonstrated the capability of the system in terms of range and measuring atmospheric species other than water vapor.

Table 7.1 DIAL detection system performance summary.

End-to-end gain	183,969 counts/(W/m ²)
Maximum output	16383 counts
Minimum detectable signal @ 820 nm	0.85 μ W/m ²
Maximum detectable signal @ 820 nm	0.84 mW/m ²
Dynamic range	1000
Maximum digitization frequency	10 MHz
Maximum time window	819.2 μ s
Maximum repetition rate (8 k word)	10 Hz
Total Noise Equivalent Power (NEP)	212 fW/Hz ^{1/2}
Power consumption	21.1 W
Card size	15x9 cm ²
Card weight	312 gm
Power supplies	± 5 V and ± 12 V
APD Sensitive area	0.238 mm ²

Although the system performance is acceptable, future research is required for additional improvements. One such improvement would be to replace the current ADC with a 16-bit, 20-MHz ADC. The availability of fast computer interfaces suggests omitting the microcontroller, which would result in even a more compact system. Also, more effort is needed in developing the SLIK structure APDs with larger sensitive areas.

The good performance of the system suggested its application in aircraft based water vapor DIAL systems such as the LASE instrument and space based DIAL systems such as the visible channel of the Ozone Research with Advanced Cooperative Lidar Experiment (ORACLE).

REFERENCES

1. Robert Christopherson, *Geosystems; An Introduction to Physical Geography*, Macmillan Publishing Company, New York (1992).
2. D. O'C. Starr & S. H. Melfi, "The role of water vapor in climate; a strategic research plan for the proposed GEWEX water vapor project," *NASA Conference Publication* **3120** (1991).
3. Z. Zhang and T. Krishnamurti, "Ensemble forecasting of hurricane tracks," *Bulletin of the American Meteorological Society* **78**(12), 2785-2795 (1997).
4. T. Krishnamurti and D. Oosterhof, "Prediction of the life cycle of a super-typhoon with a high resolution global model," *American Meteorological Society* **70**(10), 1218-1230 (1989).
5. Raymond Measures, *Laser Remote Sensing; Fundamentals and Applications*, John Wiley & Sons, Inc., New York (1984).
6. E. Browell, S. Ismail and W. Grant, "Differential absorption lidar (DIAL) measurements from air and space," *Applied Physics B* **67**, 399-410 (1998).
7. A. Moore, K. Brown, W. Hall, J. Barnes, W. Edwards, L. Petway, A. Little, W. Luck, I. Jones, C. Antill, E. Browell & S. Ismail, "Development of the lidar Atmospheric Sensing Experiment (LASE)- an advanced airborne DIAL instrument" 18th International Laser Radar Conference, *Advances in Atmospheric Remote Sensing with Lidar*, 281-288 (1997).
8. E. Browell, S. Ismail, W. Hall, A. Moore, S. Kooi, V. Brackett, M. Clayton, J. Barrick, F. Schmidlin, N. Higdon, S. Melfi and D. Whiteman, "LASE Validation Experiment," 18th International Laser Radar Conference, *Advances in Atmospheric Remote Sensing with Lidar*, 281-288 (1997).
9. R. Ferrare, S. Ismail, E. Browell, V. Brackett, S. Kooi, M. Clayton, S. Melfi, D. Whiteman, G. Schwemmer, K. Evans, P. Hobbs, J. Veefkind, P. Russell, J. Livingston, P. Hignett, B. Holben and L. Remer, "LASE measurements of aerosols and water vapor during TARFOX,"

- 19th International Laser Radar Conference, *NASA Conference Publication 207671*, 11-14 (1998).
10. S. Ismail, E. Browell, R. Ferrare, C. Senff, K. Davis, D. Lenschow, S. Kooi, V. Brackett and M. Clayton, "LASE measurements of convective boundary layer development during SGP97," 19th International Laser Radar Conference, *NASA Conference Publication 207671*, 261-264 (1998).
 11. V. Brackett, S. Ismail, E. Browell, S. Kooi, M. Clayton, R. Ferrare, P. Minnis, B. Getzwich and J. Staszal, "LASE validation experiment: preliminary processing of relative humidity from LASE derived water vapor in the middle to upper troposphere," 19th International Laser Radar Conference, *NASA Conference Publication 207671*, 465-468 (1998).
 12. W. Edwards, L. Petway and W. Antill, "Performance Improvement to the lidar atmospheric sensing experiment LASE," 19th International Laser Radar Conference, *NASA Conference Publication 207671*, 815-817 (1998).
 13. A. Moore and L. Matthews, "Conversions to the lidar atmospheric sensing experiment (LASE) instrument for nadir and zenith measurements," 19th International Laser Radar Conference, *NASA Conference Publication 207671*, 819-821 (1998).
 14. E. Browell, T. Wilkerson and T. McIlrath, "Water vapor differential absorption lidar development and evaluation" *Applied Optics* **18**(20), 3473- 3482 (1979).
 15. S. Ismail and E. Browell, "Airborne and spaceborne lidar measurements of water vapor profiles: a sensitivity analysis" *Applied Optics* **28**(17), 3603-3615 (1989).
 16. N. Higdon, E. Browell, P. Ponsardin, B. Grossmann, C. Butler, T. Chyba, M. Mayo, R. Allen, A. Heuser, W. Grant, S. Ismail, S. Mayor and A. Carter, "Airborne differential absorption lidar system for measurements of atmospheric water vapor and aerosols," *Applied Optics* **33**(27), 6422-6438 (1994).

17. R. DeYoung, G. Halama, W. Luck, K. Ellis, S. Sandford, E. Browell and T. Refaat
 "Advanced detectors, optics, and waveform digitizers for aircraft DIAL water vapor
 measurements" *Proceedings of SPIE* **3127**, 103-115 (1997).
18. T. Refaat, W. Luck & R. DeYoung, "Advanced detector and waveform digitizer for water
 vapor DIAL systems" 19th International Laser Radar Conference, *NASA Conference
 Publication* **207671**, 845-848 (1998).
19. T. Refaat, W. Luck & R. DeYoung, "Advanced water vapor DIAL detection system",
Conference on Lasers and Electro-Optics, 1999 Technical Digest, Baltimore, 524 (1999).
20. T. Refaat, W. Luck & R. DeYoung, "An advanced water vapor lidar detection system for
 aircraft and space deployment" *Proceeding of SPIE* **3756**, 92-99 (1999).
21. T. Refaat, R. DeYoung and H. Ali, "A drift-diffusion model for reach-through avalanche
 photodiodes," *IEEE Journal of Quantum Electronics*, Under Review.
22. T. Refaat, G. Halama and R. DeYoung, "Characterization of advanced avalanche photodiodes
 for water vapor differential absorption lidar receivers", *NASA Technical Publications* **210096**
 (2000).
23. T. Refaat and R. DeYoung "Validation of an advanced lidar detection system for aerosol and
 water vapor measurements," 20th *International Laser Radar Conference*, to be published.
24. Bahaa Saleh & Malvin Teich, *Fundamentals of Photonics*. John Wiley & Sons, Inc.,
 New York (1991).
25. Eustace Dereniak & Devon Crowe, *Optical Radiation Detectors*, John Wiley & Sons,
 Inc., New York (1991).
26. Govind Agrawal, *Fiber-Optic Communication Systems*, 2nd ed, John Wiley & Sons,
 Inc., New York (1997).

27. Robert Boyd, *Radiometry and the Detection of Optical Radiation*, John Wiley and Sons, New York (1983).
28. P. Webb, R. McIntyre & J. Conradi, "Properties of Avalanche Photodiodes", *RCA Review*, EG&G Optoelectronics, Canada (1974).
29. *Avalanche photodiodes: a user's guide*, EG&G Optoelectronics, Canada.
30. R. McIntyre, "Recent developments in silicon avalanche photodiodes," *Measurement* **3**(4), 146-152 (1985).
31. H. Dautet, P. Deschamps, B. Dion, A. MacGregor, D. MacSween, R. McIntyre, C. Trottier and P. Webb, "Photon counting techniques with silicon avalanche photodiodes," *Applied Optics* **32**(21), 3894-3900 (1993).
32. H. Ruegg, "An optimized avalanche photodiode," *IEEE Transaction on Electron Devices* **ED-14**(5), 239-251 (1967).
33. W. Chen and S. Liu, "PIN avalanche photodiodes model for circuit simulation," *IEEE Journal of Quantum Electronics* **32**(12), 2105-2111 (1996).
34. Data Sheet, "*High Speed Solid State Detectors for Fiber Optic and Very Low Light-Level Applications; Silicon Avalanche Photodiodes C30902E, C30902S, C30921S,*" EG&G CANADA LTD., Optoelectronic Division (1991).
35. Dieter Schroder, *Semiconductor Material and Device Characterization*, John Wiley & Sons, Inc., New York (1990).
36. R. J. McIntyre, "Silicon Avalanche Photodiode with Low Multiplication Noise," *United State Patent 4972242*, 1990.
37. M. Omar and L. Reggiani, "Drift and diffusion of charge carriers in silicon and their empirical relations to the electric field," *Solid State Elect.* **30**(7), 693-697 (1987).

38. Sheng Li, *Semiconductor Physical Electronics*, Plenum Press, New York (1993).
39. Allan Hambley, *Electronics, Atop-Down Approach to Computer-Aided Circuits Design*, Prentice Hall, Englewood Cliffs, New Jersey (1994).
40. Jacob Millman and Christos Halkias, *Integrated Electronics: Analog and Digital Circuits and Systems*, McGraw-Hill, Singapore (1987).
41. C. Lee, R. Logan, R. Batdorf, J. Kleimack and W. Wiegmann, "Ionization rates of holes and electrons in silicon," *Physical Review* **134**(3A), A761-A774 (1964).
42. M. Saritas and H. McKell, "Absorption coefficient of Si in the wavelength range between 0.80-1.16 μm ," *Journal of Applied Physics*, **61**(10), 4923-4925 (1987).
43. A. Spinelli, M. Ghioni, S. Cova and L. Davis, "Avalanche detector with ultraclean response for time-resolved photon counting," *IEEE Journal of Quantum Electronics* **34**(5), 817-821 (1998).
44. X. Sun and Frederic Davidson, "Phoron counting with silicon avalanche photodiodes," *Journal of Lightwave Technology* **10**(8), 1023-1032 (1992).
45. Hamamatsu Photonics K. K., *Photomultiplier Tube Principle to Application*, Hamamatsu (1994).
46. E. Lerner, "Avalanche photodiodes can count photons", *Laser Focus World* **32**(10), 93-102 (1996).
47. T. Refaat, G. Halama and R. De Young, "Comparison between reach through and super low κ structures APDs" *Optical Engineering* **990358** Under Review.
48. B. Griffin, "C30955E Silicon avalanche photodiode", EG&G, Optoelectronics, Canada (1985).
49. B. Dion, "C30649E Test data sheet", EG&G, Optoelectronics, Canada (1996).

50. Hamamatsu, "Photodiodes," Catalog No KPD 0001E04 (1995).
51. Albert Helfrick and William Cooper, *Modern Electronic Instrumentation and Measurement Techniques*, Prentice-Hall International, Inc., Englewood Cliffs, New Jersey (1990).
52. G. Clayton, *Operational Amplifiers*, English Language Gook Society, Butterworths, (1980).
53. T. Refaat, W. Luck and R. De Young, "Temperature control of avalanche photodiodes using thermo-electric coolers", *NASA Technical Memorandum 209689* (1999).
54. T. Kirn, D. Schmitz, J. Schwenke, T. Flugel, D. Renker and H. Wirtz, "Wavelength dependence of avalanche photodiode parameters," *Nuclear Instruments and Methods in Physic Research A***387**, 202-204 (1997).
55. J. Conradi, "Temperature Effects in Silicon Avalanche Diodes," *Solid State Electronics* **17**, 99-106 (1974).
56. C. Crowell & S. Sze, "Temperature Dependence of Avalanche Multiplication in Semiconductors", *Applied Physics Letters* **9**(6), 242-244 (1966).
57. H. Weakliem and D. Redfield, "Temperature dependence of the optical properties of silicon", *Journal of Applied Physics* **50**(3), 1491-1493 (1979).
58. K. Van-Vliet, "Noise limitations in solid state photodetectors", *Applied Optics* **6**(7), 1145-1168 (1967).
59. R. Redus and R. Farrell, "Gain and noise in very high gain avalanche photodiodes; theory and experiment", *SPIE Proceedings* **2859**, 288-297 (1996).
60. ORIEL Instruments, The Book of Photon Tools, ORIEL Instruments, Inc. Catalog (1996).

61. *MATLAB; High Performance Numeric Computation and Visualization Software*, Reference Guide, The Math Works, Inc., Natick, Mass (1993).
62. T. Refaat, W. Luck & R. DeYoung, "Design of advanced atmospheric water vapor differential absorption lidar (DIAL) detection system," *NASA Technical Publications* **209348** (1999).
63. Data Sheet, "Low Distortion, Wide Bandwidth Voltage Feedback Clamp Amps," *Analog Devices, Inc.* (1994).
64. Data Sheet, "160 MHz Rail-to-Rail Amplifier with Disable," Analog Devices, Inc. (1995).
65. Data Sheet, "2.5 MHz, 3 Pole, Low Pass Bessell Filter," K&L Microwave, Inc. (1993).
66. Data Sheet, "Dual Picoampere Input Current Op Amp," Analog Devices, Inc. (1994).
67. Data Sheet, "Programmable High Voltage Power Supply," Analog Modules, Inc. (1991).
68. The Engineering Stuff of Texas Instruments, Inc., *The Transistor and Diode Data Book*, Texas Instruments, Inc., Dallas (1973).
69. Data Sheet, "Complete 14-bit, 10 MSPS Monolithic A/D Converter," Analog Devices, Inc. (1997).
70. *TTL Logic Data Book*, Texas Instruments, Inc., Dallas (1994).
71. Albert Malvino, *Digital Computer Electronics; AN Introduction to Microcomputers*, 2nd edition, McGraw-Hill, Singapore (1985).
72. Data Sheet, "High Speed 16kx16 Dual Port Static RAM," Integrated Device Technology, Inc. (1995).
73. M. Baumann, "The most commonly asked questions about dual ports," *Integrated Device Technology, Inc. Application Notes* **91**, (1998).
74. *Embedded Microcontrollers*, Intel Literature, Mt. Prospect (1996).
75. *Embedded Applications, Volume 2*, Intel Literature, Mt. Prospect (1996).
76. Data Sheet, "CMOS Asynchronous FIFO," Integrated Device Technology, Inc. (1995).

77. R. De Voto, "Width expansion of syncFIFOs," *Integrated Device Technology, Inc. Application Notes* **83**, (1999).
78. G. Prelesnik and K. Goldblatt, "Using IDT syncFIFOs as parallel data delay lines," *Integrated Device Technology, Inc. Application Notes* **122**, (1999).
79. Data Sheet, "Hermetically Sealed, High Speed, High CMR, Logic Gate Optocouplers," Hewlett Packard (1998).
80. *DIO 6533 User Manual*, National Instruments, Inc., (1997).
81. Mickey Williams, *Essential Visual C++*, Sams Publishing, Indianapolis (1995).
82. K. Deevy, D. Sheehan and M. Byrne, "Build a single shot recorder to catch fast transients", *Integrated Device Technology, Inc. Application Notes* **296**, (1991).
83. "Dynamic Performance Testing Of A to D Converters," *Hewlett Packard Product Note* **5180A-2** (1991).
84. E. Browell, "Differential absorption lidar sensing of ozone," *Proceeding of the IEEE* **77**(3), 419-432 (1989).
85. S. McDermid, T. Walsh, A. Deslis and M. White, "Optical systems design for a stratospheric lidar system," *Applied Optics* **34**(27), 6201-6210 (1995).
86. D. Whiteman, S. Melfi and R. Ferrare, "Raman lidar system for measurement of water vapor and aerosols in the Earth's atmosphere," *Applied Optics* **31**(16), 3068-3082 (1992).
87. *U.S. Standard Atmosphere, 1976*, National Oceanic and Atmospheric Administration, National Aeronautics and Space Administration, United States Air Force, Washington, D. C. (1976).

88. L. Elterman, "UV, Visible, and IR attenuation for altitudes to 50 km," *Air Force Cambridge Research Laboratories, Environmental Research Paper 285* (1968).
89. N. Hoang, R. DeYoung, C. Prasad and G. Laufer, "Differential absorption lidar (DIAL) measurements of atmospheric water vapor utilizing robotic aircraft," 19th International Laser Radar Conference, *NASA Conference Publication 207671*, 732-728 (1998).
90. J. Smucz, V. Fromzel, C. Prasad and R. DeYoung, "Atmospheric water vapor DIAL measurements using a diode-pumped, injection-seeded, high energy Cr:LiSAF laser transmitter," 20th *International Laser Radar Conference*, to be published.
91. V. Fromzel, J. Smucz, I. Hwang and C. Prasad, "A diode-pumped, injection-seeded, high energy Cr:LiSAF laser for water vapor DIAL," 20th *International Laser Radar Conference*, to be published.
92. V. Fromzel, C. Prasad, C. Johnson, N. Barnes, G. Kim and R. Mead, "A high energy diode-pumped Cr:LiSAF laser for water vapor differential absorption lidar," *Conference on Lasers and Electro-Optics, 1999 Technical Digest*, Baltimore, 481 (1999).
93. Atmospheric Soundings for the United States;
<http://www-das.uwyo.edu/upperair/sounding.html>, 1999

APPENDIX A

APD MANUFACTURER DATA AND CHARACTERIZATION RESULTS

A.1. APD designator and manufacturer data

APD	Manufacturer				Structure ¹
Model Number	d ²	\mathfrak{R} ³	V_B ⁴	I_n / V_n ⁵	BW ⁶
Serial Number	T ⁷	λ ⁸	V_{BD} ⁹	I_d ¹⁰	NEP ¹¹
APD12	EG&G				SLIK
C30649E	0.5	50 MV/W	349	150 nV/Hz ^{1/2}	11
147	25	820	356	7	0.003
APD11	EG&G				SLIK
C30649E	0.5	50 MV/W	431	150 nV/Hz ^{1/2}	12
148	25	820	440	8	0.003
APD10	Electron Tubes, Inc.				RTS
SSO-AD-2500	2.52	45 A/W	110		2.2×10^{-3}
#8-12	21.5	880	161.7	30	0.4
APD9	Electron Tubes, Inc.				RTS
SSO-ADH-500	0.5	45 A/W	150		1.3×10^{-3}
#10	21.5	880		1.5	0.2
APD8	EG&G				RTS
C30646E	0.5	20 MV/W	217	78 nV/Hz ^{1/2}	9.4 M
CD2507	22	850	228		0.004
APD7	EG&G				RTS
C30646E	1.5	6 MV/W	384	120 nV/Hz ^{1/2}	9.5 M
CD2508	22	1064	443		0.02

¹ "SLIK" for super low κ structure, "RTS" for reach through structure and "BE" for beveled edge structure.

² Diameter of the sensitive area in mm.

³ APD responsivity.

⁴ Bias Voltage in V.

⁵ Spectral noise current and voltage density in nA/Hz^{1/2} and nV/Hz^{1/2} respectively.

⁶ Bandwidth in MHz.

⁷ Testing temperature in °C.

⁸ Testing wavelength in nm.

⁹ Breakdown voltage in V.

¹⁰ Dark current in nA.

¹¹ Noise equivalent power in pW/Hz^{1/2}.

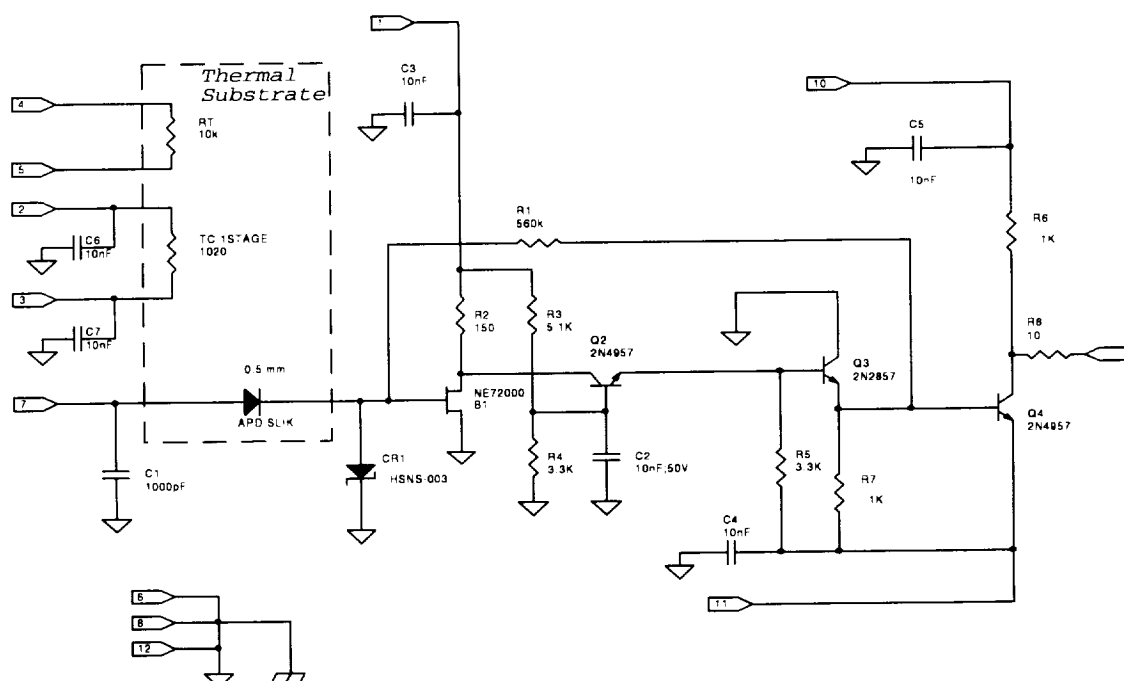
APD6	EG&G				RTS
C30659E	0.15	50 MV/W	420.4	110 nV/Hz ^{1/2}	15
CD2472		830	427	36	0.002

APD5	Advanced Photonix, Inc.				BE
197-70-71-520	5	108 A/W		2 pA/Hz ^{1/2}	43
	22	840	2450	160	0.014

APD4	EG&G				RTS
C30950E	0.8	0.5 MV/W	275	15 nV/Hz ^{1/2}	50
	25	830	425		0.029

APD2	EG&G				RTS
C30955E	1.5	70 A/W	275	2 pA/Hz ^{1/2}	---
1647		900	390	200	---

A.2. SLIK APD package



Detector Sensitive Area
 Trans-Impedance Amplifier Feedback Resistance
 Detector Maximum Power Loss
 TEC Maximum Current
 TEC Rated Current @ 0 °C
 TEC Area
 Thermistor Resistance

0.24 mm² (measured)

560 kΩ

50 Mw

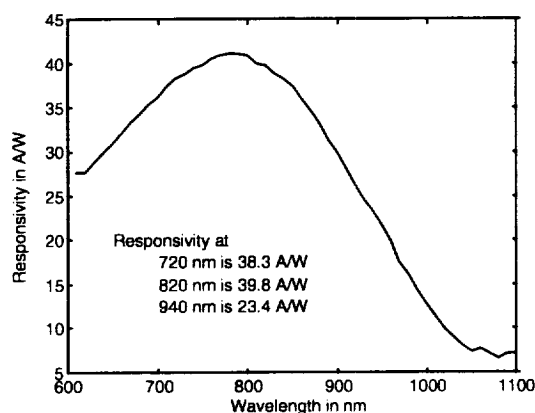
1.8 A

0.5 A

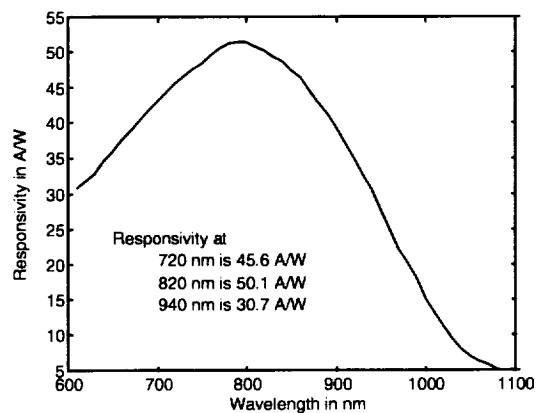
3.96x3.96 mm²

$$R_T = 10^4 \cdot e^{\left[3940 \left(\frac{1}{T} - \frac{1}{298} \right) \right]}$$

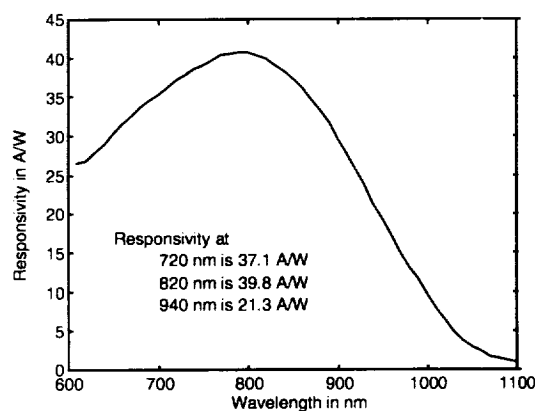
A.3. APD calibration results



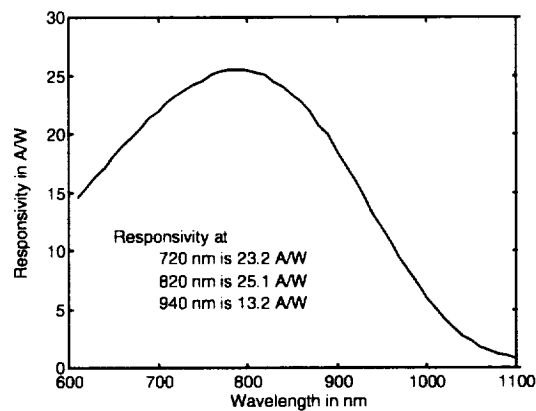
(a) APD12 Spectral Response at 336V and 25 °C.



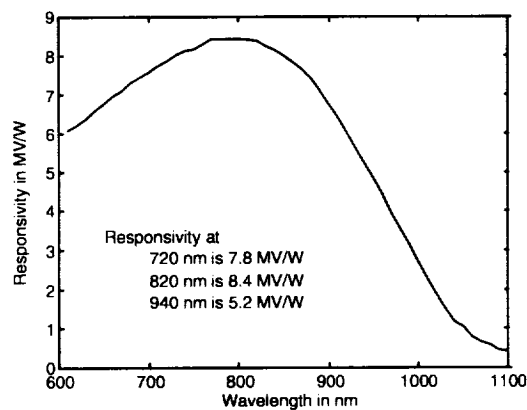
(b) APD11 Spectral Response at 415 V and 23 °C.



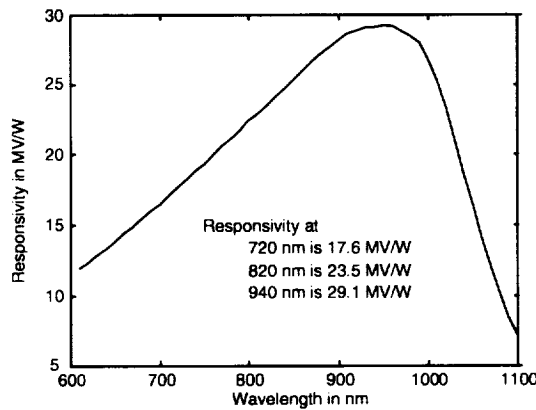
(c) APD10 Spectral Response at 110V and 22.3 °C.



(d) APD9 Spectral Response at 150V and 21.9 °C.

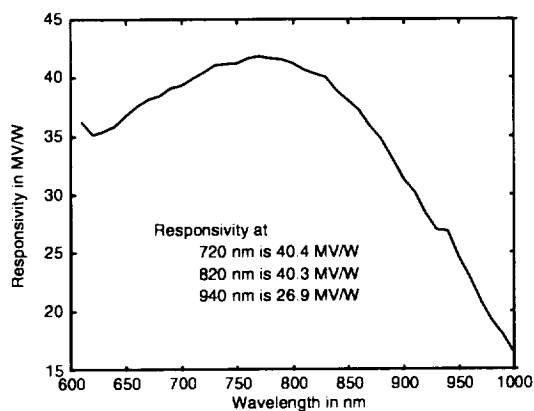


(e) APD8 Spectral Response at 190V and 23 °C.

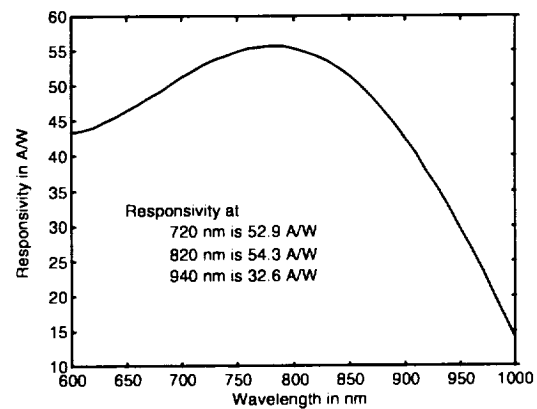


(f) APD7 Spectral Response at 380V and 23.6 °C.

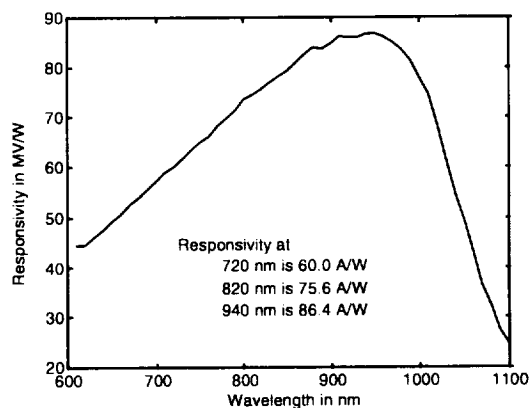
Fig.8 APD spectral response calibration.



(g) APD6 Spectral Response at 410V and 22.2 °C.



(h) APD5 Spectral Response at 2350V.



(i) APD2 Spectral Response at 317V and 23.1 °C.

Fig.8 (continue) APDs spectral response calibration.

A.4. APD surface scan results

APD	Active Area mm ²	Area non-uniformity
APD11	0.2376	14.96 %
APD10	4.9550	18.76 %
APD9	0.1800	11.27 %
APD8	0.1820	16.62 %
APD7	1.5970	15.50 %
APD6	0.0148	17.64 %
APD5	18.88	7.40 %
APD4	0.5464	6.02 %
APD2	1.6920	6.10 %

A.5. APD responsivity variation with temperature

APD12		Bias Voltage : 336 V	Condition : $-3 < T < 25$ °C
720 nm		$116.3 - 8.69T + 0.43T^2 - 8.3 \times 10^{-3}T^3$	A/W
820 nm		$113.8 - 8.23T + 0.41T^2 - 7.9 \times 10^{-3}T^3$	A/W
940 nm		$57.2 - 3.65T + 0.18T^2 - 3.6 \times 10^{-3}T^3$	A/W
APD11		Bias Voltage : 415 V	Condition : $-3 < T < 25$ °C
720 nm		$130.02 - 9.63T + 0.45T^2 - 8.3 \times 10^{-3}T^3$	A/W
820 nm		$136.19 - 9.85T + 0.46T^2 - 8.6 \times 10^{-3}T^3$	A/W
940 nm		$73.14 - 4.99T + 0.24T^2 - 4.4 \times 10^{-3}T^3$	A/W
APD10		Bias Voltage : 110 V	Condition : $6.3 < T < 22.3$ °C
720 nm		$3.85 \times 10^3 - 9.65 \times 10^2 T + 90.53T^2 - 3.71T^3 + 0.0557T^4$	A/W
820 nm		$4.22 \times 10^3 - 10.62 \times 10^2 T + 99.88T^2 - 4.09T^3 + 0.0617T^4$	A/W
940 nm		$2.17 \times 10^3 - 5.47 \times 10^2 T + 51.55T^2 - 2.12T^3 + 0.0319T^4$	A/W
APD9		Bias Voltage : 150 V	Condition : $10.4 < T < 21.9$ °C
720 nm		$58.9 - 2.92T + 8.82 \times 10^{-2}T^2 - 1.33 \times 10^{-3}T^3$	A/W
820 nm		$66.8 - 3.53T + 9.96 \times 10^{-2}T^2 - 1.15 \times 10^{-3}T^3$	A/W
940 nm		$35.2 - 1.96T + 5.75 \times 10^{-2}T^2 - 6.35 \times 10^{-4}T^3$	A/W
APD8		Bias Voltage : 190 V	Condition : $5 < T < 23$ °C
720 nm		$1.5 \times 10^7 - 4.9 \times 10^5 T + 7.6 \times 10^3 T^2$	V/W
820 nm		$1.6 \times 10^7 - 4.9 \times 10^5 T + 7.58 \times 10^3 T^2$	V/W
940 nm		$8.95 \times 10^7 - 2.6 \times 10^5 T + 4.2 \times 10^3 T^2$	V/W
APD7		Bias Voltage : 380 V	Condition : $13.3 < T < 24.5$ °C
720 nm		$2.24 \times 10^{10} - 3.26 \times 10^9 T + 1.63 \times 10^8 T^2 - 2.77 \times 10^6 T^3$	V/W
820 nm		$3.06 \times 10^{10} - 4.46 \times 10^9 T + 2.24 \times 10^8 T^2 - 3.79 \times 10^6 T^3$	V/W
940 nm		$3.88 \times 10^{10} - 5.67 \times 10^9 T + 2.86 \times 10^8 T^2 - 4.85 \times 10^6 T^3$	V/W
APD6		Bias Voltage : 410 V	Condition : $1.1 < T < 21.9$ °C
720 nm		$2.91 \times 10^8 - 4.63 \times 10^7 T + 3.07 \times 10^6 T^2 - 6.8 \times 10^4 T^3$	V/W
820 nm		$2.81 \times 10^8 - 4.53 \times 10^7 T + 3.04 \times 10^6 T^2 - 6.79 \times 10^4 T^3$	V/W
940 nm		$1.78 \times 10^8 - 2.89 \times 10^7 T + 1.96 \times 10^6 T^2 - 4.4 \times 10^4 T^3$	V/W
APD2		Bias Voltage : 317 V	Condition : $5.7 < T < 23.1$ °C
720 nm		$928.5 - 189.9T + 17.1T^2 - 0.6985T^3 + 0.011T^4$	A/W
820 nm		$1043.2 - 192.3T + 15.8T^2 - 0.6005T^3 + 0.0086T^4$	A/W
940 nm		$1093.9 - 185.9T + 14.1T^2 - 0.4956T^3 + 0.0066T^4$	A/W

A.6. APD responsivity variation with bias voltage

APD12		Temperature : 25 °C	Condition : 320 < V < 351 V
720 nm		$1.88 \times 10^7 - 2.25 \times 10^5 V + 1 \times 10^3 V^2 - 2.02 V^3 + 2 \times 10^{-3} V^4$	A/W
820 nm		$1.89 \times 10^7 - 2.27 \times 10^5 V + 1 \times 10^3 V^2 - 2.04 V^3 + 1.5 \times 10^{-3} V^4$	A/W
940 nm		$1.01 \times 10^7 - 1.22 \times 10^5 V + 5.47 \times 10^2 V^2 - 1.09 V^3 + 8.2 \times 10^{-4} V^4$	A/W
APD11		Temperature : 23 °C	Condition : 390 < V < 430 V
720 nm		$-2.76 \times 10^5 + 2.06 \times 10^3 V - 5.12 V^2 + 4.25 \times 10^{-3} V^3$	A/W
820 nm		$-2.91 \times 10^5 + 2.17 \times 10^3 V - 5.41 V^2 + 4.49 \times 10^{-3} V^3$	A/W
940 nm		$-1.65 \times 10^5 + 1.23 \times 10^3 V - 3.07 V^2 + 2.54 \times 10^{-3} V^3$	A/W
APD10		Temperature : 20.9 °C	Condition : 80 < V < 115 V
720 nm		$-9.1 \times 10^3 + 296.7 V - 3.19 V^2 + 1.14 \times 10^{-2} V^3$	A/W
820 nm		$-9.5 \times 10^3 + 308.6 V - 3.32 V^2 + 1.19 \times 10^{-2} V^3$	A/W
940 nm		$-5.2 \times 10^3 + 167.7 V - 1.81 V^2 + 6.46 \times 10^{-3} V^3$	A/W
APD9		Temperature : 22 °C	Condition : 125 < V < 150 V
720 nm		$-3.2 \times 10^3 + 73.4 V - 0.55 V^2 + 1.4 \times 10^{-3} V^3$	A/W
820 nm		$-3.6 \times 10^3 + 80.5 V - 0.61 V^2 + 1.5 \times 10^{-3} V^3$	A/W
940 nm		$-1.9 \times 10^3 + 42.6 V - 0.32 V^2 + 8 \times 10^{-4} V^3$	A/W
APD8		Temperature : 19.9 °C	Condition : 100 < V < 215 V
720 nm		$-2.1 \times 10^9 + 3.98 \times 10^7 V - 2.5 \times 10^5 V^2 + 5 \times 10^2 V^3$	V/W
820 nm		$-2.25 \times 10^9 + 4.2 \times 10^7 V - 2.6 \times 10^5 V^2 + 5.35 \times 10^2 V^3$	V/W
940 nm		$-1.4 \times 10^9 + 2.69 \times 10^7 V - 1.66 \times 10^5 V^2 + 3.4 \times 10^2 V^3$	V/W
APD7		Temperature : 22.1 °C	Condition : 100 < V < 380 V
720 nm		$3.81 \times 10^7 - 9.19 \times 10^6 V + 7.83 \times 10^3 V^2 - 27.1 V^3 + 3.33 \times 10^{-2} V^4$	V/W
820 nm		$5.07 \times 10^7 - 1.22 \times 10^6 V + 1.04 \times 10^4 V^2 - 36.1 V^3 + 4.45 \times 10^{-2} V^4$	V/W
940 nm		$6.28 \times 10^7 - 1.52 \times 10^6 V + 1.29 \times 10^4 V^2 - 44.7 V^3 + 5.52 \times 10^{-2} V^4$	V/W
APD6		Temperature : 22.6 °C	Condition : 100 < V < 350 V
720 nm		$4.02 \times 10^8 - 8.77 \times 10^6 V + 6.80 \times 10^4 V^2 - 222.5 V^3 + 0.263 V^4$	V/W
820 nm		$4.61 \times 10^8 - 10.02 \times 10^6 V + 7.75 \times 10^4 V^2 - 253.2 V^3 + 0.299 V^4$	V/W
940 nm		$2.96 \times 10^8 - 6.35 \times 10^6 V + 4.89 \times 10^4 V^2 - 159.4 V^3 + 0.188 V^4$	V/W
APD5		Temperature : 20 °C	Condition : 2050 < V < 2350 V
720 nm		$-1.73 \times 10^4 + 24.54 V - 0.012 V^2 + 0.184 \times 10^{-5} V^3$	A/W
820 nm		$-1.75 \times 10^4 + 24.79 V - 0.012 V^2 + 0.186 \times 10^{-5} V^3$	A/W
940 nm		$-0.94 \times 10^4 + 13.25 V - 0.006 V^2 + 0.099 \times 10^{-5} V^3$	A/W
APD2		Temperature : 23.1 °C	Condition : 310 < V < 340 V
720 nm		$-1.71 \times 10^4 + 1.68 \times 10^2 V - 0.551 V^2 + 6.05 \times 10^{-4} V^3$	A/W
820 nm		$-3.28 \times 10^4 + 3.16 \times 10^2 V - 1.018 V^2 + 1.095 \times 10^{-3} V^3$	A/W
940 nm		$-4.44 \times 10^4 + 4.25 \times 10^2 V - 1.36 V^2 + 1.45 \times 10^{-3} V^3$	A/W

A.7. APD noise measurement

APD	λ nm	I_n	NEP fW/Hz ^{1/2}	D^* cmHz ^{1/2} /W
APD12	720	2.2×10^{-13} A/Hz ^{1/2}	1.9	2.87×10^{13}
	820		1.9	3.05×10^{13}
	940		3.9	1.63×10^{13}
APD11	720	2.3×10^{-13} A/Hz ^{1/2}	1.8	2.77×10^{13}
	820		1.7	2.90×10^{13}
	940		3.1	1.57×10^{13}
APD10	720	2.5×10^{-12} A/Hz ^{1/2}	74.3	2.99×10^{12}
	820		69.3	3.21×10^{12}
	940		129.4	1.72×10^{12}
APD9	720	1.9×10^{-12} A/Hz ^{1/2}	80.7	5.26×10^{11}
	820		74.9	5.67×10^{11}
	940		141.8	2.99×10^{11}
APD8	720	9.3×10^{-8} V/Hz ^{1/2}	11.8	3.62×10^{12}
	820		11.0	3.88×10^{12}
	940		17.7	2.41×10^{12}
APD2	720	1.7×10^{-12} A/Hz ^{1/2}	28.0	4.75×10^{12}
	820		22.2	5.99×10^{12}
	940		19.4	6.84×10^{12}

APPENDIX B

DETECTION SYSTEM APPLIED CIRCUITS

B.1. Analog-to-digital converter circuit

The AD9240 is a 10-M sample per second, 14-bit ADC. It has an on-chip low noise sample and hold amplifier and a programmable voltage reference. Figure B1 shows the associated programming circuit in our application. C32, C33, C34, C35 and Ca35 are 0.1- μ F bypass capacitors between each supply and its corresponding ground pin. The AD9240 maximum conversion rate can be controlled by R34. VINA and VINB are two analog inputs for either a differential input mode or single-ended mode. By connecting VINB to VREF and SENSE via R33, the second mode is selected with a common mode at 1 V with 2 V input range. The chip internal reference, which appears on CAPT and CAPB, is used in this connection. C28, C29, C30 and C31 form the recommended decoupling network to insure a stable reference. It should be noted that this device provides the only connection between the analog and the digital grounds.

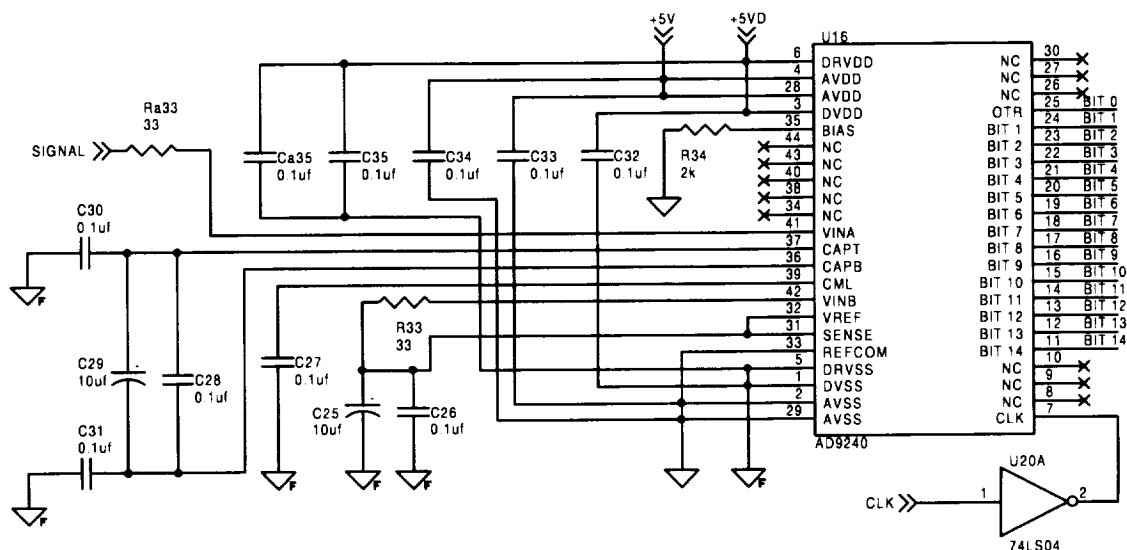


Figure B1 Analog to digital converter circuit.

B.2. Data collect and store circuit

The data collect and store circuit acts as a single shot transient recorder. The operation of this circuit is fully controlled by the microcontroller through the "counter enable" signal, applied by the two input NAND gate U15A. A microcontroller "clear counter" signal clears the contents of all three, four bit binary counters and the J-K flip flop. The maximum count is detected by four input NAND gate, U14A, which

automatically stops the counting operation through U15A and sends an “end-of-count” signal to the microcontroller.

To reduce pick-up noise, the inverter U20A enables the data conversion by the ADC in a different half cycle than that of the counter. Connecting the MSB of the RAM left address to supply enable the data to be stored only in the lower half of the memory.

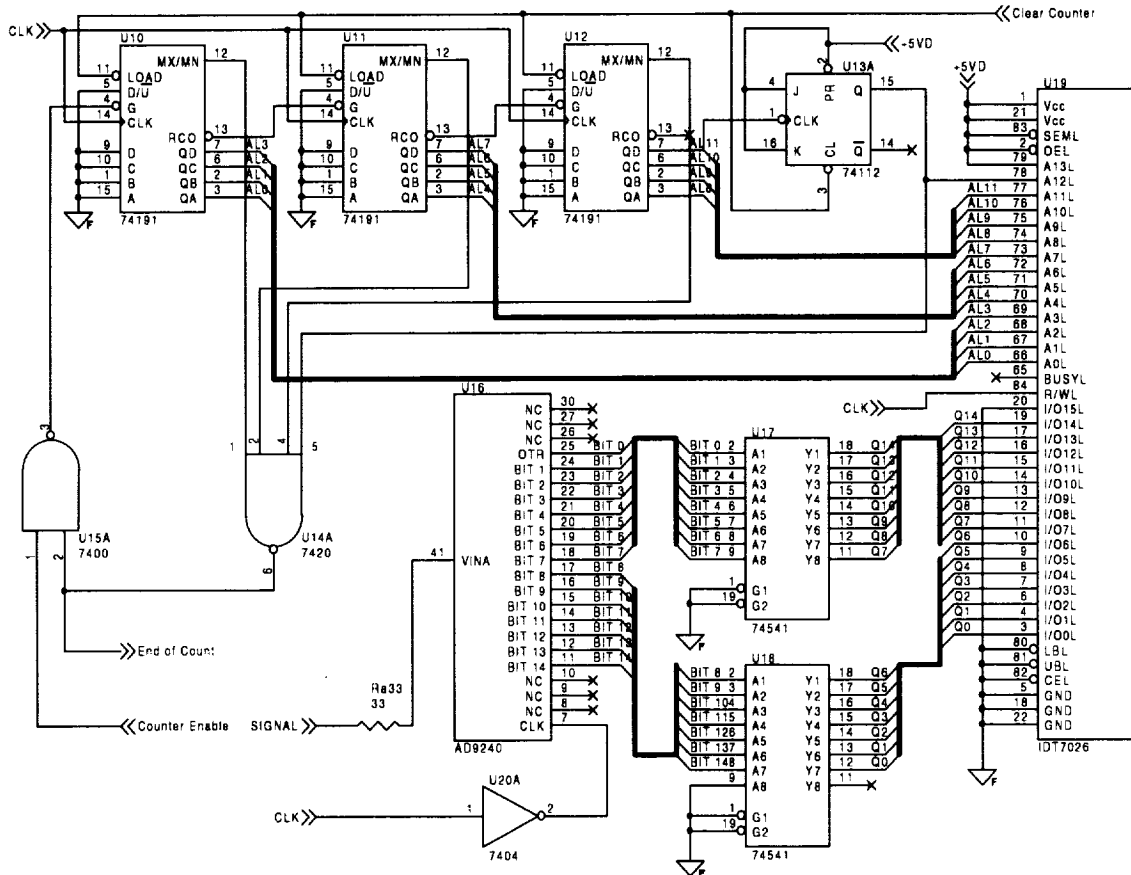


Figure B2 Data collect and store circuit.

B.3. Microcontroller connection circuit

The 80C196KB-16 microcontroller shares the data and address on one 16 bit bus. The address latch, formed by U24 and U25, is used to distinguish and separate the address and the data words. The inverter U20B is used to divide the microcontroller memory into two sections. One section accesses the right address of the dual port RAM, while the other section is sub-divided into two sub-sections. The two sub-sections are decoded to access the FIFO using the four input AND gate U26A, while the other is used to access the 8-bit dip-switch using the four input AND gate U26B and the inverters U20C and U20D. The control of the FIFO and counter operations is obtained using the microcontroller port 1. Port 2 is used to sense the “trigger” signal and for serial communication if applied. Port 0 is set as analog channels to the internal analog to digital

converter in order to read the APD temperature and bias voltage values. Each monitor channel is protected using the interface circuit shown in figure B4a. Figure B4b shows the microcontroller reset circuit.

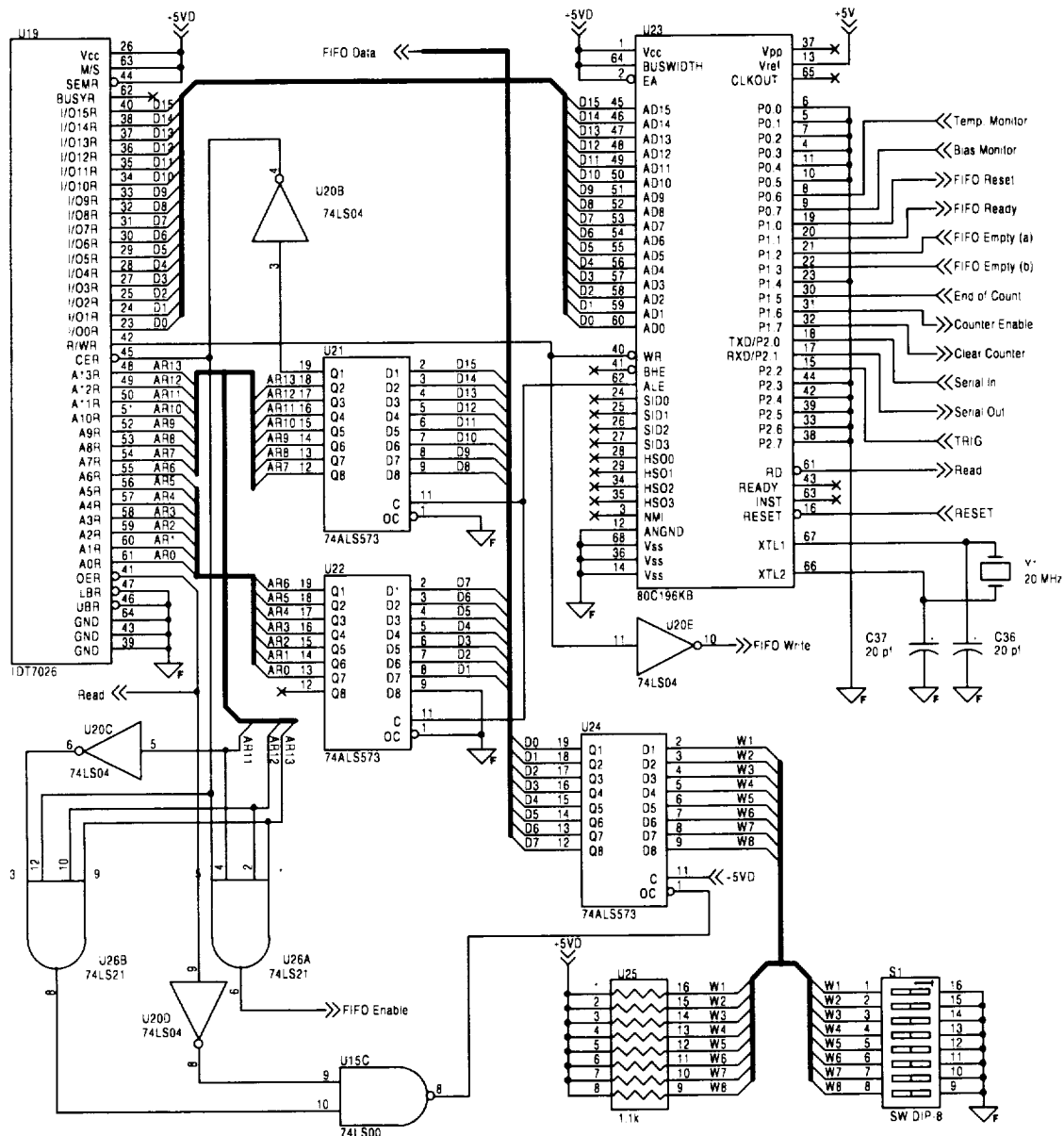


Figure B3 Microcontroller connection circuit.

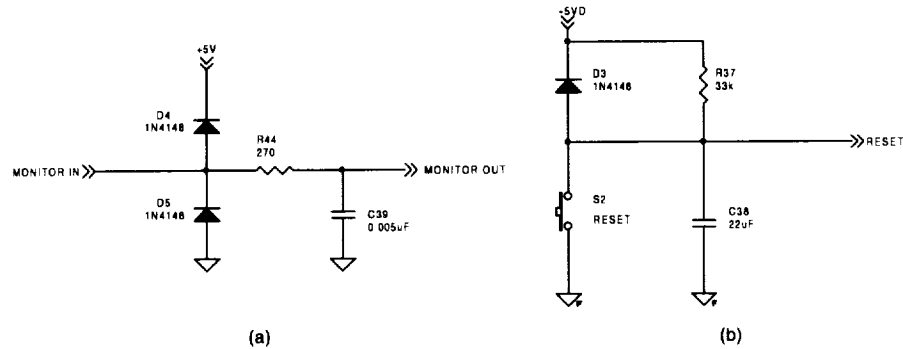


Figure B4 Microcontroller (a) ADC interface and (b) reset circuit.

B.4. Output stage

The FIFO output data is buffered using U29 and U30, the output of which is applied to the four channel opto-couplers U31-U34 for ground optical isolation. The FIFO control signals “FIFO ready” and “read FIFO” are also optically isolated using the dual separate channels U37 optocouplers.

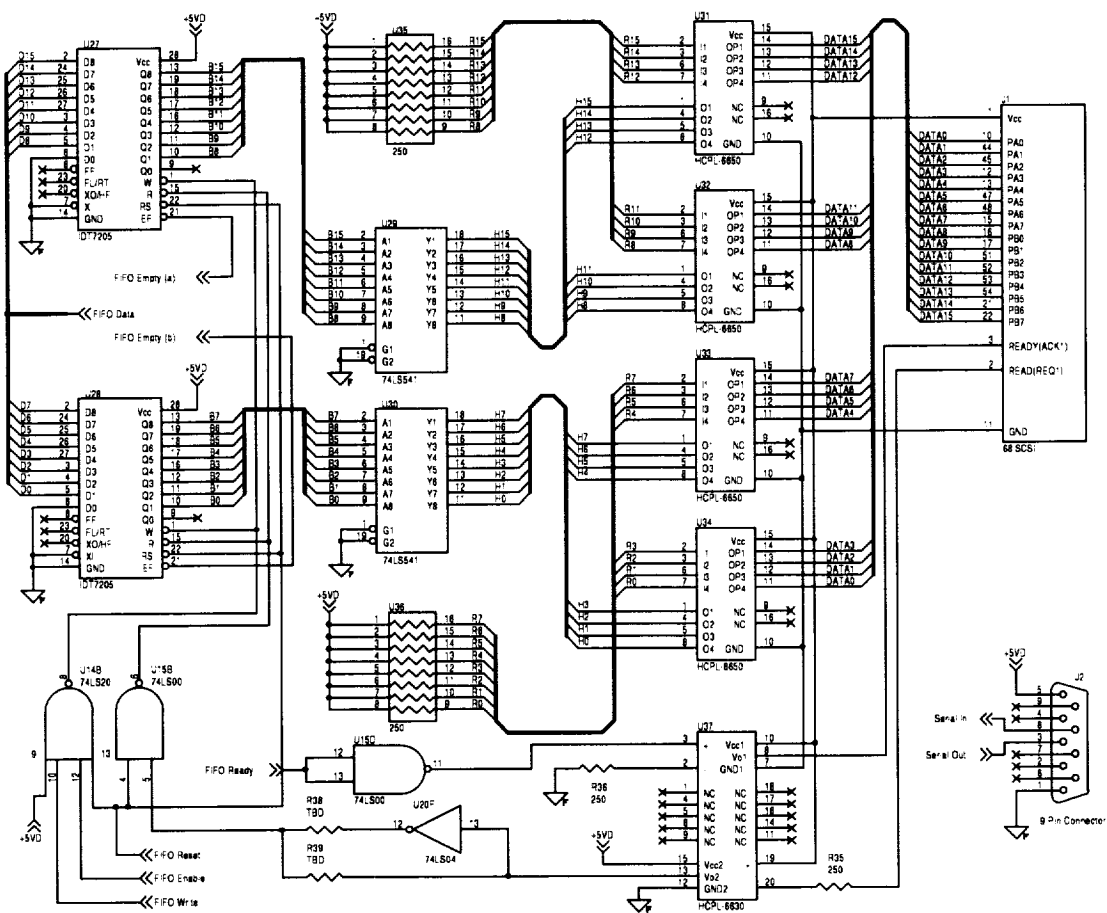


Figure B5 Microcontroller connection circuit.

B.5. Chip power supply bypassing

Generally, bypass or coupling capacitors are used with every supply pin of any device. It is used to supply the device with inrush current required at switching instants. Figure B6 shows the used power supply bypassing for an op amp, for both the positive and the negative supplies. Inductors Lx1 and Lx2 are used for smoothing the device bias current. As a layout restriction, ceramic capacitors (Cx3 and Cx1 are 0.1 μ F) must be located less than 0.3 cm away from the supply pin. Cx2 and Cx4 are 10 μ F electrolyte capacitors. For all devices other than op amps, 0.1 μ F capacitors are only in use to couple every supply pin to the ground.

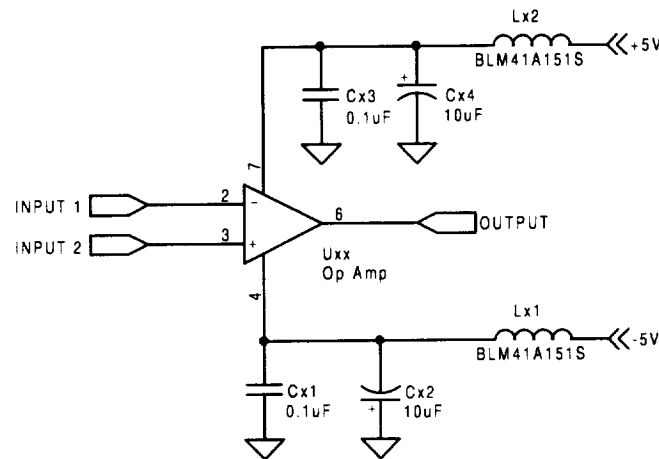


Figure B6 Op amp connection to power supplies.

B.6. Clock and trigger isolation

U38, the HCPL-2430, is a dual channel, TTL compatible optocoupler. It is used to optically isolate the clock and the trigger inputs as shown in Fig.D5. Resistors R41 and R42 are 50 Ω termination resistors. R40 and R43 are used to limit light emitting diode current.

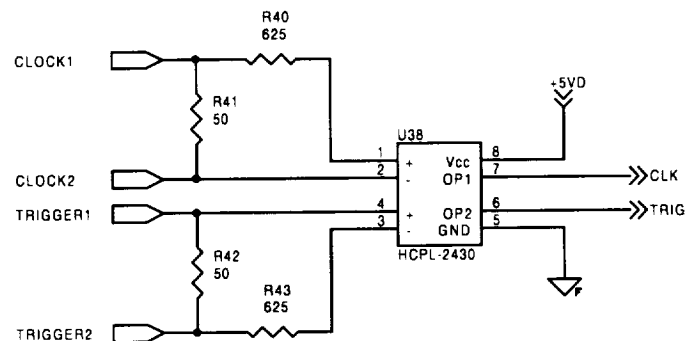


Figure B7 External clock and trigger isolation circuit.

APPENDIX C

ELEMENTS OF THE NEW DETECTION SYSTEM

C.1. Detection system components

Referring to Chapter 4 and Appendix B, this appendix gives the component list of the new detection system along with the description of these component, the manufacturer and the number of parts used.

Component	Part Reference	Description	Manufacturer	# of Parts
AD586BR	U1	Reference Voltage	Analog Devices	1
AD706AR	U2,U3,U5	Dual Op-Amp	Analog Devices	3
521-5-M	U4	High Voltage Supply	Analog Modules	1
C30649E	U6	Avalanche Photodiode	EG&G	1
AD8036AR	U7	Clipping Amplifier	Analog Devices	1
AD8041AR	U8	Buffer Amplifier	Analog Devices	1
B3LL31-25-P/P	U9	Output Filter	Microwave Inc.	1
74F191SC	U10,U11,U12	4 Bit Counter	FAIRCHILD	3
TC74AC112FN	U13	Dual JK Flip Flop	TOSHIBA	1
TC74VHC20FT	U14	Dual, 4 input NAND	TOSHIBA	1
TC74VHC21FT	U26	Dual, 4 Input AND	TOSHIBA	1
TC74VHCT00AFT	U15	Quad,2 Input NAND	TOSHIBA	1
AD9240AS	U16	14 Bit, 10 MHz ADC	Analog Devices	1
TC74VHCT541AF T	U17,U18,U29,U30	Octal Buffers	TOSHIBA	4
IDT7026L20J	U19	Dual Port RAM	IDT	1
TC74VHC04FT	U20	Hex Inverters	TOSHIBA	1
TC74VHC573FT	U21,U22,U24	8 Bit, Address Latch	TOSHIBA	3
N87C196KB-16	U23	Microcontroller	INTEL	1
IDT7205L15J	U27,U28	8k, 9Bit, FIFO	IDT	2
HCPL-6650	U31,U32,U33,U34	4 Channel Optocoupler	Hewlett Packard	4
HCPL-6630	U37	2 Channel Optocoupler	Hewlett Packard	1
HCPL-2430#300	U38	2 Channel Optocoupler	Hewlett Packard	1
766-163-R(1k)	U25	1k, 2%,160mW, Resistor Network	CTS	1
766-163-R(270)	U35,U36	270, 2%,160mW, Resistor Network	CTS	2
LL4148DICT	D1,D3,D4,D5,D6, D7	Diode, 1N4148	VISHAY	6
BZX84C5V1DICT	D2	5.1V, Zener Diode	VISHAY	1
TIP110	Q1	Darlington Transistor	Texas Instrument	1
NFM46P11C155	L1,L2,L4,L5,L16	Line Filter	MURATA	5
BLM41A151S	L3,L6,L7,L8,L9, L10,L11,L12,L13, L14,L15	Chip Ferrite Bead Inductors	MURATA	11

Component	Part Reference	Description	Manufacturer	# of Parts
1812Y104JXE	C8	0.1 μ F, 500 V, 5% Ceramic Capacitor	VISHAY	1
VJ1812Y105JXXM	C2,C10,C5,C5a	1 μ F, 25V, 5% Ceramic Capacitor	VISHAY	4
PCC472BCT	C39,C40	5nF, 50V, 10%, Ceramic Capacitor	Panasonic	2
PCS1226CT	C38	22 μ F, 6.3V Tantalum Capacitor	Panasonic	1
PCC200CCT	C36,C37	20pF, 50V, 5% Ceramic Capacitor	Panasonic	2
PCC220JCT	C9	22pF, 3kV, 5% Ceramic Capacitor	Panasonic	1
PCS3106CT	C14,C17,C21,C23, C25, C29,C3u23	10 μ F, 16V Tantalum Capacitor	Panasonic	6
PCC103BCT	Cu31,Cu32,Cu33, CU34,C1u37,C2u37 C1u19,C2u19, C3u19,C1u23	0.01 μ F, 50V, 10% Coupling Capacitor	Panasonic	6
PCC104BCT	C1,C3,C4,C6,C7, C11,C12,C13,C15, C16,C18,C19,C20, C22,C24,C26,C27, C28,C30,C31,C32, C33,C34,C35,Cu10, Ca35,Cu11,Cu12, Cu13,Cu14,Cu15, Cu17,Cu18,Cu20, Cu21,Cu22,Cu24, Cu26,Cu27,Cu28,	0.1 μ F, 50V, 10% Coupling Capacitor	Panasonic	42
895-0205	R32	5 Ω , 1% Resistor	Dale	2
P33ECT	R33,Ra33	33 Ω , 5% Resistor	Panasonic	2
P50FCT	R21,R30,R31,R41, R42	49.9 Ω , 1% Resistor	Panasonic	5
TNPW1206100B	R26	100 Ω , 1% Resistor	VISHAY	2
P130FCT	R22	130 Ω , 1% Resistor	Panasonic	1
P140FCT	R23	140 Ω , 1% Resistor	Panasonic	1
P270ECT	R35,R36,R44,R45	270 Ω , 5% Resistor	Panasonic	4
TNPW1206301B	R27,R28,R29	301 Ω , 1% Resistor	VISHAY	3
P499FCT	R6	499 Ω , 1% Resistor	Panasonic	1
P620ECT	R40,R43	620 Ω , 5% Resistor	Panasonic	2
P2KZCT	R14,R34	2 k Ω , 0.1% Resistor	Panasonic	2
P3KZCT	R2	3 k Ω , 0.1% Resistor	Panasonic	1
P10KZCT	R1,R8,R24,R25	10 k Ω , 0.1% Resistor	Panasonic	4
P22KZCT	R13	22 k Ω , 0.1% Resistor	Panasonic	1
P33KZCT	R17,R15,R16,R37	33 k Ω , 0.1% Resistor	Panasonic	4
P49.9KFCT	R3	49.9 k Ω , 1% Resistor	Panasonic	1
P82KZCT	R12	82 k Ω , 0.1% Resistor	Panasonic	1

Component	Part Reference	Description	Manufacturer	# of Parts
P200KFCT	R4,R5,R19	200 k Ω , 1% Resistor	Panasonic	3
	R9,R10,R11	2.55 M Ω Resistor		3
	R18,R38,R39	TBD		
SM4W103	R7,R20	10 k Ω , POT, 10%	Philips	2
SPE1211	JP1,JP2,JP3,JP4	Jumpers	Specialty Elec.Inc.	2
777600-01	J1	68 Pin Connector	AMP	1
AFR09G	J2	9 Pin D Connector	AMP	1
AMR09G	J3	9 Pin D Connector	AMP	1
CT2198MST	S1	8 Pin, Dip Switches	CTS	1
P8087SCT	S2	Push Button Switch	Panasonic	1
XC550CT	Y1	16 MHz Crystal	ECS	1
SK-PLCC68-SO1		68pin, PLCC Socket	Ironwood Elec.	1

C.2. Detection system power consumption

The steady state maximum power consumption of the individual components of the detection system and the total power for each section are given as follows:

Reference Voltage			
	P U1	500.00 mW	
	P U2	650.00 mW	
	P R1	2.50 mW	
	P R2	0.75 mW	
Total power	P1	1153.25 mW	(1)
Signal Conditioning			
	P U6	250.00 mW	
	P U7	900.00 mW	
	P U8	900.00 mW	
	P R21	45.00 mW	
	P R24	0.70 mW	
	P R25	0.70 mW	
	P R26	22.50 mW	
	P R27	67.50 mW	
	P R28	67.50 mW	
	P R29	67.50 mW	
	P R30	101.30 mW	
	P R31	101.30 mW	
Total power	P2	2524.00 mW	(2)

Voltage Controller			
	P U3	650.00	mW
	P U4	480.00	mW
	P R3	0.50	mW
	P R4	2.00	mW
	P R5	2.00	mW
	P R6	50.00	mW
	P R7	2.50	mW
	P R8	0.10	mW
	P R9-11	20.70	mW
	P R12	0.20	mW
	P R13	0.10	mW
Total power	P3	1208.10	mW (3)
Temperature Controller			
	P U5	650.00	mW
	P R14	24.50	mW
	P D2	16.70	mW
	P R15	0.40	mW
	P R16	0.40	mW
	P R17	0.40	mW
	P R19	0.20	mW
	P R20	14.40	mW
	P RT	0.40	mW
Total power	P4	707.40	mW (4)
	P R32	625.00	mW
	P Q1	1875.00	mW
	P TEC	125.00	mW
Total power	P5	2625.00	mW (5)
Data Collect and Store			
	P U10	100.00	mW
	P U11	100.00	mW
	P U12	100.00	mW
	P U13	180.00	mW
	P U14	180.00	mW
	P U15	180.00	mW
	P U16	285.00	mW
	P U17	180.00	mW
	P U18	180.00	mW
Total power	P6	1485.00	mW (6)

Microcontroller Circuit			
	P U19	750.00 mW	
	P U20	180.00 mW	
	P U21	180.00 mW	
	P U22	180.00 mW	
	P U23	1500.00 mW	
	P U24	180.00 mW	
	P U25	181.80 mW	
	P U26	180.00 mW	
Total power	P7	3331.80 mW	(7)
Output Stage			
	P U27	770.00 mW	
	P U28	770.00 mW	
	P U29	180.00 mW	
	P U30	180.00 mW	
	P U31	800.00 mW	
	P U32	800.00 mW	
	P U33	800.00 mW	
	P U34	800.00 mW	
	P U35	800.00 mW	
	P U36	800.00 mW	
	P U37	400.00 mW	
	P U38	700.00 mW	
	P R40	10.00 mW	
	P R41	125.00 mW	
	P R42	125.00 mW	
	P R43	10.00 mW	
Total power	P8	8070.00 mW	(8)

Total Power for Analog Circuit from ± 5 V Supply

$$=P_2+P_5= 2524.00+2625.00 =5149.00 \text{ mW}$$

Total Power for Analog Circuit from ± 12 V Supply

$$=P_1+P_3+P_4= 1153.25+1208.10+707.40 =3068.75 \text{ mW}$$

Total Power for Analog Circuit

$$=P_1+P_2+P_3+P_4+P_5= 5149.00+3068.75 =8217.75 \text{ mW}$$

Total Power for Digital Circuit from +5 V Supply

$$=P_6+P_7+P_8= 1485.00+3331.80+8070.00 =12886.80 \text{ mW}$$

Total Power for the Card

$$=P_1+P_2+P_3+P_4+P_5+P_6+P_7+P_8= 8217.75+12886.80 =21104.55 \text{ mW}$$

REPORT DOCUMENTATION PAGE			Form Approved OMB No. 0704-0188	
Public reporting burden for this collection of information is estimated to average 1 hour per response, including the time for reviewing instructions, searching existing data sources, gathering and maintaining the data needed, and completing and reviewing the collection of information. Send comments regarding this burden estimate or any other aspect of this collection of information, including suggestions for reducing this burden, to Washington Headquarters Services, Directorate for Information Operations and Reports, 1215 Jefferson Davis Highway, Suite 1204, Arlington, VA 22202-4302, and to the Office of Management and Budget, Paperwork Reduction Project (0704-0188), Washington, DC 20503.				
1. AGENCY USE ONLY (Leave blank)		2. REPORT DATE June 2000		3. REPORT TYPE AND DATES COVERED Contractor Report
4. TITLE AND SUBTITLE Advanced Atmospheric Water Vapor DIAL Detection System			5. FUNDING NUMBERS PO L-68314D WU 622-63-13-70	
6. AUTHOR(S) Tamer F. Refaat and Hani E. Elsayed-Ali				
7. PERFORMING ORGANIZATION NAME(S) AND ADDRESS(ES) Old Dominion University Norfolk, VA 23508			8. PERFORMING ORGANIZATION REPORT NUMBER	
9. SPONSORING/MONITORING AGENCY NAME(S) AND ADDRESS(ES) National Aeronautics and Space Administration Langley Research Center Hampton, VA 23681-2199			10. SPONSORING/MONITORING AGENCY REPORT NUMBER NASA/CR-2000-210301	
11. SUPPLEMENTARY NOTES Langley Technical Monitor: Russell J. DeYoung				
12a. DISTRIBUTION/AVAILABILITY STATEMENT Unclassified-Unlimited Subject Category 33 Distribution: Nonstandard Availability: NASA CASI (301) 621-0390			12b. DISTRIBUTION CODE	
13. ABSTRACT (Maximum 200 words) Measurement of atmospheric water vapor is very important for understanding the Earth's climate and water cycle. The remote sensing Differential Absorption Lidar (DIAL) technique is a powerful method to perform such measurement from aircraft and space. This thesis describes a new advanced detection system, which incorporates major improvements regarding sensitivity and size. These improvements include a low noise advanced avalanche photodiode detector, a custom analog circuit, a 14-bit digitizer, a microcontroller for on board averaging and finally a fast computer interface. This thesis describes the design and validation of this new water vapor DIAL detection system which was integrated onto a small Printed Circuit Board (PCB) with minimal weight and power consumption. Comparing its measurements to an existing DIAL system for aerosol and water vapor profiling validated the detection system.				
14. SUBJECT TERMS APD modelling; APD characterization; Digitizers; Lidar, DIAL			15. NUMBER OF PAGES 155	
			16. PRICE CODE A08	
17. SECURITY CLASSIFICATION OF REPORT Unclassified	18. SECURITY CLASSIFICATION OF THIS PAGE Unclassified	19. SECURITY CLASSIFICATION OF ABSTRACT Unclassified	20. LIMITATION OF ABSTRACT UL	

